WATER CAVITATION PEENING FOR AEROSPACE MATERIALS

A Dissertation
Presented to
The Academic Faculty

by

Andrea Marcon

In Partial Fulfillment
of the Requirements for the Degree
Doctor of Philosophy in the
School of Mechanical Engineering

Georgia Institute of Technology
May 2017

COPYRIGHT © 2017 BY ANDREA MARCON

WATER CAVITATION PEENING FOR AEROSPACE MATERIALS

Approved by:

Dr. Shreyes Melkote, Advisor
School of Mechanical Engineering
Georgia Institute of Technology

Dr. Minami Yoda
School of Mechanical Engineering
Georgia Institute of Technology

Dr. Christopher Saldana
School of Mechanical Engineering
Georgia Institute of Technology

Dr. Richard Neu
School of Mechanical Engineering
Georgia Institute of Technology

Dr. James Castle
Boeing Research and Technology
The Boeing Company

Date Approved: January 20th, 2017

To my wife, Cassi

ACKNOWLEDGEMENTS

First and foremost, I would like to express gratitude to my advisor, Dr. Shreyes Melkote, for being patient with me and providing the guidance necessary to complete this journey over the past few years. This would not have been possible without his human qualities. Special thanks to Dr. Minami Yoda, for overlooking my work and for the many conversations that helped me improve my ideas. My gratitude also goes to Boeing Research and Technology for funding this project. In particular, I'd like to thank Dr. James Castle and Dr. Dan Sanders for believing in my work and supporting me over the years. My appreciation extends to my committee members, Dr. Richard Neu and Dr. Christopher Saldana, for helping me improve the quality of my work. Special thanks to Steven Sheffield and all the machine shop crew, past and present, who helped me tremendously in the beginning of this project and taught me a few things about this country. Thanks to my PMRC colleagues, in particular to those who shared an office with me and were subjected to my many opinions. Thanks to the many friends I met here in Atlanta, in particular to Tony and Debra, who really made the difference in my first few years.

My endless gratitude goes to my family. To my parents for always supporting me, even when my choices involved leaving home. To my brother and his family, for their constant effort to fill the distance between our two countries. To my new family, for welcoming me and making me feel at home. Finally, to my wife, who made this a place worth living in.

TABLE OF CONTENTS

LIST OF TABLES

LIST OF FIGURES

ix

x

xiii

SUMMARY

Conventional shot peening has been used for almost a century as a means to mechanically improve the fatigue and corrosion resistance of metals. It employs spherical shots of different size and materials to introduce compressive residual stress in the surface layers of metals, thereby improving their mechanical integrity when subjected to cyclic loading and/or a corrosive environment. However, this technique is also characterized by substantial surface roughening, high consumables cost and workpiece contamination.

Over the past few decades, a number of alternative peening techniques have been developed to overcome these limitations. Among them, water cavitation jet peening (WCP) has showed promising preliminary results in further extending fatigue life, reducing surface modification and lowering equipment and operating costs. Nevertheless, there is limited scientific understanding of this process at present. Consequently, there is a need for further studies aimed at developing detailed fundamental understanding of the cavitation jet peening process, exploring its potential and adequately characterizing the process to satisfy the demanding requirements set by industry, especially for aerospace applications.

This thesis presents an investigation of a novel *co-flow* water cavitation jet peening (WCP) system that expands the limited understanding of the process and addresses the limitations of the currently available peening processes. The basic concept involves creating cavitation by injecting a high speed jet into a low speed jet in a concentric (or co-flow) configuration, and placing the co-flow nozzle at an optimum distance from the workpiece surface. By suitably controlling the flow parameters and nozzle dimensions, it is possible to produce a sufficiently aggressive cavitation cloud capable of plastically

deforming metal surfaces and introducing beneficial compressive residual stresses. The main focus of this thesis is on the development of a WCP peening and the fundamental characterization of the cavitating flow for peening applications.

The flow characterization is carried out by means of accelerated erosion tests and strip curvature tests. Accelerated erosion tests are commonly used in the field of cavitation erosion to evaluate cavitation intensity and rank the erosion resistance of common engineering materials. Strip curvature tests are an established practice in the peening field used to evaluate the effectiveness of peening treatments. The results indicate that cavitation intensity and peening capability can be substantially increased by adopting suitable flow conditions, and that the optimum outer flow velocity V_{out} and normalized standoff distance s_N are essentially independent of the inner flow velocity V_{in} within the range adopted for this study. Peening tests carried out on Aluminum 7075-T651 give higher and deeper residual stresses compared to shot peening while lowering the surface roughening, potentially leading to a substantial increase in the fatigue life of components treated by WCP compared to conventional shot peening.

Nozzle geometry in co-flow configuration is investigated following the same approach developed in the previous study. Among other aspects, the scalability of the process is investigated by testing three nozzles with constant geometry ratios but increasing in size. Peening time is found to diminish by 30% as a consequence of a 12% increase of the nozzle diameter. Interestingly, optimum flow parameters previously identified are found to apply to different nozzles as well. In addition to erosion and strip curvature tests, high speed video imaging analysis is introduced to investigate the effect of nozzle geometry on the

cavitation cloud. A correlation is found between cavitation intensity, cavitation cloud width and its power spectral density.

Finally, pitting tests are carried out on mirror finished Aluminum 7075-T651 samples under several flow conditions and impact loads exerted by single cavitation phenomena onto the material surface are calculated. The pitting tests are found in good agreement with the flow characterization performed in chapter 4, showing larger pit diameters and impact loads for the flow conditions leading higher mass loss and strip curvature. The stress generated by the cavitation phenomena and the pit diameter observed during the pitting tests are used as input in a dynamic, 2D axisymmetric finite element model solved in ABAQUS/Explicit. The purpose of the model is to obtain an estimate of the longitudinal residual stresses introduced in the material surface by a single cavitation phenomenon using the information collected through the stress-strain analysis. Although the actual peening process is characterized by thousands of cavitation impacts per unit time and area, the pitting tests, along with the model of a single cavitation bubble collapse, reveal encouraging results for the future development of a semi-empirical model capable of predicting the residual stress state in WCP.

In summary, this thesis describes the investigation of an innovative water cavitation peening process capable of introducing compressive residual stresses in aerospace materials such as Aluminum 7075-T651 while limiting surface roughness and contamination typical of conventional shot peening. The characterization of the process and nozzle serve as a basis for users to select optimal peening conditions and create a cost effective alternative to the conventional shot peening technology.

CHAPTER 1.   INTRODUCTION

Conventional shot peening has been used for almost a century as a means to mechanically improve the fatigue and corrosion resistance of metals. It employs spherical shots of different sizes and materials to introduce compressive residual stress in the surface layers of metals, thereby improving their mechanical integrity when subjected to cyclic loading and/or a corrosive environment. However, this technique is also characterized by substantial surface roughening, high consumables cost, and workpiece contamination. Over the past few decades, a number of alternative peening techniques have been developed to overcome these limitations. Among them, water cavitation jet peening (WCP) has yielded promising preliminary results that point its ability to further extend fatigue life, reduce surface roughening, and lower equipment and operating costs. Nevertheless, the scientific understanding of this process is limited at present. Consequently, there is a need for further studies aimed at developing detailed fundamental understanding of the cavitation jet peening process, and exploring its potential and adequately characterizing the process to meet the demanding requirements set by industry, especially for aerospace applications.

1.1   Peening Techniques

Peening techniques have been extensively used in industry to improve the fatigue life of components subjected to fatigue and corrosion. The most common among these techniques, namely Shot Peening (SP), employs localized plastic deformation caused by shots of different sizes and materials to introduce compressive residual stress in metal surfaces, thereby improving their resistance to crack initiation and propagation. However,

1

this technique is also characterized by contamination and substantial surface roughening, which can lead to unexpected failures in low cycle fatigue (LCF) loading situations [1, 2]. Over the past few decades, a number of alternative peening techniques have been developed to overcome these limitations. Laser shock peening (LSP) is capable of introducing high compressive residual stresses at very large depths with minimal surface modification [3, 4], but it requires long processing times, special surface preparation, and expensive equipment. Deep rolling uses rollers to create a highly cold worked surface as well as a compressive layer of residual stress, and has been investigated for a number of different applications [5-7], . While it has been shown to yield substantial improvements in corrosion and fatigue life, it is limited in its applicability to simple geometric features and not applicable to thin-walled components [8]. Waterjet peening (WJP) has also been evaluated by a number of researchers [9-13]. It employs high speed water droplets as the peening medium, and it has yielded good results in introducing compressive residual stresses in metal surfaces. Flexibility, limited surface roughening and negligible workpiece contamination are significant advantages of WJP over conventional shot peening [14]. The greatest limitation of WJP is its demanding pressure requirements (>200 MPa), which is one order of magnitude higher than the requirement for water cavitation peening (WCP) [15].

1.2   Water Cavitation Peening

Water Cavitation Peening (WCP) is a surface integrity enhancement process whose purpose is to improve the material response to fatigue and corrosion of metallic components. In its most common configuration, cavitation is generated by injecting a high speed jet into a water filled chamber where the component surface to be treated is

2

submerged. The vapor-filled bubbles created by the strong velocity fluctuations within the mixing layer are delivered by the fluid flow to the material surface, where shock waves and re-entrant jets are generated upon bubble collapse, causing plastic deformation of the material surface [16, 17]. A schematic of the water cavitation peening process in the submerged configuration is shown in Figure 1-1.

Inner Jet, V_{in}

Treated Surface
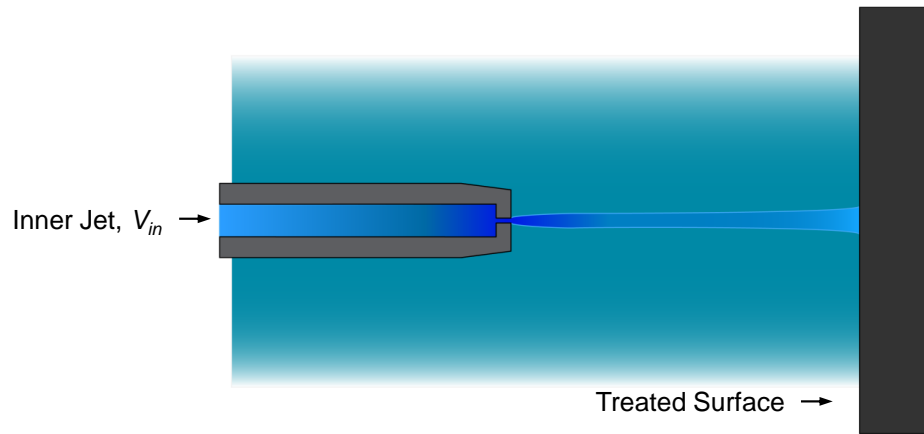
Figure 1-1 Water Cavitation Peening in submerged configuration.

A few studies have investigated the effect of WCP on materials such as aluminum alloys and steels, demonstrating the capability of the process to introduce compressive residual stresses [15, 18] in the surface layer of the materials while limiting the surface roughening typical of other mechanical surface treatments. Fatigue life was also shown to be improved by the process [19], although studies reporting direct comparison between WCP and other techniques are very limited in number and extent of discussion [20].

In spite of the advantages of WCP, there are significant limitations preventing the adoption of this technology by the aerospace industry. These limitations include, but are not limited to, the limited process flexibility due to the requirement for the part to be

3

submerged in water, limited knowledge of the effect of process parameters such as jet velocity on the process performance, and finally the lack of knowledge of the effect of nozzle design on the overall process performance.

1.3   Research Objectives

In light of the aforementioned limitations, this thesis aims to research a novel water cavitation peening process utilizing a *co-flow* configuration to introduce beneficial compressive residual stresses into aerospace materials. The specific objectives of this research are as follows:

1. Experimental characterization of the flow in co-flow water cavitation peening.
2. Experimental characterization of the nozzle geometry effect in co-flow water cavitation peening.
3. Estimate of the compressive residual stresses from pitting analysis in water cavitation peening.

These research objectives are accomplished through a comprehensive literature review of the prior work, followed by scientific studies and rigorous experimental validation of the approach proposed.

1.4   Research Approaches

The co-flow WCP process configuration relies on the same principles used by the submerged WCP process configuration while relaxing the requirement for both the nozzle and the part to be submerged. Cavitation is generated by artificially submerging the high

pressure water jet in a low speed jet that is concentric around the high speed jet. A schematic of the co-flow WCP process is shown in Figure 1-2.
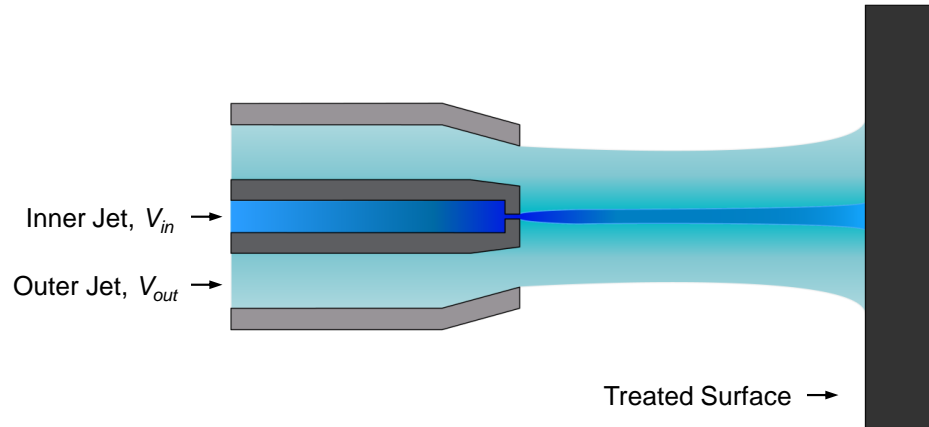
Figure 1-2 Water Cavitation Peening in co-flow configuration.

Similar to the submerged case, the shear boundary layer where the high speed inner jet interacts with the lower speed outer jet generates vapor-filled cavitation bubbles that are transported by the flow to the surface of the metal part where they collapse and produce shock waves and re-entrant micro jets, which in turn produce localized plastic deformation. In order to systematically investigate the co-flow WCP process characteristics, it is necessary to address several gaps in scientific knowledge. These include the effects of the inner and outer jet velocities and of the nozzle standoff distance on process performance, the effect of nozzle design parameters on process performance, and the effect of the flow conditions on the pressure exerted on the metallic surface and the resulting residual stress characteristics. Figure 1-3 summarizes the research approach designed to address these gaps in knowledge through specific tasks.

5

In order to investigate and understand these effects, a laboratory-scale system capable of implementing the co-flow WCP process is required. The system must include three major components: (1) a power unit, including the pumps, providing the two distinct flows shown in Figure 1-2, (2) a test bed where samples of different sizes can be peened, and (3) a co-flow nozzle adequately designed to generate a suitable amount of cavitation necessary to cause plastic deformation in metallic components. The design and fabrication of the co-flow WCP system is addressed in Task 1 of the research approach.
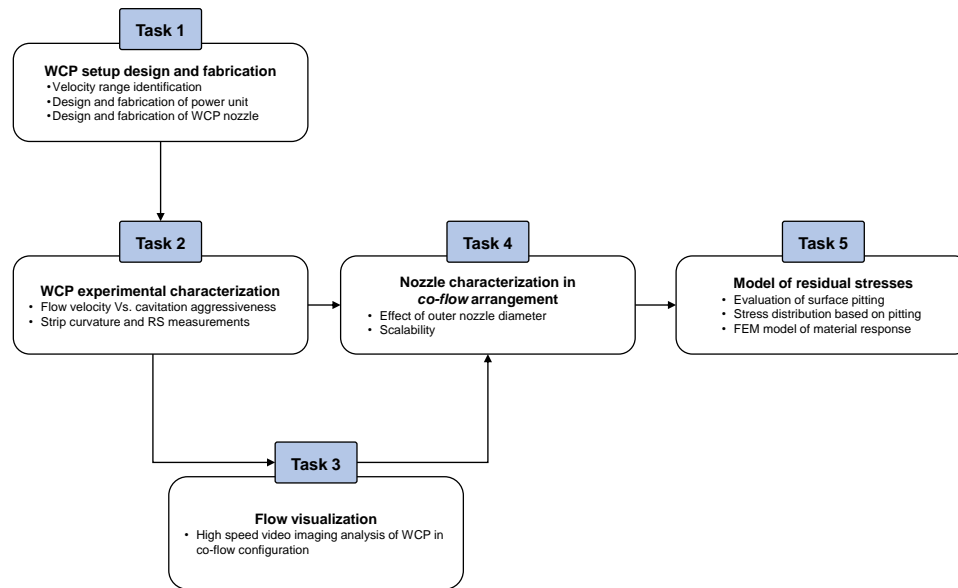
Figure 1-3 Research approach.

The effect of jet velocities and standoff distance on the performance of the co-flow WCP process is investigated in Task 2 by means of accelerated erosion tests [21] and strip curvature tests (Figure 1-4). Accelerated erosion tests are conventionally used in hydraulic applications to investigate the resistance of engineering materials to cavitation. Several previous studies have used this technique to assess the cavitation intensity in the context of peening [15] or cutting processes [22], under the assumption that the highest cavitation

6

erosion (and therefore cavitation intensity) will translate into the best flow conditions for the peening process. It should be noted that while mass loss is not desirable in peening, it serves to quantitatively establish the flow conditions that yield the most intense cavitation. Once cavitation intensity is established via the accelerated erosion tests, actual peening tests are performed by exposing the metal surface to the cavitating jet for a short duration to induce residual stresses without any mass loss.

Compressive residual stresses in the metal surface are a desired outcome of the peening process. Their evaluation is generally done by techniques such as X-ray diffraction (XRD) and hole-drilling, which are expensive and time consuming. In contrast, strip curvature tests have been extensively used in industry as a fast method to evaluate the peening performance [23, 24]. The strip curvature produced by the plastic deformation generated in the peening process is used as an indirect measure of the change in compressive residual stresses produced in the metal surface. Once the optimum peening conditions are identified, through-the-depth residual stress distribution (profile) is determined via the X-ray diffraction method.
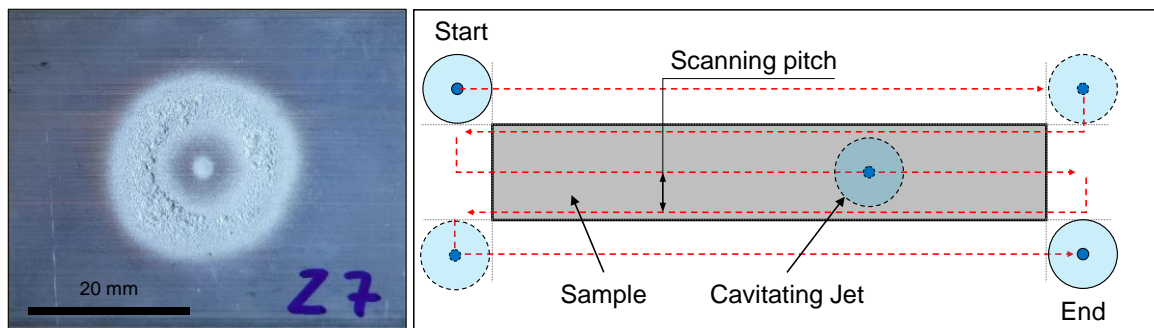
Figure 1-4 (Left) Accelerated erosion test crater and (Right) strip curvature test peening path.

Following the jet velocity study, the effect of nozzle geometry on cavitation intensity and on the process capability are evaluated in Task 3 of the research approach. The goal of this task is to identify the nozzle features that influence the cavitation intensity and to provide an understanding of how the cavitating flow operates and how it can be enhanced. The key aspect of this study is the investigation of the scalability of the co-flow jet and its performance, which are of great importance for the successful adoption of this technology by industry. Three co-flow WCP nozzles of different sizes but with the same normalized dimensions of the key nozzle features are fabricated and evaluated through experiments. Other aspects of the nozzle study include the investigation of the influence of the inner and outer jet orifice diameters and, analogous to the work of Vijay et al. [22], the effect of nozzle offset on the cavitation cloud.

Task 3 of the research approach involves high speed video imaging (Figure 1-5) and associated analyses that are used to characterize the cavitating flows produced by the different nozzle geometries and to explain the experimentally observed trends.
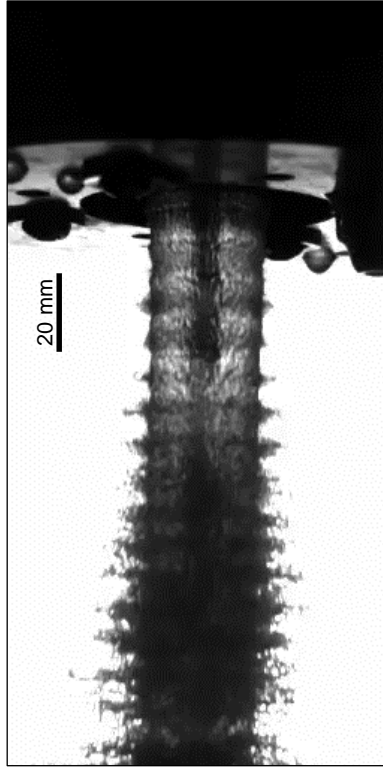
Figure 1-5 High speed video imaging of co-flow cavitating flow at 14,000 FPS.

Finally, Task 5 of the research approach employed in this thesis addresses the development of a semi-empirical model for the estimate of the residual stress introduced by the co-flow WCP process. The model will be developed in three steps. First, pitting tests are conducted on mirror polished samples to investigate the pit geometry generated by WCP under several flow conditions. The information gathered by these test is used to calculate the strain characterizing the single pits and estimate the stress necessary to generate the observed plastic deformation. Finally, the residual stresses induced in the material are estimated via a mechanical model implemented in a finite element software (ABAQUS). Input to this model consists of the stress distribution determined in the previous step, and the outcome is validated against the results previously obtained.

9

1.5   Dissertation Outline

The outline of the thesis is as follows. The introductory chapter is followed by a thorough literature review of the topics relevant to this thesis as detailed in Chapter 2. Chapter 3 focuses on the co-flow WCP system design and fabrication while Chapter 4 covers the investigation of the effect of jet velocities in co-flow water cavitation peening. Chapter 5 focuses on the experimental investigation on the effect of nozzle design on cavitation intensity and peening capability. Chapter 6 covers the development of a semi-empirical model for the prediction of residual stresses in aluminum 7075-T651. Finally, the main conclusions and original contributions of the thesis are summarized and suggestions for future work are presented in Chapter 7.

CHAPTER 2.   LITERATURE REVIEW

This section contains a review of prior work in areas considered relevant to this thesis. The specific areas include: (1) Peening processes, (2) Water cavitation peening, (3) Cavitation intensity, and (4) Cavitation erosion.

Peening processes have been extensively studied for a number of applications and materials. All available peening methods share the common goal of improving the surface resistance to fatigue failure and corrosion by introducing compressive residual stresses in the metallic surface layers. Therefore, a review of existing peening techniques can help in establishing the relative merits and limitations of the various methods. Cavitation intensity and erosion are known phenomena and have been extensively studied. Much of this prior work is generally focused on limiting cavitation erosion rather than using cavitation for beneficial purposes. Information on cavitation-material interaction is available in the literature and can be used to understand how engineering materials are affected by cavitation.

2.1   Peening Processes

Peening techniques, such as shot peening, deep rolling, and laser shock peening, are known to significantly increase the fatigue and corrosion resistance of metals. Their effect is localized at the surface of metallic components, and their mechanism is characterized by microstructural changes (work hardening), the introduction of compressive residual stresses, and an (unwanted) increase in surface roughness. Each peening process displays a characteristic combination of these aspects, with different contributions to the final outcome in terms fatigue resistance [25].

11

Figure 2-1 Shot peening (SP).

The most common peening technique is Shot Peening (SP), which employs mechanical shots of different sizes and materials to introduce compressive residual stress in the metal surface, and is accompanied by substantial surface roughening. Evidence of beneficial effects can be found in a number of studies performed on a wide range of materials and applications [23, 26-28]. These studies focus on the experimental characterization of material response, such as residual stress and fatigue life, for different peening conditions. Both finite element and semi-empirical methods have been proposed for calculation of the residual stresses [29-32]. Residual stress relaxation due to cyclic loading is also a topic of interest, since, over time, it can neutralize the beneficial effect of peening [33-35]. Additional impetus for industrial use of these techniques is derived from the development of special peening methods such as warm peening [35], stress peening [36], and ultrasonic stress peening [37, 38].

Laser shock peening (LSP) was developed in the 1970s and has become popular in recent years as a result of advances in laser technology. In its most common form, LSP employs one of three types of lasers: Nd-glass (wavelength λ= 1053 or 527 nm), Q-switched Nd:YAG (λ= 532 nm), and XeCl-Excimer (λ=308 nm) [39]. It can be performed

in two configurations, namely *direct* and *confined* ablation, and is characterized by larger and deeper residual stresses compared to conventional shot peening [40-42].
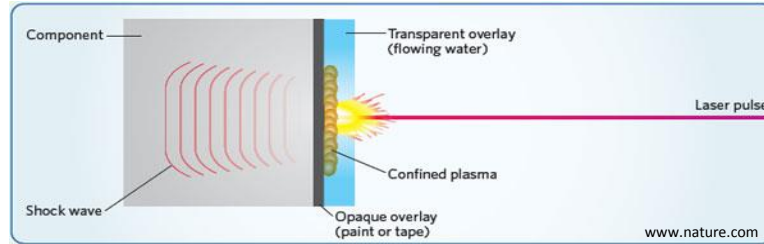
Figure 2-2 Laser shock peening (LSP).

Surface finish strongly depends on the laser settings, leading to a wide range of possible surface roughness outcomes [3, 25, 43, 44]. As in shot peening, several studies have been reported on different materials subjected to different peening conditions [3, 41]. Fabbro et al. [40, 45, 46] studied analytically and experimentally the impulse pressure generated by the laser-produced plasma cloud in the confined case [40], and in a later study presented a complete model to predict the residual stresses generated in the process [47]. Finite element models are also available to predict residual stresses caused by laser shock peening [48-51]. Yao et al. [52-54] investigated micro scale laser shock peening, and proposed a model for the material deformation caused by the laser-induced shock wave [55].

Water jet peening employs water droplets as the peening media [9, 56]. The effect of this process on aluminum and titanium alloys has been investigated in several studies [10, 57, 58] and models of residual stress formation have been proposed [58-62]. The greatest limitation of this technique is its high pressure requirement (>200 MPa) combined with the small treated area. Substantial roughening and erosion can occur when the peening time is not controlled properly [63]. Grinspan et al. [11, 12, 64, 65] investigated the effect of

13

mineral oil as the peening medium. According to these authors, mineral oil (and its higher viscosity) increases the process capability in terms of the maximum residual stress, while reducing the potential for erosion and surface damage [66].

Figure 2-3 Water jet peening (WJP).
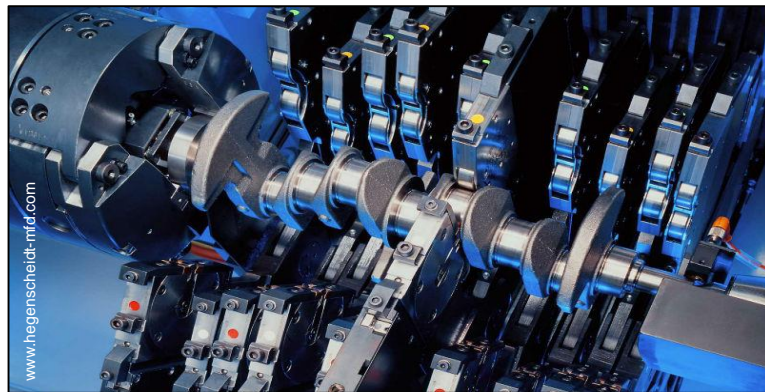
Figure 2-4 Deep rolling (DR).

Deep rolling is another notable peening technique which employs a hardened sphere or cylindrical roller to induce cold work in metal surfaces [67]. Its application is restricted by the tool and component geometry, and the high loads involved make this process unsuitable

for thin-walled parts. It is characterized by high compressive residual stresses and exceptional surface finish [25], and it is therefore often used on crankshafts [67], ball bearings, and other components subjected to sliding and fretting fatigue [6]. Roller burnishing is a technique similar to deep rolling in that it employs the same type of tooling and procedures, but with the focus shifted toward the surface finish rather than compressive residual stress [8, 68-70]. While a limited number of studies on the prediction of sub-surface stress states in deep rolling have been reported [67, 71], modeling of the roller burnishing process has drawn considerable attention in the scientific community in recent years [72-74].
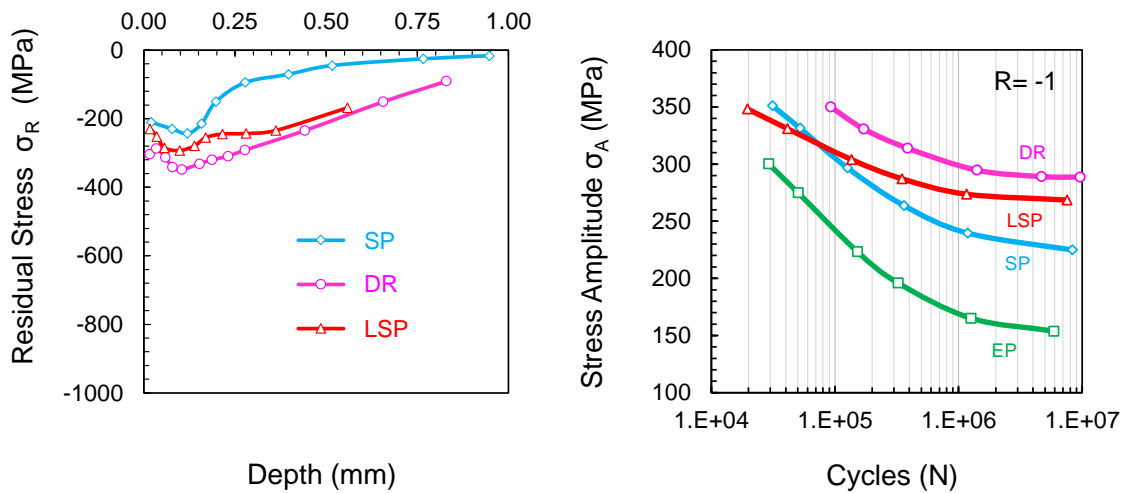
Figure 2-5 (Left) Residual stresses introduced in Aluminum 7075-T73 by shot peening (SP), deep rolling (DR) and laser shock peening (LSP) and (Right) fatigue life comparison at inversion (R=-1) including the electro polished (EP) baseline state. (Wagner, 2011)

Despite the availability of a large number of studies of the aforementioned peening techniques, studies directly comparing their relative performance are scarce. Noteworthy are the works of Wagner et al. [23, 25], Altenberger et al. [5], Nalla et al. [75], Rodopoulos et al. [76], and Luong et al. [77]. These studies are primarily focused on the high cycle

15

fatigue (HCF) response of the treated surfaces and consistently report improvements in fatigue life for aerospace alloys treated with laser shock peening and deep rolling over those treated with conventional shot peening.

2.2 Water Cavitation Peening (WCP)

The first observation of the peening capability of cavitating jets was published by Blickwedel et al. [78]. Since then, only a handful of researchers have investigated this process, with the result that only a few scientific studies are available in the open literature today.

As discussed earlier, water cavitation peening in the *submerged* configuration employs a single high-speed jet surrounded by stationary water to produce cavitation. Soyama et al. [15] reported high surface compressive residual stresses in 304 and 316 stainless steels for a jet pressure of 20 MPa and exposure times as little as 30 s. Subsequently, improvements in fatigue life were reported for different metals such carburized steel [79], aluminum alloys [80], tool and spring steels [81, 82], and titanium [83, 84]. Studies comparing WCP to shot peening are limited. Soyama et al. [19, 79] reported higher fatigue life (in HCF) for cavitation peened samples over shot peened samples, despite lower compressive residual stresses introduced in the material. An explanation offered for this finding is that WCP results in less surface roughening than shot peening, which plays a significant role in HCF.

16
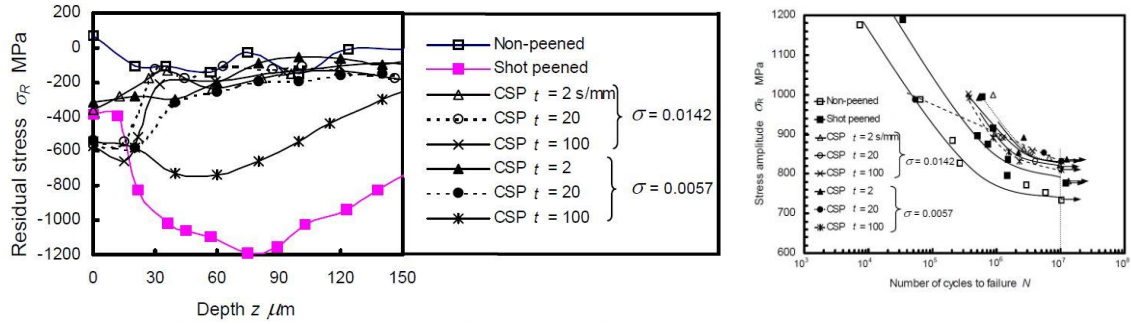
Figure 2-6 (Left) Residual stresses introduced by Cavitation Shotless Peening (CSP) in JIS SCM415 steel for different cavitation numbers σ and (Right) S-N diagram for rotating beam bending test at R= -1 (Soyama, 2004).

Nozzle shape and geometry effects were investigated by Soyama et al. [85, 86]. In these studies, cavitation aggressiveness was assessed by an accelerated erosion test, similar to that described in [21]. Ju et al. [87, 88] proposed a cavitation nozzle with aeration to increase the flow aggressiveness. Grinspan et al. [89, 90] investigated a mineral oil based cavitation process as an alternative to water in order to increase the compressive residual stresses induced in the material and to decrease surface roughening. Peening parameter selection and optimization for the *submerged* configuration was investigated by Soyama et al. [19, 91]. Ju et al. [92] investigated the effect of incident angle on the WCP process capability.

There are just a few modelling studies of this process. Ju et al. [93, 94] proposed a finite element method combined with a dislocation density based approach to predict the residual stresses induced by cavitation peening. Pressure magnitude and impulse duration are estimated from the cavitation literature and therefore results are not conclusive. Takakuwa et al. [95] estimated the depth of surface modification layer induced by cavitation peening. The practical use of the modeling results is limited in that it first requires the measurement of the surface residual stresses induced by the process. Finally, Vijay et al. [22, 96]

17

presented a computational fluid dynamic analysis of submerged cavitating jets by analyzing the cavitation numbers produced in the mixing layer.
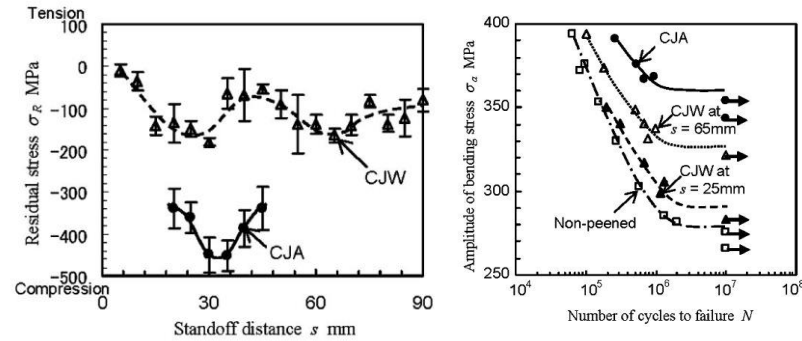
Figure 2-7 (left) Surface residual stresses in JIS SUS316L as a function of nozzle standoff distance s for submerged (CJW) and co-flow (CJA) configuration and (Right) S-N diagram for plate bending test at R= -1 (Soyama, 2007).

Water cavitation peening in the *co-flow* configuration employs a low speed, high flow rate jet to locally submerge the high speed jet [18, 97]. A single comparative study of the two flow arrangements was reported by Soyama [98] where compressive residual stresses and fatigue life obtained with the *co-flow* configuration were shown to be higher than there are in submerged configuration. Marsh et al. [99] proposed a co-flow configuration based oil cavitation peening process in which scanning pitch, stand-off distance and scanning feed rate were investigated and an optimum was found. Takakuwa et al. [100] also investigated the effect of scanning pitch for cavitating jet with overlapping treatment. To the best of the author's knowledge, the effect of flow velocities on the material response and nozzle geometry in the *co-flow* arrangement have not been reported in the literature. It is worth noting that, despite several studies that have investigated the effect of jet pressure in both *submerged* and *co-flow* configurations, the results obtained are specific to the

18

systems used and cannot be replicated, particularly since fundamental details about the nozzles such as contraction ratios and orifice length are not reported.

2.3   Cavitation Intensity

Cavitation intensity is an important metric utilized to characterize the effectiveness of cavitating jets. It measures the intensity of the liquid/solid interaction and it is assessed indirectly by means of the accelerated erosion test, as prescribed by the ASTM standard G134 [21]. While the goal of this test is to evaluate the resistance of different materials to cavitation, accelerated erosion tests can also be used to assess relative effectiveness of the cavitating flows produced by different nozzles or flow conditions, and studies on cavitating jets have extensively used this method to evaluate the optimum processing parameters [85, 86, 101]. Moreover, a number of studies are found in literature that focus on maximizing cavitation intensity. Different approaches are proposed, generally concerning one of the following three aspects: (1) fluid properties, (2) nozzle geometry, and (3) flow conditions.

The correlation between fluid properties and cavitation erosion has been investigated by a number of authors for a wide variety of applications. The nuclear sector in particular has sparked interest in the cavitation behavior of conventional fluids such as high temperature water, and other fluids such as sodium [102], mercury, lead-bismuth, and lithium at temperatures as high as 250°C [103, 104]. Hattori et al. [105] reported an increase in the erosion rate for water of 1% per °C for temperatures T between 5° and 45° C, followed by a decrease of 2% per °C for T between 45 and 80°C due to cushioning effects. Other studies confirm similar results for the effect of temperature in water cavitation erosion [106].

19
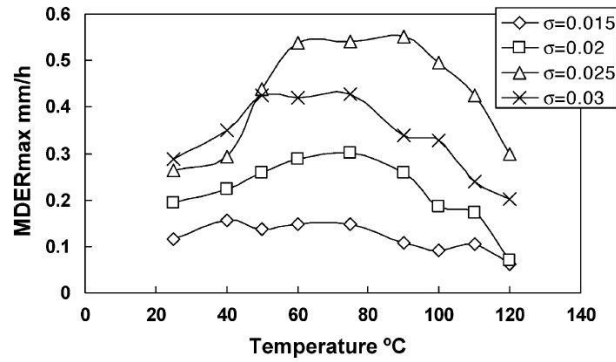
Figure 2-8 Maximum mean depth of erosion rate (MDERmax) as a function of water temperature for different cavitation numbers σ (Hattori, 2006).

A major focus of this thesis is the evaluation of how nozzle geometry affects peening applications, therefore limiting this study to the fluid water at room temperature. Nevertheless, a lack of interest from the research community in water-base fluids developed to enhance the cavitating jet intensity is noted, and could be of interest for future development.

Nozzle design is a fundamental aspect of water jetting, playing a key role in both cavitating and non-cavitating jets. In the case of submerged cavitating jets, several studies have proposed nozzle designs with the goal of maximizing cavitation intensity. Chahine et al. developed a self-resonating nozzle [107-109] producing pulsed cavitation that is capable of improving cavitation erosion in mining and cleaning operations in both submerged and "in air" configurations. Vijay et al. investigated the effect of nozzle geometry on cavitating jets for cutting applications in both submerged [110] and co-flow configurations [22]. Nozzle shape, outer flow rate, and outer flow diameter were among the parameters investigated in the studies. It was found that the co-flow configuration produces higher cavitation intensity compared to the submerged case under equivalent conditions. Soyama

20

et al. have performed several studies on the effect of nozzle geometry on cavitation intensity in the submerged configuration. First, an evaluation of the upstream geometry of the nozzle was performed, and results for a cylindrical, conical and a horn nozzle [111] were presented. Pressure-sensitive films were used to measure the impulsive pressures produced by the different nozzles. While the horn nozzle resulted in the highest impulsive pressure, the cylindrical nozzle was shown to produce the highest mass loss in the accelerated erosion tests, therefore resulting in the highest cavitation intensity, as defined by [21].
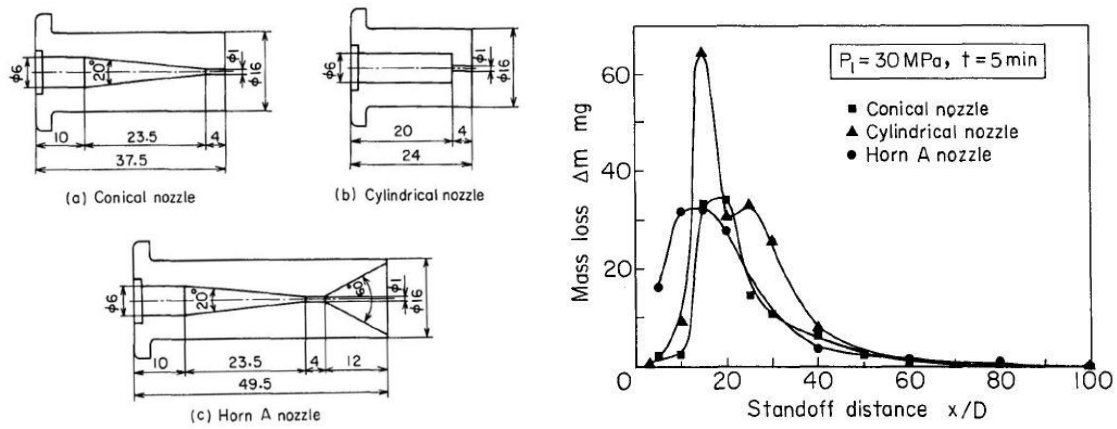
Figure 2-9 (Left) Conical, cylindrical and horn nozzles for submerged configuration and (Right) relative accelerated erosion tests results as reported by Soyama et al (1995).
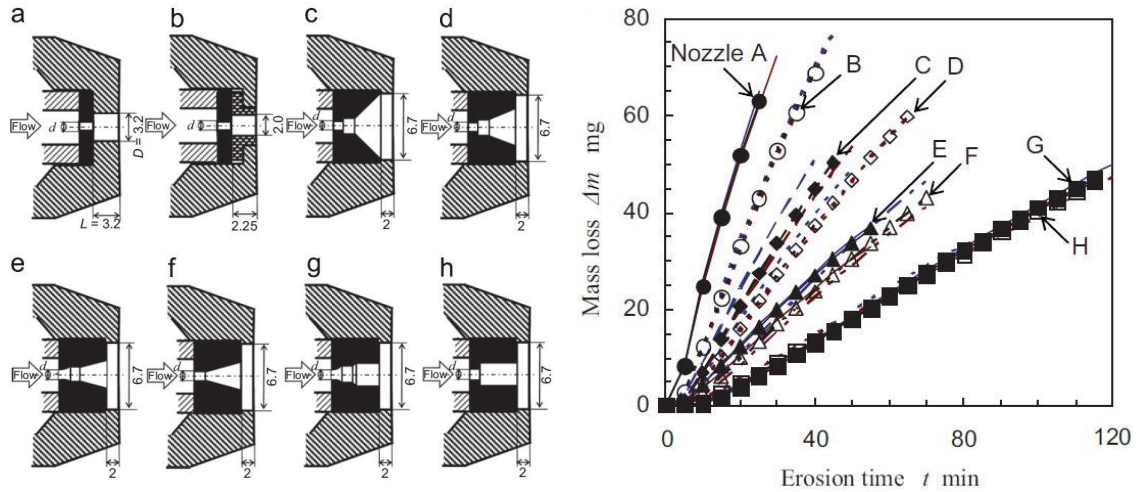
Figure 2-10 (Left) Cylindrical nozzles for submerged configuration and (Right) relative accelerated erosion tests results as reported by Soyama et al (2013).

Another study which investigated the effect of nozzle outlet geometry on cavitation intensity [86], showed that the nozzle features located downstream from the high pressure orifice had a tremendous impact on the cavitation intensity. While these results have substantial technological relevance, there are no reported efforts to explain or generalize the observed results. Another study from the same group investigated the effect of orifice geometry on cavitation erosion [85]. In this study, the optimized nozzle geometry developed in [86] was compared to several other nozzle designs (Figure 2-10), which differed in shape and dimensions. The study concluded that cavitation erosion and the optimum standoff distance strongly depend on the nozzle geometry, but little insight into the effect of the single nozzle features on the cavitation intensity and ways to optimize them can be inferred from these studies. Finally, Soyama proposed a nozzle design including a cavitator [112], similar to what was previously proposed by Johnson et al. [107, 108]. The study experimentally optimized the cavitator geometry and reported a substantial increase in cavitation intensity over the regular cylindrical nozzle developed in [86].

Surface roughness produced in the submerged WCP configuration has also been studied. Li et al. [113] investigated the effect of surface roughness on cavitation intensity and the specific energy consumption for an organ-pipe nozzle, and discovered a correlation between the average roughness height and the thickness of the viscous sublayer in the turbulent flow. Their results show that higher inlet pressures, and therefore smaller viscous sublayers, require smoother surfaces to maintain the flow in the beneficial region, as shown in Figure 2-11.
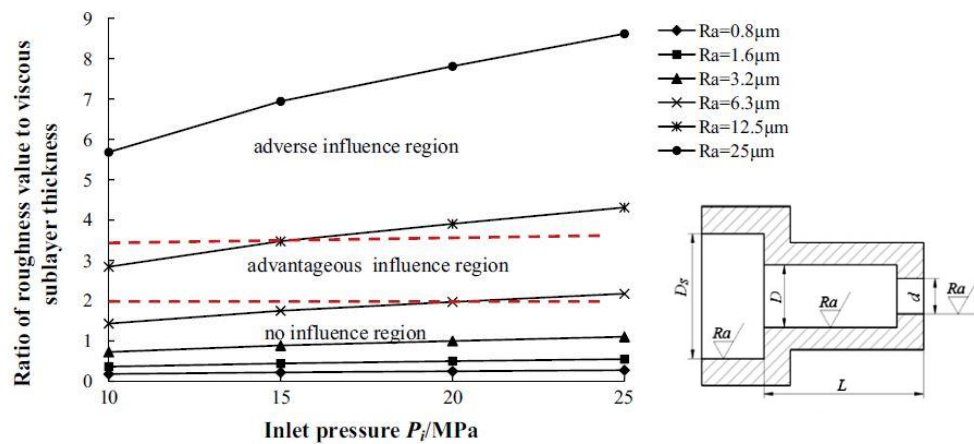
Figure 2-11 Ratio of nozzle roughness to viscous sublayer thickness as a function of inlet pressure P_i.

While the effect of nozzle geometry on cavitation intensity in the submerged configuration has received some attention from the research community, the same cannot be said for co-flow cavitating jets. Among the few studies on the co-flow configuration, the study by Vijay et al [22] investigated the effect of the outer flow diameter and the nozzle offset on cavitation intensity, but failed to generalize the results by not adjusting the outer flow rate to compensate for the different nozzle geometries. As a result, it is difficult to conclude whether the observed trends are due to the nozzle geometry, or due to the combination of nozzle geometry and consequent variation in outer flow velocity.

23

Moreover, since their study is mainly focused on cutting applications, and considering the nozzle geometry and flow velocities reported, it is fair to assume that the experiments were conducted in the center regime, where the cavitation erosion is focused in the center of the jet as seen in [114]. Soyama et al. have conducted a few studies on co-flow cavitation peening [18, 97, 98, 101]. Each of these studies uses a different nozzle, and all lack a detailed description of the nozzle geometry. Investigation of the effect of the nozzle on cavitation intensity is limited to the identification of the optimum outer diameter of the inner jet nozzle, as reported in [97].
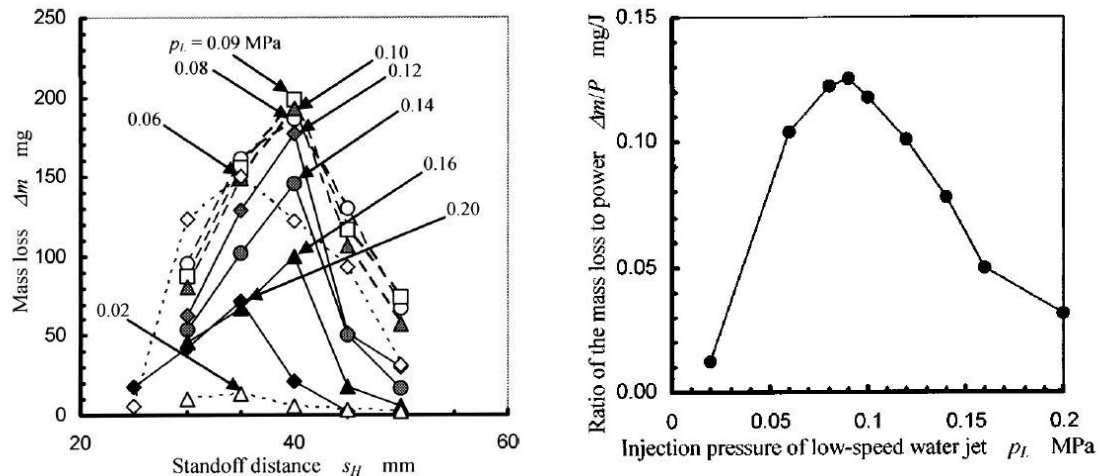
Figure 2-12 (Left) Cavitation intensity (mass loss) as a function of standoff distance for different outer flow pressures P_L, and (Right) cavitation intensity per unit power as a function of outer flow pressure.

Finally, the effect of flow parameters such as the jet velocities and the standoff distance on cavitation intensity have also been investigated for both the submerged [15, 22, 115, 116] and co-flow configurations [18, 22, 97, 114]. While an optimum cavitation number and jet pressure is shown to exist, the vast majority of the studies fail to report jet

velocities along with the nozzle geometry (Figure 2-12), thereby making it difficult to understand how the jet pressure/velocity affect the WCP process performance.

2.4 Cavitation Erosion

Cavitation is known to occur under several flow conditions and is responsible for severe damage of components such as hydrofoils, impellers, valves and pumps. This section offers a review of key aspects of cavitation and erosion that are believed to be relevant to the cavitation peening process.
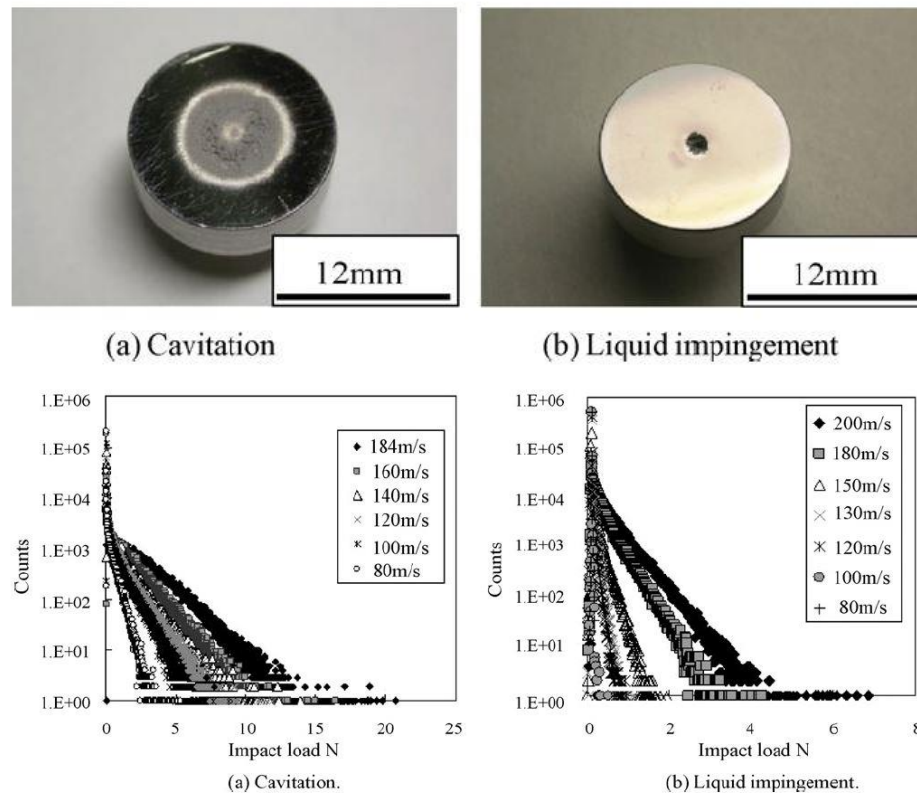
Figure 2-13 Comparison of cavitation erosion with liquid impingement erosion, (Top) crater surface and (Bottom) distribution of impact load for different jet velocity (Hattori 2006).

Submerged jets have been investigated for several decades [117-119]. Unfortunately, the majority of these studies are focused on flows at low Reynolds numbers, low pressure

25

drop and large nozzles, which are not representative of the peening process. Soyama et al. [101, 111, 120, 121] investigated submerged high speed jets through direct visualization of the cavitating flow generated by different types of nozzles. Vijay et al. included the erosion characteristic [110] and presented a computational fluid dynamics study of the mixing layers [96] as a means to assess the nozzle's cavitation effectiveness. Hattori et al. [122] evaluated the liquid impingement erosion rate versus the cavitation erosion rate (Figure 2-13). Their study provides useful insights into the selection of the jet velocity range used in this research and shows how cavitation bubbles can produce higher impact forces compared to impinging droplets. The mechanism of pit formation and bubble-wall interaction has been the object of intensive research. The seminal work of Plesset et al. [123] was followed by a number of studies [124-126] leading up to the recent works of Dular [16] and Tzanakis [17] where pit formation was captured and analyzed. Choi et al. [127] presented a finite element analysis of pit formation and studied the effect of loading and material properties on the material response to impact loading.
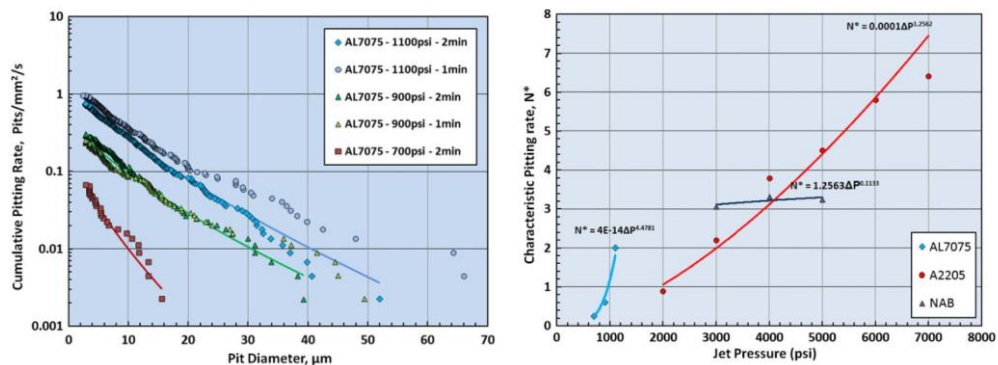
Figure 2-14 (Left) Cumulative pitting rate as a function of pit diameter for different values of the jet pressure on Aluminum 7075, (Right) characteristic pitting rate as a function of jet pressure for different materials (N*= characteristic pitting rate) (Choi 2012).

26

The pitting rate, coverage time, and incubation time are quantities of great interest in when estimating cavitation erosion. The same quantities are also relevant to water cavitation peening, since coverage and incubation time are measures of the peening time. Choi et al. [116, 128] investigated the scaling of cavitation pitting and erosion caused by cavitating jets, and proposed a useful normalization capable of capturing erosion trends for several engineering materials (Figure 2-14). Franc et al. [129, 130] investigated the effect of material and velocity on cavitation erosion pitting and incubation time for work hardening materials and Chahine et al. [131] proposed a collection of advanced experimental and numerical techniques for the prediction of cavitation erosion.

The impact load generated during cavitation bubble collapse has drawn significant attention over the years. Recent developments in sensing technology have allowed several researchers to count the number of impacts of an impinging cavitating cloud and measure the load distribution [132-137]. An approach developed by Knapp [138], and recently adopted by Carnelli et al. [139, 140] and Tzanakis et al. [17], employs the material surface as a sensor, and involves stress-strain analysis of individual pits to derive the hydrodynamic impulse pressure of cavitation impact. Based on the literature review, there is insufficient understanding of cavitation generation by a high speed jet in the *co-flow* configuration. Moreover, to the best of the author's knowledge, modelling of residual stresses induced by bubble collapse in WCP has not been reported.

27

2.5   Summary

It is clear from the literature survey that:

- Limited investigation has been carried out to evaluate the process capability of co-flow water cavitation peening.

- No work has been reported on the effect of jet velocities on water cavitation peening.

- No work has been carried out to investigate the effect of co-flow nozzle geometry on the water cavitation peening process.

- Limited work has been done on modeling of residual stresses produced in water cavitation peening.

This thesis describes the design, development, experimental characterization, and modeling of the co-flow water cavitation peening process for the introduction of beneficial residual stresses into aerospace materials.

CHAPTER 3. DESIGN AND FABRICATION OF THE WATER CAVITATION (WCP) SYSTEM

The chapter focuses on the design and fabrication of a WCP system for the introduction of beneficial residual stresses into aerospace alloys. This work is motivated by the lack of commercially available WCP systems and the promising improvements obtained by WCP over shot peening results shown in the literature and discussed in the previous section. The WCP system design and fabrication are described in detail, along with the instrumentation necessary to investigate and evaluate the WCP process.

3.1 Approach

The initial approach adopted in the design of the WCP system consisted of the identification of nozzle outlet geometry and the jet velocity combinations capable of producing the level of cavitation intensity necessary to peen a metal surface. The major elements composing the WCP system are:

1. Power Unit
    1. High pressure line (inner jet)
    2. Low pressure line (outer jet)
2. Test section
    1. Test enclosure, gantry system & return line
    2. Co-flow nozzle

The power unit is composed of a reservoir tank and two pumps feeding the inner and outer flow lines, along with the necessary instrumentation (e.g., flow meter) to characterize the

29

flow. The test section includes the WCP nozzle as well as all the elements necessary to conduct experiments effectively and in safety, such as a test enclosure for the collection of the cavitating fluid and a gantry system for automating the nozzle path during peening. The rest of the chapter describes in detail the WCP system and motivates the approaches adopted to address the challenges encountered in the development of the experimental setup.

3.2   System Schematic

A schematic of the WCP system was developed starting from a previous study performed by the same group [99] as well as from other works published by Soyama et al. [18, 97, 101]. The schematic, shown in Figure 3-1, illustrates the operating principle and includes the major components selected for the final system design.

Filtered tap water is collected in a reservoir tank (1), which serves both the centrifugal pump (5) in the outer flow line and the positive-displacement pump (6) in the inner flow line. Both pumps are preceded upstream by strainers (4) and shut-off valves (3). The positive-displacement pump is followed downstream by a pulsation damper (7), as prescribed by the ASTM standard detailing the evaluation of cavitation erosion resistance for engineering materials [21]. A butterfly valve (8) was chosen to control the outer flow line (centrifugal pump), while a variable frequency drive (VFD) was installed on the inner flow line, allowing for precise flow rate control. Flow rates are measured by means of turbine flow meters installed upstream from the nozzle (FI). To minimize flow variations, the outer flow line was connected to the cavitation nozzle through four inlets spaced 90° apart and located at the top of the nozzle. The inlets and the nozzle main cross sectional

30

area were dimensioned with the goal to keep the average outer flow velocity entering the nozzle well below 0.5 m/s.
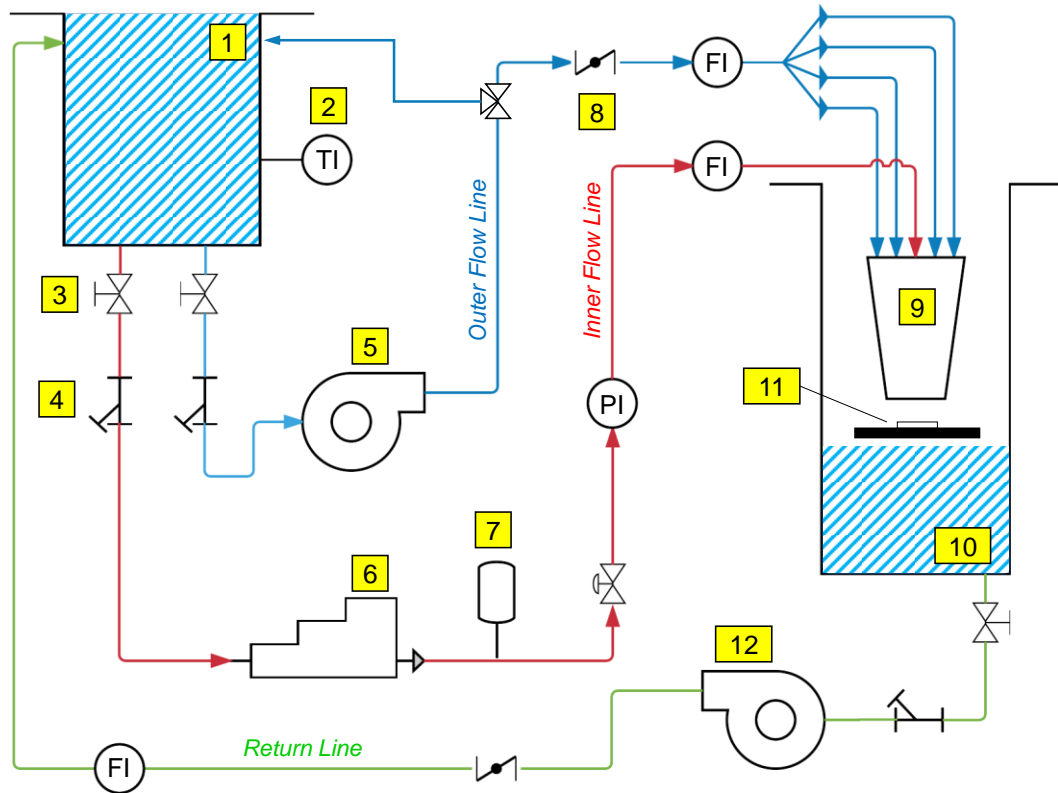
Figure 3-1 Water cavitation peening (WCP) apparatus. (1) Reservoir tank (2) temperature (TI), flow rate (FI) or pressure (PI) indicators, (3) shut-off valves, (4) strainers, (5) centrifugal pumps, (6) positive-displacement pump, (7) pulsation damper, (8) butterfly valve, (9) WCP nozzle, (10) test enclosure, (11) test sample and (12) return pump.

The nozzle was designed with the goal of providing the flexibility necessary to investigate several variables of the process, including the nozzle outlet geometry, while at the same time limiting the overall dimension and weight to fit a mid-sized commercially available gantry system. Finally, the test pit (10) was installed on top of two centrifugal

pumps (12) matching the flow rate capability of the power unit in order to recirculate the peening fluid. A picture of the entire system is shown in Figure 3-2.
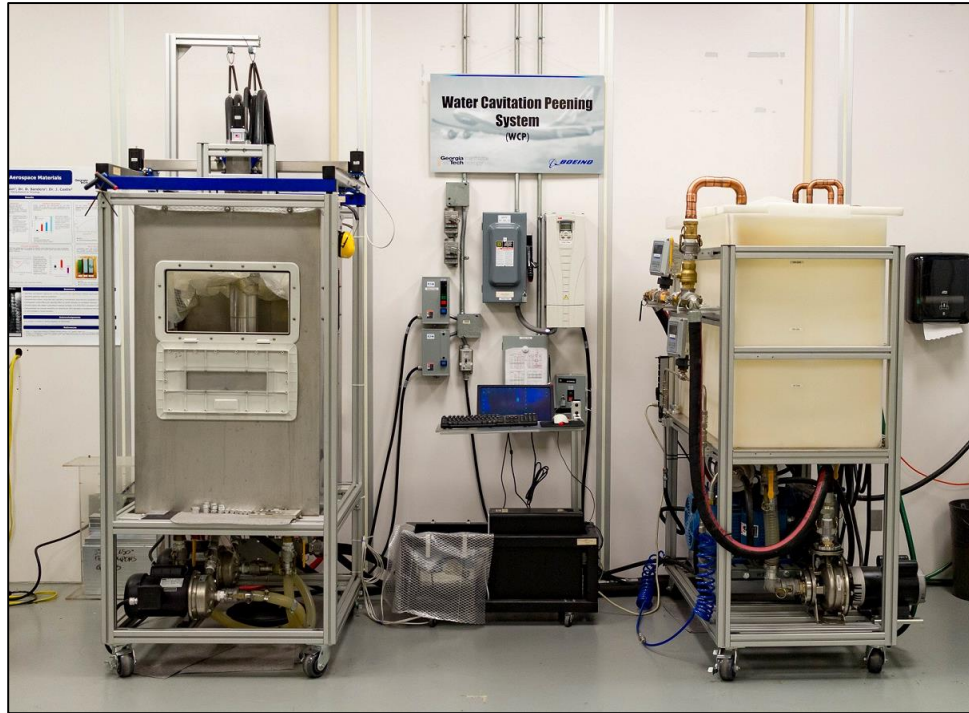
Figure 3-2 Water Cavitation Peening system.

3.3   Power Unit

The power unit includes all the components necessary to supply the nozzle with adequate flow rates for both the high pressure line (inner jet) and the low pressure line (outer jet).

3.3.1   High Pressure Line

The high pressure line is equipped with a CAT 718 positive displacement pump, capable of delivering 0.017 m^3/min (4.5 gpm) of water at 34 MPa (5,000 psi). The pump is coupled to a 20 HP electric motor, whose rotational speed can be varied continuously by

means of a variable frequency drive (VFD). The pump requirements were calculated by assuming a nozzle diameter $D_{in} \sim 0.9$ mm, discharge coefficient $C_D \sim 0.65$ (cylindrical nozzle [85]), and target inner jet velocity of $V_{in} \sim 150$ m/s, as explained in detail in a later section. Stainless steel Swagelok fittings, valves, and piping were selected for the high pressure line, ensuring the appropriate pressure rating and corrosion resistance. An Omega turbine flow meter FTB-1400 with 1% accuracy was chosen measure the flow rate from which the jet velocity could be computed. Other components in the high pressure line include a fine mesh strainer, a pulsation dumper, and a shut-off valve.

3.3.2   Low Pressure Line and Reservoir Tank

The low pressure line is equipped with an Ebara 3U-32-160B-5HP centrifugal pump (Figure 3-3). The pressure and flow rate requirements were calculated assuming a ring-shaped nozzle geometry with outer and inner diameters of ~25 mm and ~12 mm respectively, and a target outer jet velocity of $V_{out} \sim 15.0$ m/s, as explained in a later section. The piping system connecting the pump outlet to the nozzle was carefully sized in order to reduce both concentrated and distributed losses. Copper piping and cam-and-lock type brass fittings were selected for the low pressure line, ensuring the appropriate pressure rating and corrosion resistance. An Omega turbine flow meter FTB-1400 with 1% accuracy was chosen measure the flow rate in the line and thereby compute the jet velocity. All the flow meters were installed according to specifications as shown in Figure 3-4.
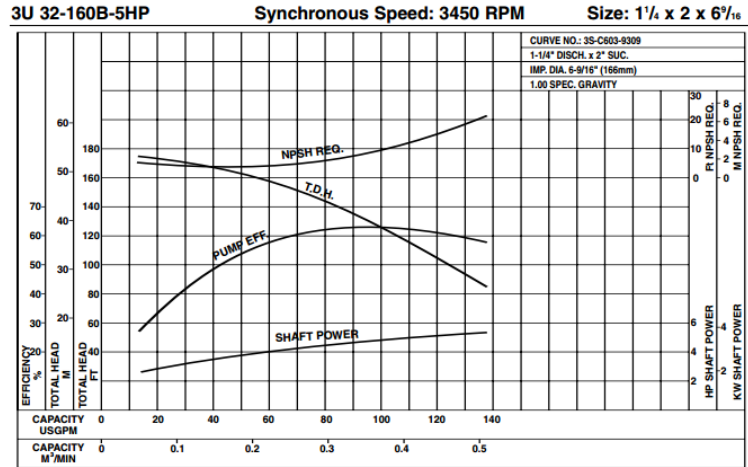
Figure 3-3 Centrifugal pump curve for the EBARA 3U-32-160B-5HP adopted in the power unit. (source: http://www.pumpsebara.com/)
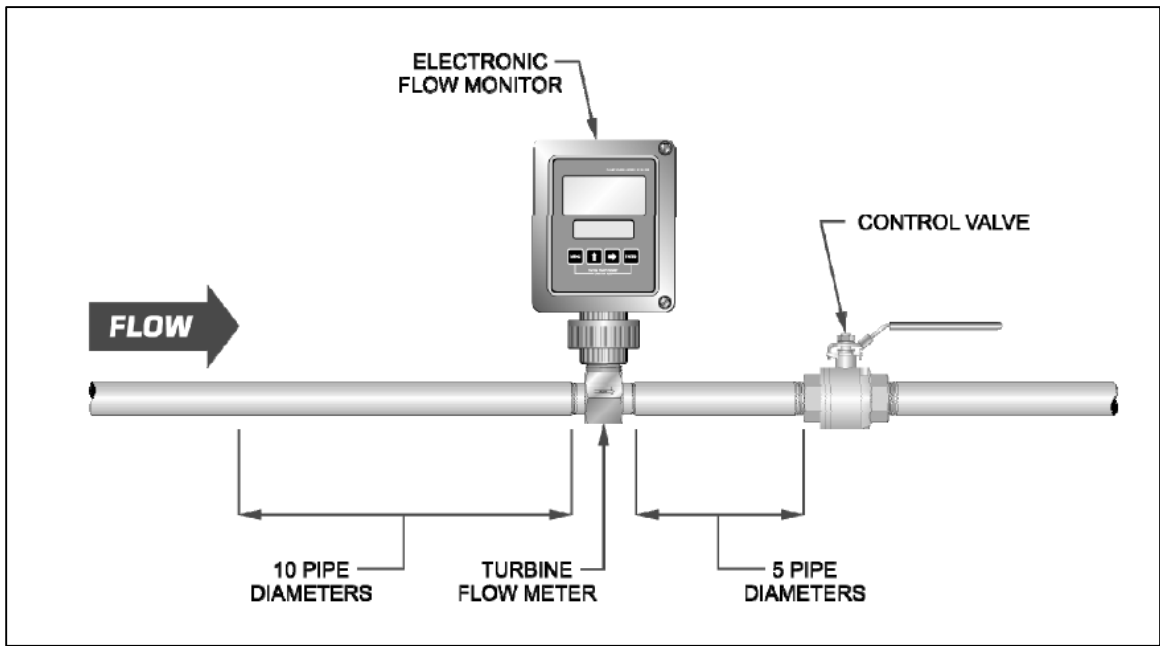
Figure 3-4 Flow meter installation (source: Omega FTB-1400 user's guide).
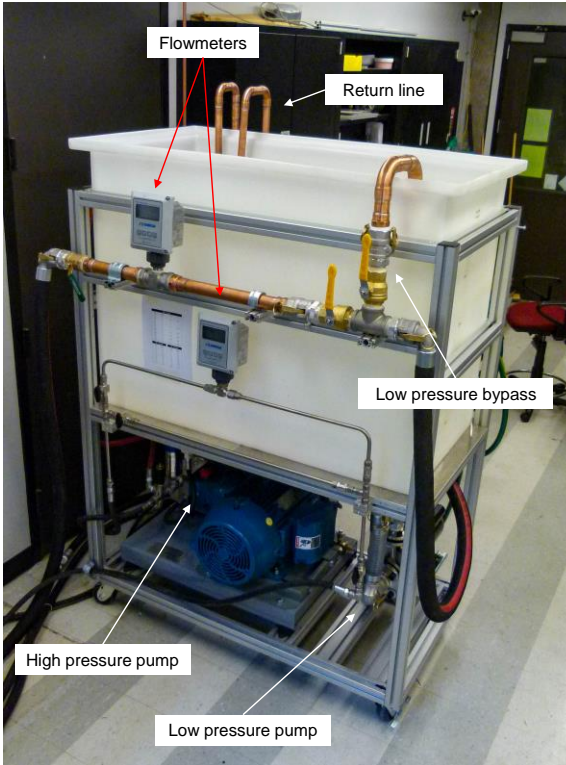
Figure 3-5 Power unit in WCP system.

Coarse flow rate regulation is achieved by means of a bypass valve upstream from the flow meter, while a butterfly valve placed downstream from the flow meter is used for fine adjustments. A detailed view of the power unit is shown in Figure 3-5.

Tap water is stored in a 0.75 m^3 (200 gal) reservoir tank installed on top of the power unit, ensuring the necessary suction head required by the pumps. Baffles were installed inside the tank to prevent any trapped air from circulating in the circuit and causing damage to the pumps.

3.4   Test Section

www.manaraa.com

The test section includes all the components necessary to carry out the investigations of the Water Cavitation Peening process. Components include the test enclosure, the gantry system, the WCP nozzle, and the return line.

3.4.1   Test Enclosure, Gantry System & Return Line

The test pit consists of five welded stainless steel panels, forming an open-top enclosure. The open top is necessary to grant access to the nozzle, which is mounted on a XYZ gantry system placed above the enclosure. Heavy-duty plastic sheeting is used to prevent splashing from the enclosure's open top. The enclosure dimensions are $0.75 \times 0.75 \times 1.25$ m^3, and it sits on top of two centrifugal pumps used to return the water to the main tank, thereby closing the circuit. A window is installed on each side of the enclosure, while a hatch is mounted on the front panel to grant access to the work table located inside the enclosure. The work table is used to hold the samples to be peened and its height can be adjusted as needed (Figure 3-6(a)). A detailed view of the test section is shown in Figure 3-6 (b).
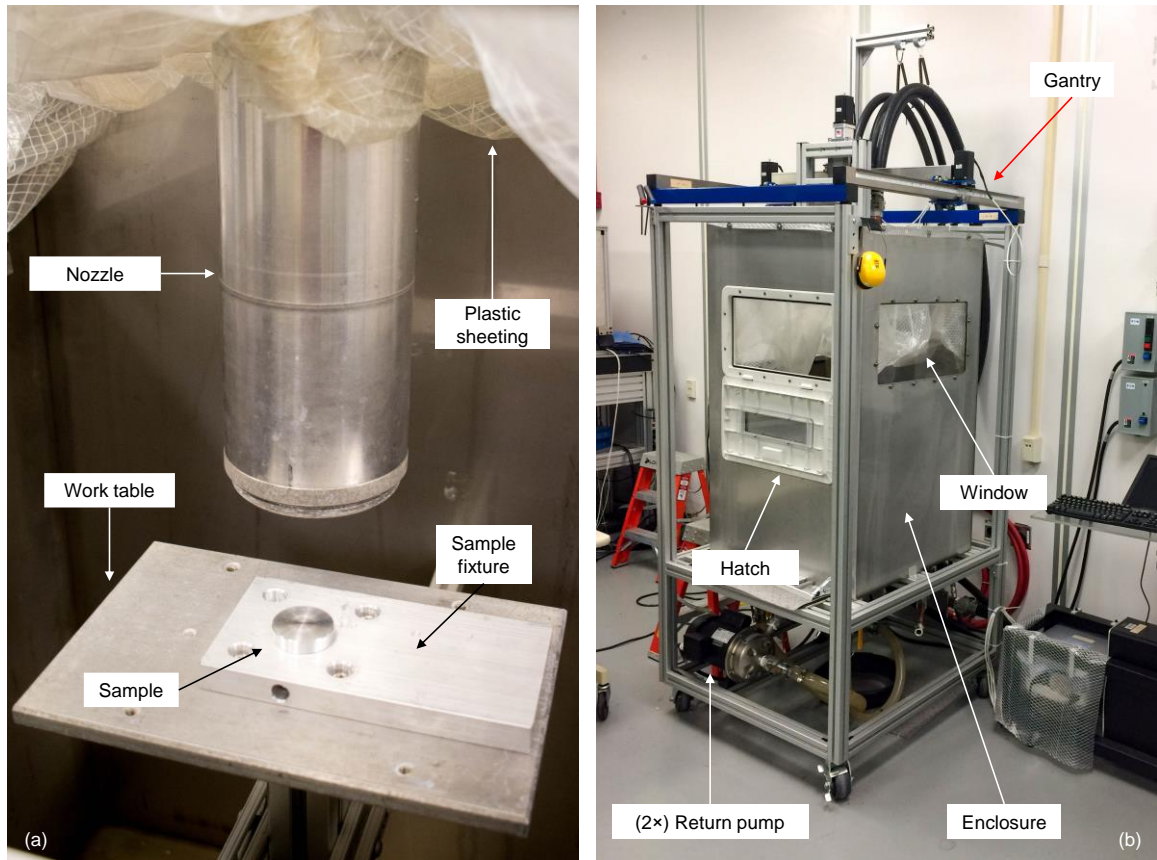
Figure 3-6 (a) Work area inside the WCP enclosure and (b) overview of the WCP test section.

The return lines are equipped with two Ebara CDU70/3-1½HP centrifugal pumps (Figure 3-7) installed underneath the test enclosure. A dual-pump solution was chosen over a single pump given the limited suction head available in the test enclosure. The combined flow rate of the two pumps matches the flow rate entering the test pit from the power unit, balancing the capabilities of the two sections. Butterfly valves and a rotameter (King Flowmeters 7200 series) are installed on the return lines, to regulate and adjust the flow.
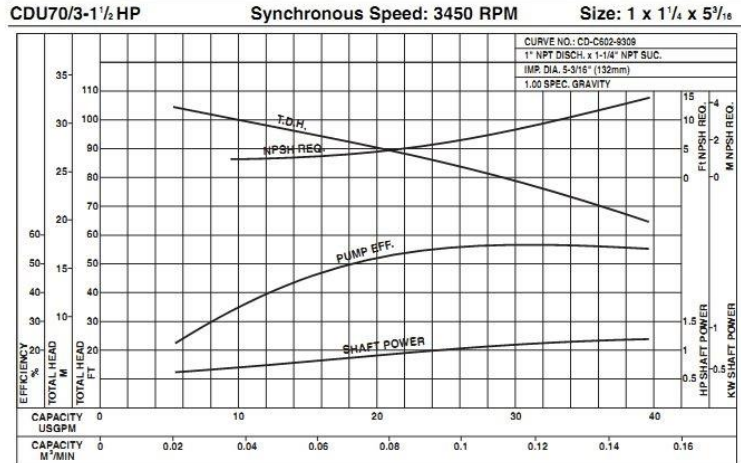
Figure 3-7 Centrifugal pump curve for the EBARA CDU70/3-1½HP adopted in the power unit. (Source: http://www.pumpsebara.com/)

The peening process requires the sample to be scanned in its entirety, demanding the motion of either the nozzle or the workpiece to be automated. Among the available solutions, a Precision Plasma SLC2x2 gantry system was chosen and installed above the test pit. The choice of automating the nozzle path was preferred over XYZ motorized linear stages given the extremely wet environment present inside the enclosure during normal peening operations. The gantry total work area measures 600x600x100 mm³, with four high-torque stepper motors connected through rack-and-pinion systems translating the nozzle in the XYZ directions. A Mach3 CNC controller and standard G-Code are used for nozzle path programming.

3.4.2   WCP Nozzle

This section details the design of the WCP nozzle developed in this research, which is shown in Figure 3-8.

Figure 3-8 WCP nozzle.

3.4.2.1 WCP Nozzle Requirements

The identification of suitable jet velocities is a critical step in the fabrication of the WCP system, as every component described in the previous section had to be sized according to these requirements. In the case of co-flow WCP where two distinct flows are used to generate cavitation, the literature was surveyed to identify the nozzle geometry and flow rates necessary to meet the jet velocity requirements.

Nozzle geometry and inner flow velocity are the key factors when selecting the proper pumping unit and sizing the different components in the circuit. The few studies that have investigated WCP implemented in the co-flow configuration generally employ orifice diameters $D_1 \sim 1$ mm and inner jet pressures $P_{in} \sim 20$ MPa. These values allowed for a rough estimate of the inner jet velocity of $V_{in} \sim 130$ m/s. In order to expand knowledge

of the co-flow WCP process, the target diameter and inner jet velocity selected for this process are $D_1 = 0.9$ mm and $V_{in} = 150$ m/s, respectively.

The orifice shape also plays an important role in the performance of cavitating jets, and the geometry selected for this study can be seen in Figure 3-9a. While a number of studies were published over the years addressing nozzle design for cutting applications [22, 107, 109, 110], there is limited work on enhancing cavitation intensity in peening applications [85, 120, 121]. One important distinction between the different operations was reported in a study by Soyama et al. [111], where it was shown how highly coherent cavitating jets generated by conical nozzles (Figure 3-9b) are very effective for cutting operations, while cylindrical nozzles and their diverging jets are generally better suited for peening.
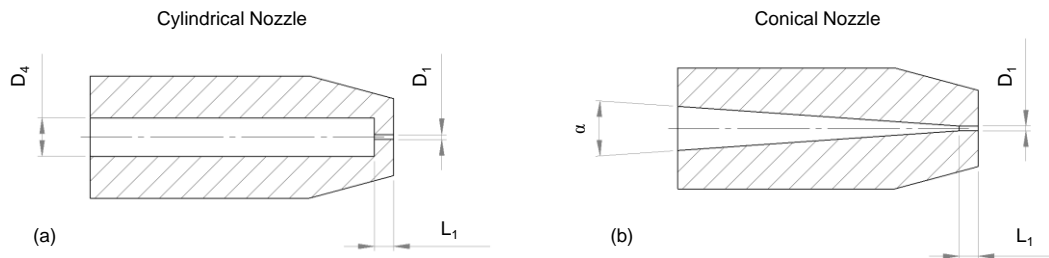
Figure 3-9 WCP orifice geometry.

The sharp (90°) constriction ($D_4 \rightarrow D_1$, Figure 3-9a) characterizing the cylindrical nozzle introduces pressure losses quantified by a discharge coefficient C_d, according to the equation:

$$C_d = \frac{Q_{real}}{Q_{theoretical}} \tag{1}$$

40

where Q_{real} is the actual flow rate downstream from the constriction and $Q_{theoretical}$ is the theoretical flow rate as calculated from the Bernoulli equation. The discharge coefficient for a cylindrical nozzle has been quantified to be $C_d \sim$ 0.55-0.65, as reported by Soyama et al. [85] and by Vijay et al. [110]. This parameter is extremely important when calculating the flow rate in the high pressure line, and has to be accounted for when selecting the pumping unit for the inner flow.

The lack of information of the outer flow rate required to produce cavitation made the sizing of the low pressure line particularly challenging. Few studies [101, 141] report the optimum outer flow pressure P_{out} for co-flow configuration, which cannot be used to accurately calculate the outer flow velocity in the absence of a detailed description of the nozzle geometry. The Bernoulli equation was used to obtain a rough estimate of the range of outer flow velocity ($V_{out} \sim$ 11-14 m/s), and these values were used as a basis for the selection of the outer flow pump and associated components. The nozzle diameters were set to $D_2 \sim$ 25 mm, $D_0 \sim$ 12 mm (Figure 3-12) and the target outer flow velocity was set to $V_{out} =$ 15 m/s.

3.4.2.2   WCP Co-Flow Nozzle

The WCP nozzle shown in Figure 3-10 was designed and fabricated at the Precision Machining Research Center (PMRC) at Georgia Tech. The nozzle is composed of two distinct sections, one for each of the two flows generating cavitation. The overall length of the nozzle (350 mm) was determined experimentally by means of accelerated erosion tests, as described in the next chapter, with the goal of providing sufficient length to allow the flow to homogenize. The external diameter (150 mm) was set based on the commercial

41

availability of thin-walled aluminum pipe stock and the capability of the ME machine shop at Georgia Tech.
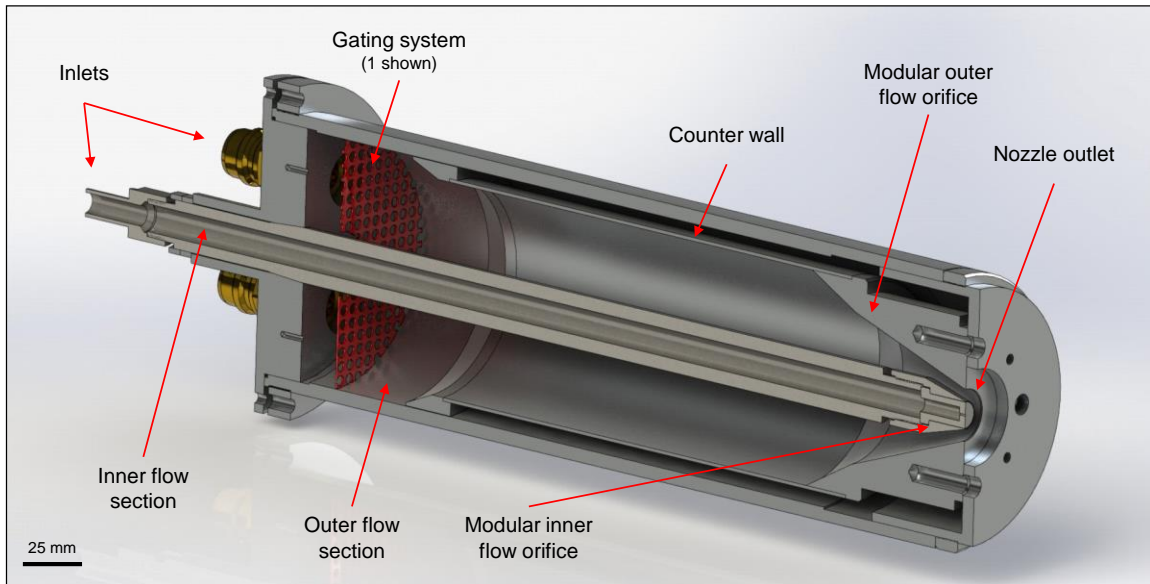
Figure 3-10 WCP nozzle cross-section.
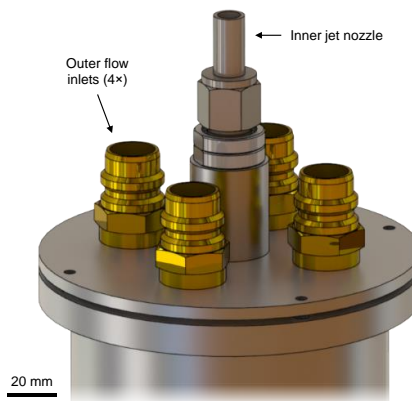
Figure 3-11 WCP nozzle inlet.

The purpose of the outer flow section is to homogenize and straighten the outer flow entering the nozzle from four independent inlets spaced 90° apart (Figure 3-11). The

number of inlets was chosen to maximize the total inlet area, thereby minimizing the inlet flow velocity. A gating system was employed to progressively break down large eddies entering the nozzle, thereby homogenizing and straightening the flow at the nozzle outlet. Details of the gating system are discussed in the next section. The modular design of the outer flow orifice serves three distinct purposes:

1. Interchangeability, for the investigation of different nozzle geometries.
2. Longitudinal adjustability, for the investigation of the effect of the orifice's offset.
3. Radial adjustability, for the coaxial alignment of the two orifices.

The effect of nozzle misalignment on the flow is rather severe and will be discussed in the following section. Finally, a thin walled pipe was connected to the orifice with the purpose of presenting a smooth and consistent transition to the flow in proximity of the nozzle outlet (counter wall).

The inner flow section is composed of a 350 mm long stainless steel tube coupled to the outer section by means of a conical profile and a jam-nut. The other extreme of the tube hosts an interchangeable orifice and it is fixed to the tube by means of a custom made nut. The tube was sized to withstand pressures up to 34 MPa while reducing the flow velocity in the straight section (V_{max} ~ 0.8 m/s), allowing the flow to straighten and homogenize.

43
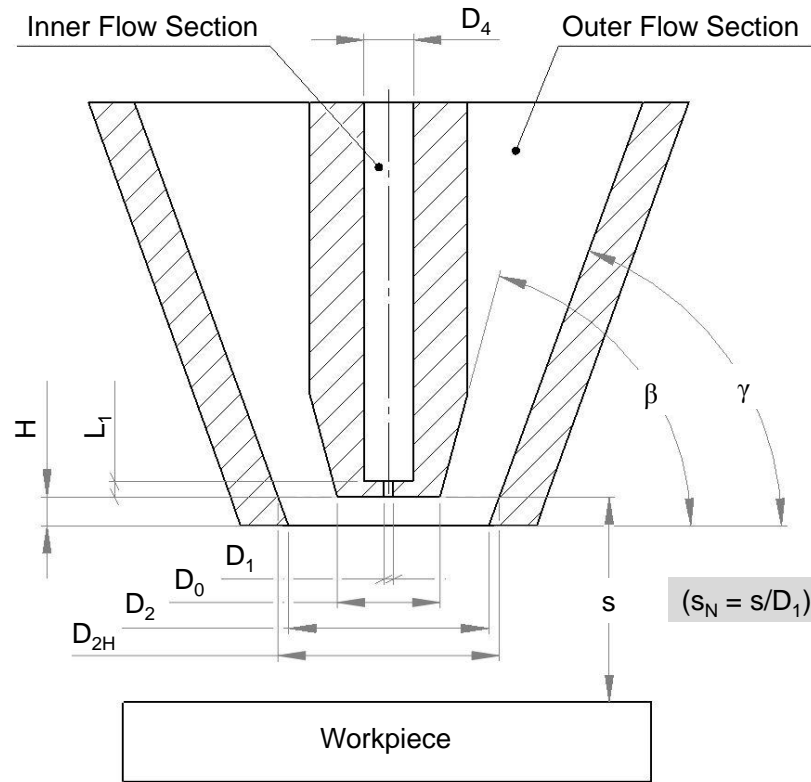
Figure 3-12 WCP outlet geometry.

Figure 3-12 shows the detailed geometry and dimensions of the outlet area of the standard WCP nozzle. Diameter D_1 was produced by electro-discharge machining (EDM) to ensure consistent geometry and surface roughness with the several parts machined for this study. Dimensions D_4 and L_1 were selected based on established knowledge in the field of water-jetting technology [142]. It is important to note that one of the most desirable features in water-jetting is for the jet to be coherent in order to increase penetration. This is not necessarily the case in WCP, but nevertheless, given the complete lack of information on nozzle optimization for cavitation peening processes, it represents a reasonable starting point to build upon. The dimensions of the WCP nozzle outlet section are summarized in Table 3-1.

الاستشارات

www.manaraa.com

Table 3-1 WCP nozzle standard dimensions.

Feature	Dimension	Ratio ($/D_1$)
D_1	0.85 mm	1
D_0	12.8 mm	15
D_2	24.0 mm	28.2
D_{2H}	24.0	28.2
D_4	6.80 mm	8
L_1	2.98 mm	3.5
H	0	0
β, γ	75°, 70°	-

3.4.2.3 Flow Homogenization and Nozzle Alignment

The outer flow entering the nozzle through four ¾ NPT fittings is characterized by flow rates as high as 0.32 m^3/min (85 gpm), corresponding to a maximum localized velocity at the inlets of $V_{inlet} \sim 5$ m/s. In order to obtain consistent flow during the WCP process, the outer flow has to be homogenized, i.e., made axisymmetric, before exiting the nozzle and mixing with the inner flow. Moreover, since vortices inside the nozzle are expected to promote cavitation [143], it was deemed desirable to work with a straight flow in this research, so that the effect of swirl on the cavitation intensity produced in the co-flow configuration can be meaningfully investigated in future work. Figure 3-13 (a) shows the

45

effect of insufficient outer flow homogenization (lobing) during an accelerated erosion test performed to assess the cavitation intensity of the flow.
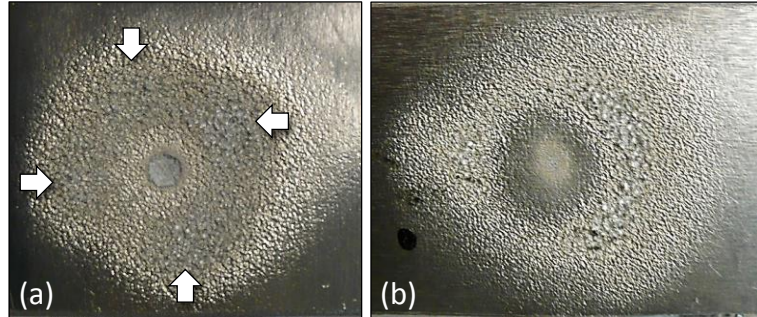
Figure 3-13 (a) Lobing in cavitation craters as a consequence of insufficient outer flow homogenization and (b) effect of orifice misalignment in water cavitating jets.

Flow homogenization was accomplished through a series of perforated sheets and meshes placed in the proximity of the nozzle inlets. The perforated sheets used (Figure 3-14 (a)) were decreasing in size and spacing, as shown in Figure 3-14 (b). The number of perforated sheets can be selected to match the nozzle requirements, and a minimum number of three is recommended. It is important to remember that perforated sheets and meshes introduce considerable pressure losses in the nozzle, which must be accounted for when selecting the pumping unit.

46
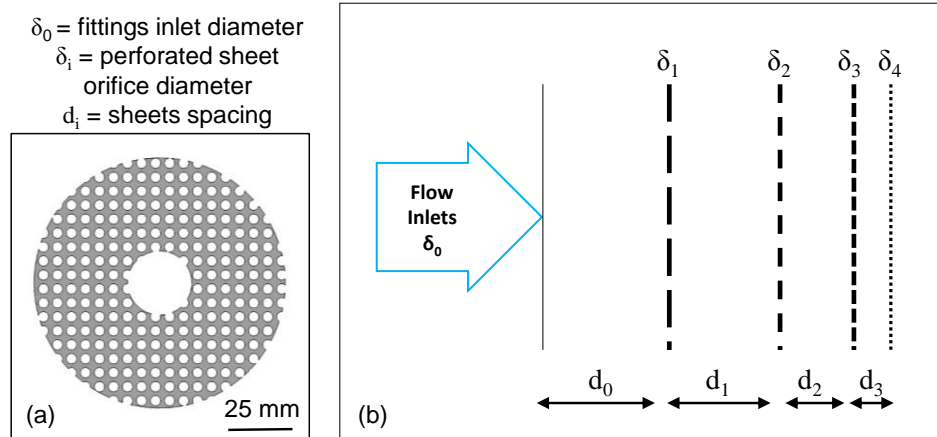
Figure 3-14 (a) Perforated sheet used in the WCP nozzle and (b) system sizing and spacing.

Flow straightening, if necessary, can be achieved by means of a honeycomb section suitably placed between the gating system and the nozzle outlet.
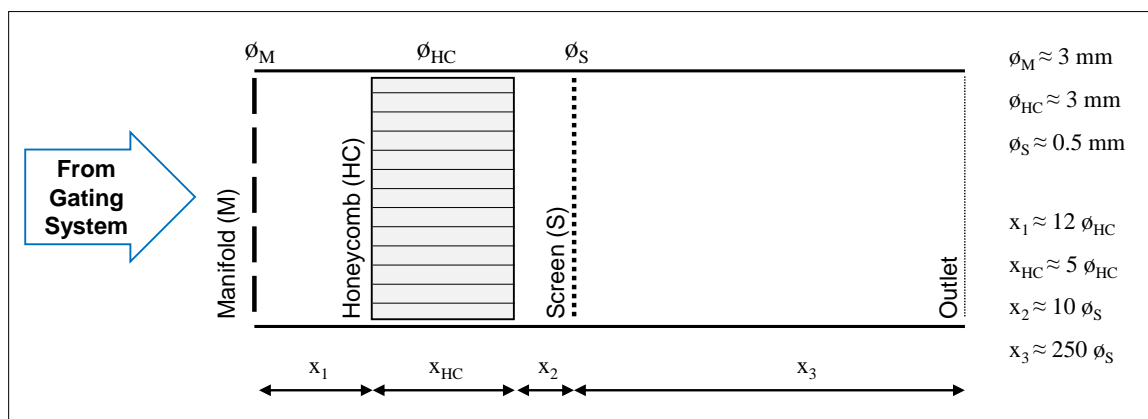
Figure 3-15 Flow straightening system. Cell sizes are indicated by ϕ.

A manifold (gate) and a fine mesh screen are generally placed on each side of the honeycomb. Figure 3-15 specifies the cell dimensions as well as the distances between the major components in the system. Once again it must be mentioned that a honeycomb structure dramatically increases the pressure losses in the pipe section, and therefore must be accounted for in the design phase. Preliminary accelerated erosion tests suggested that the nozzle developed in this study and described in the previous section does not require a

47

honeycomb section downstream from the gating system, and therefore it was not included in the final design.
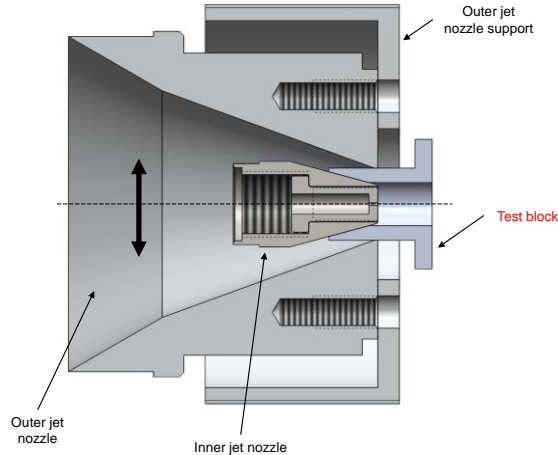
Figure 3-16 Test block used for accurate nozzle alignment.

Finally, nozzle alignment was found to be a critical factor in the performance of the WCP nozzle, as seen in Figure 3-13 (b), prompting the adoption of a design solution that permitted fine adjustments. A test block (Figure 3-16) was machined to precisely match the outer flow diameter and the conical profile of the inner flow nozzle, and used in the assembly of the nozzle to maintain the coaxiality between diameters D_1 and D_2 within the safe value of $\pm$ 0.1 mm.

3.5   Summary

In this chapter, details of the design and fabrication of a unique Water Cavitation Peening (WCP) system were presented. The challenges encountered during the design phase, along with the engineering solutions adopted to address them, were discussed in the chapter in detail. The following chapter will discuss the characterization of the co-flow

cavitating flow as a function of the jet velocities and the nozzle standoff distance for the

introduction of beneficial residual stresses in Al 7075-T6.

CHAPTER 4.   FLOW CHARACTERIZATION IN CO-FLOW WATER CAVITATION PEENING

4.1 Overview

Water cavitation jet peening (WCP) uses cavitation caused by the shear layer created by two concentric co-flowing jets with a large velocity difference to introduce compressive residual stresses in the surface layers of metal components subjected to fatigue loading or to a corrosive environment. Mass loss and surface alteration in WCP have been shown to be minimal compared to other mechanical surface enhancement techniques, such as shot peening (SP). This chapter investigates the effect of concentric jet velocities in a co-flow cavitation jet peening process on the cavitation intensity and peening performance, which are characterized by accelerated erosion on Al1100-O and Al 7075-T6 samples and by a strip curvature test on Al 7075-T6 samples. Accelerated erosion tests reveal that cavitation intensity and associated erosion (measured by mass loss) are greatly affected by the combination of the inner (V_{in}) and outer (V_{out}) jet velocities and the normalized standoff distance (s_n). Two distinct operating regimes characterized by different erosion patterns are found depending on the relative magnitudes of the jet velocities: one that is focused at the jet center (termed the *center regime*) and another that is concentrated in the surrounding annular region (termed the *ring regime*). Erosion tests on Al1100-O and Al 7075-T6 give different results in terms of the maximum mass loss as a function of the jet velocities and standoff distance. When compared to strip curvature tests, it is found that the accelerated

50

erosion tests on Al 1100-O do not capture the influence of inner jet velocity V_{in} and instead imply misleading trends with regard to the outer flow velocity V_{out}. Erosion and curvature tests performed on Al 7075-T6 are found to be in good agreement and therefore are believed to be better suited to identify the optimum process conditions for WCP. Notwithstanding the higher mass loss density values observed in the center regime, the resultant strip curvature is found to be higher in the ring regime for a higher inner jet velocity V_{in}, potentially leading to larger and deeper compressive residual stresses.

4.2   Experimental Method

4.2.1   Accelerated Erosion Tests

Cavitation aggressiveness is evaluated indirectly by exposing samples of soft aluminum Al1100-O and Al7075-T6 to the cavitating flow for an extended period of time (beyond the incubation period [143]) and measuring the corresponding mass loss. It should be noted that mass loss is an undesirable effect in peening processes. However, it serves to quantitatively establish the flow conditions that yield the most intense cavitation. Once cavitation aggressiveness is established through the accelerated erosion tests, actual peening is performed by exposing the surface to the cavitating jet for a short duration (*saturation time* [15]) to induce residual stresses without any mass loss. This method was initially developed and adopted by many researchers in the field of cavitation to evaluate the cavitation erosion resistance of engineering materials [21, 116, 129, 131], and adopted by Soyama et al. [15, 18, 85, 86, 97, 101] to identify the optimum peening conditions. The underlying assumption of this method is that the erosion tests conducted on soft materials, such as Al 1100-O, are suitable for identifying the flow conditions that optimize the

51

peening process on different structural aerospace materials such as aluminum and titanium alloys. In order to validate this assumption erosion tests on both Aluminum 1100-O and 7075-T6 are carried out in this chapter and the results are compared to strip curvature tests performed on Al7075-T6 Almen strips.

Table 4-1 Test conditions.

V_{in}	110	130	150			(m/s)
V_{out}	5.0	6.5	8.0	9.5	11.0	(m/s)
	12.5	14.0	15.5	17.0		
$s_n = s/D_1$	35	40	45	50		(-)

In the erosion tests the samples are exposed to cavitation for up to 30 min [97, 116] at normalized standoff distances s_n in the range 35 – 50. The inner jet flow velocities V_{in} used in the experiments are 110, 130 and 150 m/s. These values were selected based on the study of Hattori et al. [122], where it was shown that cavitation erosion prevails over erosion caused by direct liquid impingement when the jet velocity is in the range of 100-140 m/s for a submerged cavitation configuration. The outer flow velocities V_{out} chosen for this study range from 5 m/s to 17 m/s and are spaced 1.5 m/s apart. This velocity range is partially based on [18], where only outer flow pressures are reported, allowing for a rough estimation of the outer jet velocity range. The experimental parameters are summarized in

Table 4-1. Water temperature was maintained at $21\pm3°C$ with the help of a water chiller. Mass loss was measured using an analytical balance with 0.1 mg resolution and 0.3 mg repeatability. Average flow velocities are calculated at the nozzle exit as follows:

$$v = \frac{Q}{A_o} \tag{2}$$

where Q is the volumetric flow rate measured by an inline turbine flow meter (with 1% accuracy) and A_o is the orifice cross-sectional area measured by an optical comparator with accuracy of $5\text{x}10^{-3}$ mm. Figure 4-1 (left) shows an example of the crater generated by an accelerated erosion test. Two distinct features can be identified: the outer erosion ring and the center erosion crater. Similar to [116], the *mass loss density* is calculated for each flow condition:

$$M_D = \frac{m}{A_C} \tag{3}$$

where m is the mass loss of the sample (mg) and A_C is the crater surface area (cm^2). The total crater surface area is evaluated by grey scale analysis of the optical images of the eroded samples exposed to the cavitating flow for 3 min, as shown in the example in Figure 4-1 (right). To ensure consistency, the images are taken under the same lighting conditions and the greyscale threshold is kept approximately constant for all the samples.
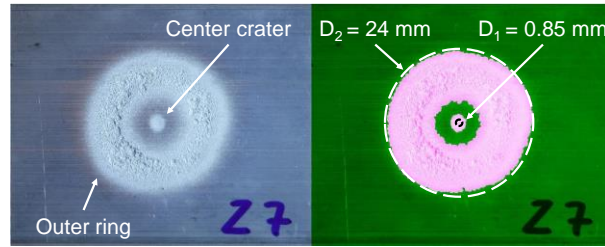
Figure 4-1 Eroded area in an accelerated erosion test (left) and eroded surface area from greyscale image analysis (right). Nozzle diameters D_1 and D_2 are overlaid for reference.

4.2.2 *Strip Curvature Tests*

Compressive residual stresses in the metal surface are a desired outcome of the peening process. Their evaluation is generally done by techniques such as X-ray diffraction (XRD) and hole-drilling, which are expensive and time consuming. In contrast, strip curvature tests have been extensively used in industry as a fast method to evaluate the peening performance [23, 24]. The strip curvature caused by the plastic deformation induced by the peening process is used as an indirect measure of the change in compressive residual stresses produced in the metal surface. Strip curvature tests are performed on 7075-T6 aluminum Almen strips of Type Y. The strip dimensions are 76x19x3.9 mm^3, and have Brinell hardness in the range of 143-158 BHN. The initial roughness of the strips is equal to 0.514 µm (R_a) with a standard deviation of 0.102 µm. The strips are mounted in a fixture as shown in Figure 4-2.

54
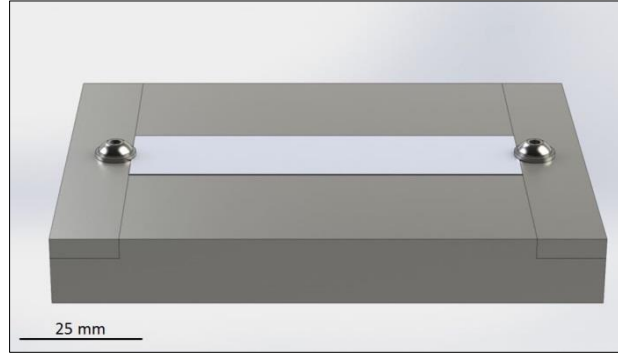
Figure 4-2 Almen strip fixture.

The scanning speed (of peening) is set to 480 mm/min for $V_{out} > 8.0$ m/s and 240 mm/min for $V_{out} < 8.0$ m/s, and the scanning pitch is held constant at 1 mm for all flow conditions. The processing time t_P is defined as the time required to peen the entire sample, and for a given strip geometry it is a function of the scanning speed and pitch. To ensure homogeneous treatment of the strip, peening is performed by following the scan path shown in Figure 4-3, where the trajectory followed by the cavitation nozzle starts and finishes outside the sample boundaries. The radius of curvature r is measured by an optical comparator after each complete coverage of the sample (*full pass*). The curvature is averaged over three measurements based upon a minimum of five interpolation points. Each strip undergoes several full passes and the experiment is terminated when the incremental variation in curvature ρ ($\rho=r^{-1}$) drops below the 5% threshold, indicating that the saturation time t_s has been reached.
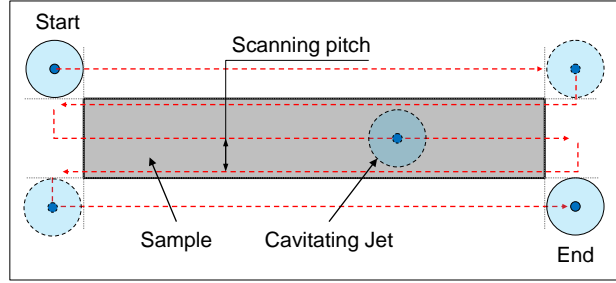
Figure 4-3 Peening path.

The exposure time t_e is defined as the time duration the material is exposed to the cavitating flow per unit area. An estimate of the exposure time is necessary for the assessment of the saturation time. It is a function of the scanning parameters (pitch, scanning speed) and the cavitating jet area (A_C), which depends on the combination of the jet velocities and standoff distance. The procedure used to determine the exposure time is described in the next section.

4.2.2.1 Evaluation of the Cavitating Flow Exposure Time

The exposure time per unit area in the water cavitation peening process is evaluated by the following steps:

1. Evaluate the crater equivalent diameter D_e:

$$D_e = \sqrt{\frac{4A_c}{\pi}} \tag{4}$$

where A_c is the crater area measured with the image processing algorithm.

2. Sum all the equally spaced chords a_j shown in Figure 4-4 using the following equations:

56

$$h_1 = 0$$
$$h_j = h_{j-1} + p$$
$$a_j = 2\sqrt{(h_j + (j-1)p)(D_e - h_j + (j-1)p)} \qquad (5)$$
$$L_0 = \sum_1^n a_j$$

where a_j is the jth-chord length, h_j is the distance of the jth-chord from the top of the circle, p is the scanning pitch and L_0 is the sum of all the n cords. Since the distance h_1 between the chord a_1 and the top of the circle can fall anywhere between 0 and p, it is initially assumed to be equal to h_1=0, and the uncertainty introduced in L_0 by this assumption is eventually evaluated:

$$n = \left\lfloor \frac{D_e}{p} \right\rfloor \qquad (6)$$

3. Vary h_1 between 0 and p at $p/10$ intervals, compute L_i for each interval and average to obtain $L_{ave.}$

4. Divide L_{ave} by the scanning speed for peening to obtain the exposure time t_e.

The error caused by the introduction of the equivalent diameter D_e in place of the dimensions of the annulus has been estimated to be no greater than 0.2 %, while the uncertainty caused by the variability of h_1 between 0 and p is two orders of magnitude smaller than t_e.
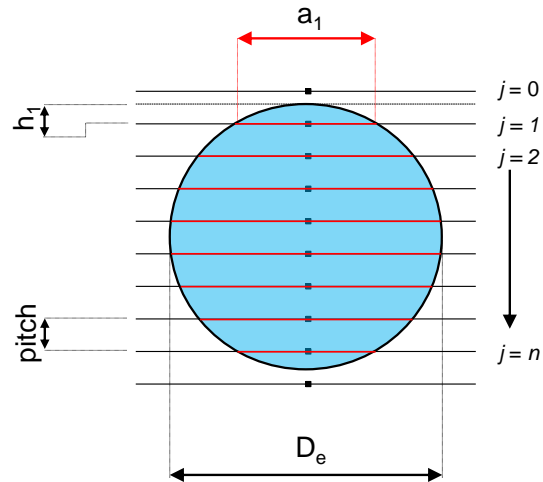
Figure 4-4 Exposure time estimation from the sum of chords length travelled by the nozzle.

4.2.3   *High Speed Imaging and Analysis*

The cavitating flow was imaged used a high speed CMOS camera (Phantom v7.3). The camera was equipped with a fixed focal length Nikon 35 mm f2.0 prime lens, which captured images in 8-bit greyscale with an image size of 512 x 256 pixels. A schematic of the imaging procedure is shown in Figure 4-5.
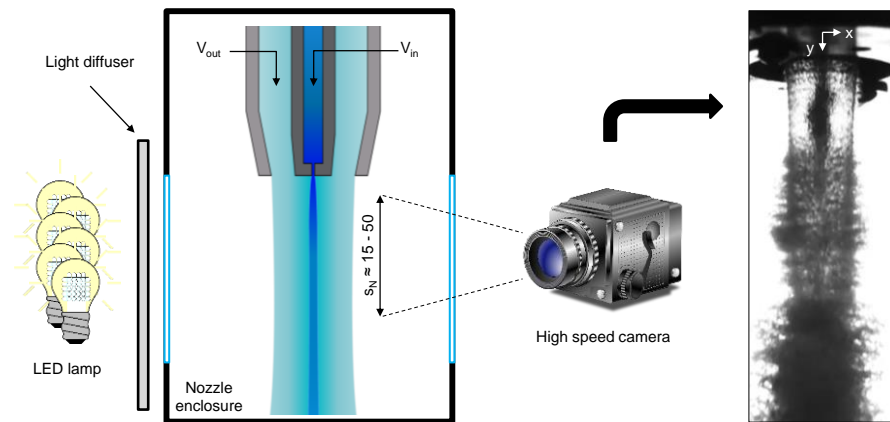
Figure 4-5 High speed imaging procedure.

58

For each flow condition, 2000 frames at 14000 fps were captured for a total duration of 0.143 s. During imaging, a consistent lighting condition and a consistent relative distance between the camera and nozzle were maintained. A diffuser was placed between the light source and the nozzle to homogenize the background illumination. A multi-step image analysis was conducted on the cavitation cloud with the goal of isolating it and identifying the characteristic features of the cloud such the average cloud size and the cloud frequency. First, each frame was cropped to the region of interest, which measured $0.75 \text{x} D_2$ along the x-axis and $15 \leq s_N \leq 50$ along the y-axis. The analysis was limited to this section since the cavitation cloud at $s_N > 45$ was very diffuse and tended to merge with the wavy pattern characterizing the outer flow, thus rendering it indistinguishable from the outer jet (Figure 4-5). The frames were subsequently transformed into a binary image by setting an appropriate black/white (b/w) threshold, and an averaging filter was applied to remove the isolated pixels. Morphological noise removal was performed by erosion and dilation operations via a circular structuring element using MATLAB image processing toolbox. Finally, the cavitation cloud was isolated and any remaining noise extending from the sides of the frame was removed. An example of the image processing procedure just described is shown in Figure 4-6.

A Lagrangian frame of reference was adopted in the analysis of the cavitation cloud, and for each cloud the maximum cloud width as a function of time at the optimum standoff distance ($s_N = 40 - 45$) was determined. The maximum cloud width is used as a metric to quantify the changes in the cloud characteristics as a function of the experimental variables.
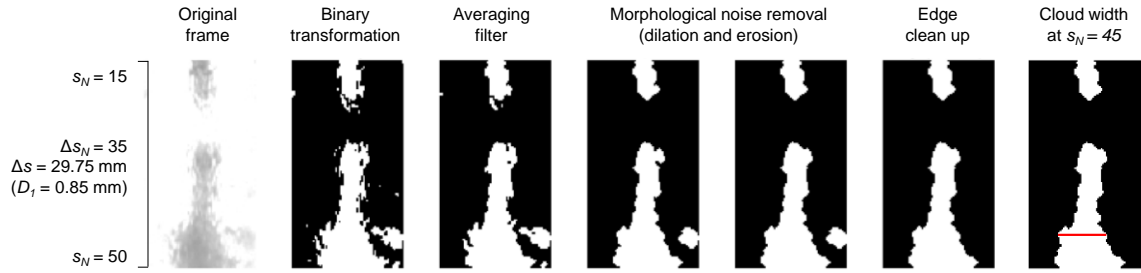
Figure 4-6 Representative image processing analysis of the cavitation cloud.

Given the periodic nature of the cavitation cloud, spectral analysis was performed on the cloud width for different flow conditions. The cloud width dataset was initially filtered by a bandpass Butterworth filter (100-6500 Hz) to remove static peaks and high frequency noise. The power spectral density (PSD) was calculated and averaged among five subsets consisting of 400 frames each. Changes in the PSD with flow conditions are analyzed and discussed later in the chapter.

4.3   Results and Discussion

4.3.1   *Accelerated Erosion Tests (Al 1100-O and Al 7075-T6)*

The results of the accelerated erosion tests on aluminum Al1100-O and Al7075-T6 samples are discussed in this section. The outer jet velocity V_{out} was varied between 5.0 and 17.0 m/s at 1.5 m/s intervals, while the normalized standoff distance s_n was varied between 30 and 50. Two exposure times t_e were chosen for Al1100-O, namely 3 and 10 min, while the exposure time of 30 min was used for Al7075-T6. Results for the three inner jet velocities V_{in} and $t_e = 3$ min are shown in Figure 4-7 to Figure 4-9, where lines connecting data points are added to facilitate the understanding of the trends.

60

Figure 4-7 Mass loss as a function of the outer flow V_{out} velocity for different normalized stand-off distances s_n (V_{in} = 110 m/s, Al 1100-O, t_e = 3 min).

Figure 4-8 Mass loss as a function of the outer flow V_{out} velocity for different normalized stand-off distances s_n (V_{in} = 130 m/s, Al 1100-O, t_e = 3 min).

61

Figure 4-9 Mass loss as a function of the outer flow V_{out} velocity for different normalized stand-off distances s_n (V_{in} = 150 m/s, Al 1100-O, t_e = 3 min).
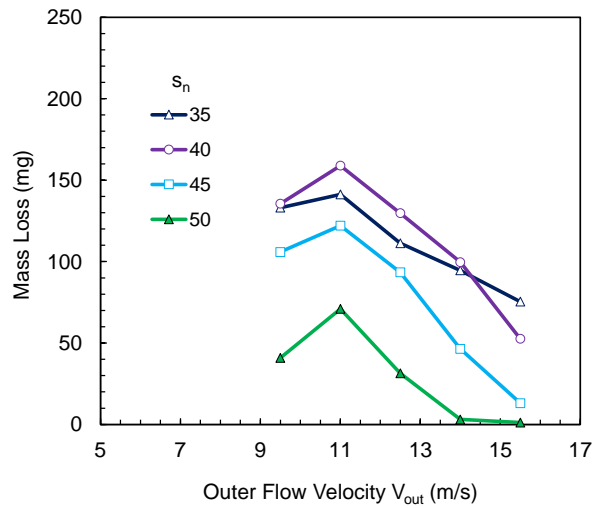
Figure 4-10 Mass loss as a function of the outer flow V_{out} velocity for different normalized stand-off distances s_n (V_{in} = 110 m/s, Al 1100-O, t_e = 10 min).

The mass loss trends for V_{in} =110 m/s can be seen in Figure 4-7. Cavitation aggressiveness is found to be maximum at V_{out} =11.0 m/s for a standoff distance between 35 and 40. Figure 4-8 shows the mass loss trends for V_{in} =130 m/s. Two distinct local

62

maxima can be seen in this plot; the first is observed at V_{out} =11.0 m/s and s_n=45, and the second occurs at V_{out} =15.5 m/s and s_n=40. While the mass loss peak at V_{out} =11.0 m/s is consistent with the results of Soyama [97], the presence of a second peak appears to be a new result. Figure 4-9 shows the mass loss trends for V_{in} =150 m/s. As observed in the previous cases, a peak is noted at V_{out} =11.0 m/s and s_n=45, while the trends for s_n = 35 and 40 suggest that local maxima occur at V_{out} >17.0 m/s, similar to that seen in Figure 4-8. For all velocity combinations investigated, the maximum mass loss was found to occur at a standoff distance in the range 35<s_n<45, consistent with data reported by Soyama et al. [97] and Vijay et al. [22].

Figure 4-11 Mass loss as a function of the outer flow V_{out} velocity for different normalized stand-off distances s_n. (V_{in} = 130 m/s, Al 1100-O, t_e = 10 min).

63

Figure 4-12 Mass loss as a function of the outer flow V_{out} velocity for different normalized stand-off distances s_n. (V_{in} = 150 m/s, Al 1100-O, t_e = 10 min).

Interestingly, the maximum mass loss for each inner jet velocity V_{in} was found to be in the range 33.3±1.6 mg, concealing the influence of the inner jet velocity on the cavitation response of the material. To investigate this phenomenon, the experiments were repeated for a subset of flow conditions at an extended exposure time of 10 min Results are reported in Figure 4-10 to Figure 4-12 for the three inner jet velocities V_{in}. It can be seen that while trends are substantially unchanged for the V_{in} =110 m/s and 130 m/s, the V_{in} =150 m/s case shows a shift in the optimum s_n from 45 to 50, as seen in Figure 4-12. Mass loss is also found to be maximum at V_{out} = 15.5 m/s for cases with high inner jet velocity V_{in} and short standoff distances s_n. As the standoff distance is increased, the mass loss peaks shift toward lower outer jet velocities V_{out} (Figure 4-11 and Figure 4-12). To the best of the authors' knowledge, this trend has never been reported before; a hypothesis explaining these observations is presented at the end of this section.
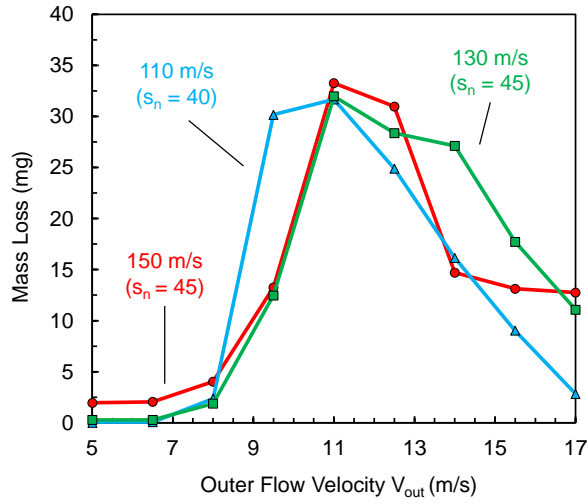
Figure 4-13 Mass loss as a function of the outer flow velocity V_{out} for different inner flow velocities V_{in} at the respective optimum normalized stand-off distances s_n (Al 1100-O, t_e = 3 min).

Figure 4-14 Mass loss as a function of the outer flow velocity V_{out} for different inner flow velocities V_{in} at the respective optimum normalized stand-off distances s_n (Al 1100-O, t_e = 10 min).

65
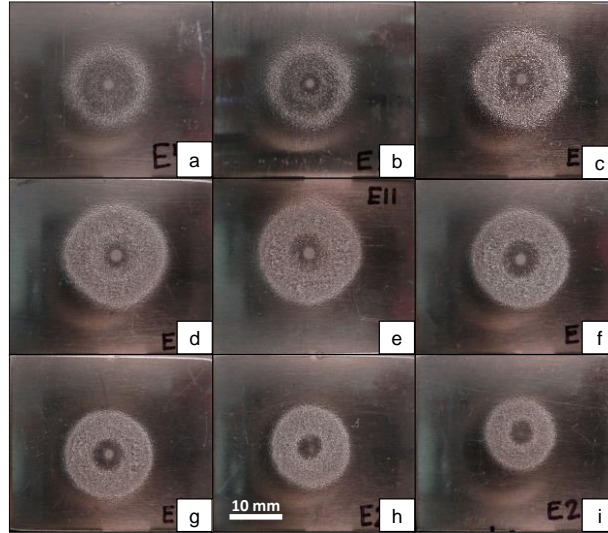
Figure 4-15 Erosion patterns on Al1100-O for WCP with V_{in} = 150 m/s, s_n = 45 and V_{out} = (a) 5.0 m/s, (b) 6.5 m/s, (c) 8.0 m/s, (d) 9.5 m/s, (e) 11.0 m/s, (f) 12.5 m/s, (g) 14.0 m/s, (h) 15.5 m/s, (i) 17.0 m/s.

A comparison of the results obtained at exposure times t_e of 3 and 10 min is given in Figure 4-13 and Figure 4-14. The plots report the mass loss as a function of the outer flow velocity for different inner jet velocities at a standoff distance that yields the optimum (maximum) cavitation erosion. The maximum mass loss is consistently achieved at the outer jet velocity V_{out} = 11 m/s, this being the value that optimizes two competing mechanisms occurring in the jet outside the nozzle, namely, cavitation production, which increases with the difference between V_{in} and V_{out}, and cavitation delivery to the workpiece surface, which increases with the outer flow velocity V_{out}, as explained by Soyama [18]. The maximum mass loss is also found to consistently occur at a standoff distance of $40<s_n<45$ in all cases considered. An explanation for this observation is offered by Summers in [142], where it is reported that the ratio L_1/D_1 and the slope of the straight section (L_1) are the parameters that are mainly responsible for determining the jet penetration outside the orifice. Since neither of these two parameters are varied in this

66

work, it is not surprising to find the optimum standoff distance s_n to be relatively unchanged throughout the study. The effect of inner jet velocity on cavitation erosion, partially concealed at t_e =3 min, is now evident at longer exposure times (Figure 4-14). It can be seen that the flow combination of V_{in} = 130 m/s, V_{out} = 11 m/s, s_n = 45 yields the most aggressive cavitation erosion (and therefore highest cavitation aggressiveness) results for Al 1100-O.

Figure 4-15 shows the erosion patterns for V_{in} =150 m/s and s_n=45 at different outer flow velocities V_{out}. Similar to Soyama's findings [97], the pattern exhibits a small central crater and an annular eroded region. The dimensions of the two features are found to vary with the flow velocity. The surface area of the center crater is maximum for outer jet velocities V_{out} < 8 m/s (see Figure 4-15(a)-(b)) and it decreases as the outer jet velocity increases, disappearing completely at V_{out} =17 m/s.

Evidence suggests that the center crater is caused by the cavitation generated directly around the inner jet. Figure 4-16 shows the mass loss trends for flow velocities of V_{in} =150 m/s and V_{out} ≤ 6.5 m/s. For V_{out} < 8 m/s, the ring erosion is negligible compared to the center crater and the mass loss can be attributed exclusively to the center crater. Cavitation aggressiveness is found to decrease with increasing s_n as the momentum of the inner jet dissipates further away from the nozzle orifice. The cavitation aggressiveness is also found to increase at lower outer jet velocity V_{out}, as a larger velocity difference (between V_{in} and V_{out}) creates the conditions for more cavitation to be generated. Similar patterns for the center erosion can be found in the work of Vijay et al [110].
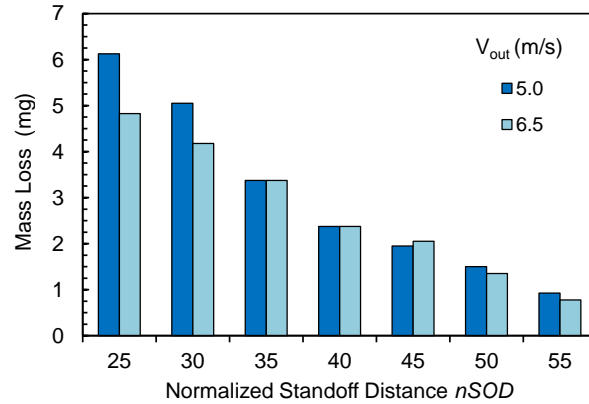
Figure 4-16 Mass loss in center regime as a function of outer flow velocity V_{out} and standoff distance s_n. (V_{in} =150 m/s, t_{e} = 3 min).
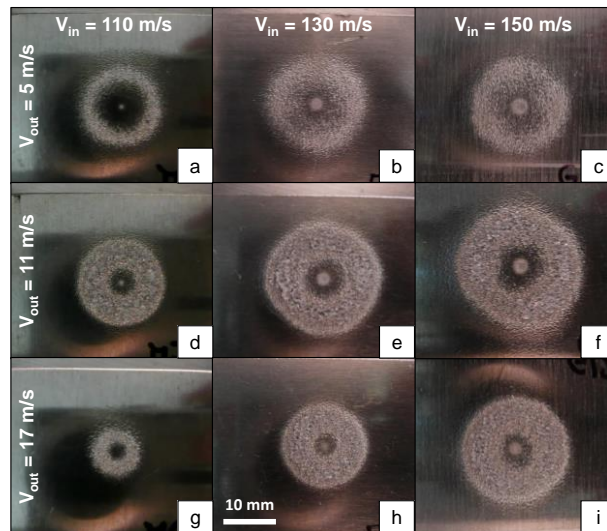
Figure 4-17 Erosion patterns for $s_n = 45$ ($t_e = 3$ min).

The turbulence in the mixing layer between the two jets generates the cavitation cloud responsible for the erosion. The bubbles in the cloud spread radially upon impinging the metal surface, collapsing in the annular-shaped pattern observed in Figure 4-15 and Figure 4-17. This erosion pattern is typical of cavitating water jets for both submerged and co-flow configurations, as discussed by Soyama [18, 86, 101] and Hattori [122]. Figure

68

4-17 shows the erosion crater for s_n=45 as a function of V_{in} and selected outer velocities V_{out}, while Figure 4-18 shows the associated crater area trends. It can be seen that, for a given velocity V_{out}, both the center crater and ring crater area increase with V_{in}. When the inner jet velocity V_{in} is kept constant, the area of the ring-shaped region peaks at V_{out} ~11 m/s, while the center crater size tends to decrease monotonically as the outer jet velocity V_{out} is increased from 5 to 17 m/s. Figure 4-19 shows the crater area as a function of the standoff distance s_n. It can be seen that the crater area is maximum for 9.5< V_{out} <12.5 and 40<s_n<45, which is consistent with the mass loss results, but their effect on the crater area is arguably less clear when compared to the effect of flow velocities seen in Figure 4-18.
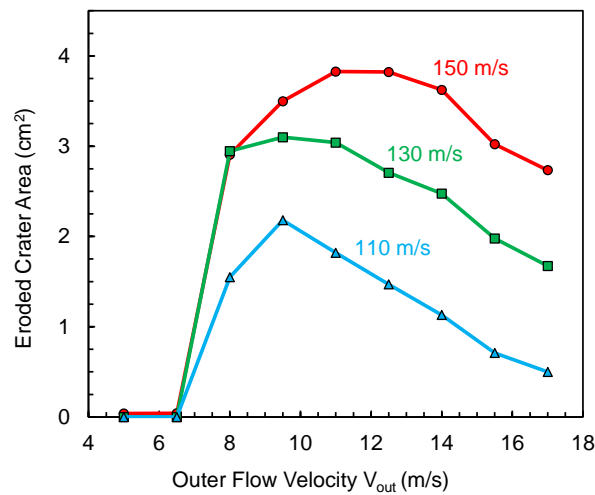
Figure 4-18 Crater area as a function of the outer flow velocity V_{out} for different inner jet velocities V_{in} ($s_n = 45$).
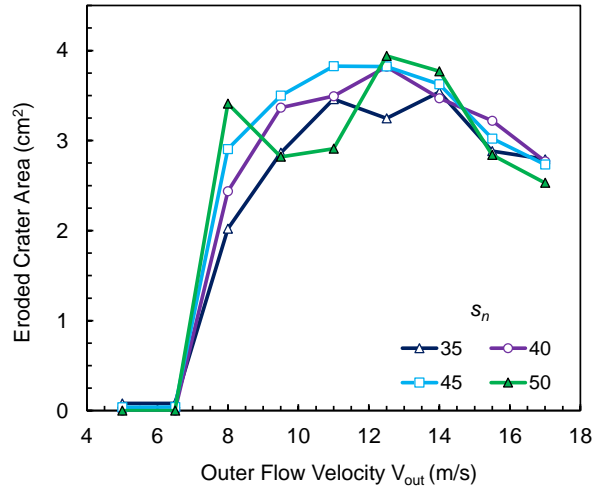
Figure 4-19 Crater area as a function of the outer flow velocity *Vout* for different standoff distances *sₙ* (V_{in} =150 m/s, t_e = 3 min).

These observations suggest that for a given velocity combination, the standoff distance significantly affects the cavitation phenomena responsible for mass loss, while the treated surface area is only marginally affected.

Given the variability observed in the mass loss and crater area, the mass loss per unit area, or *mass loss density,* is introduced to better characterize the flow aggressiveness, analogous to the approach proposed by Choi et al [116].
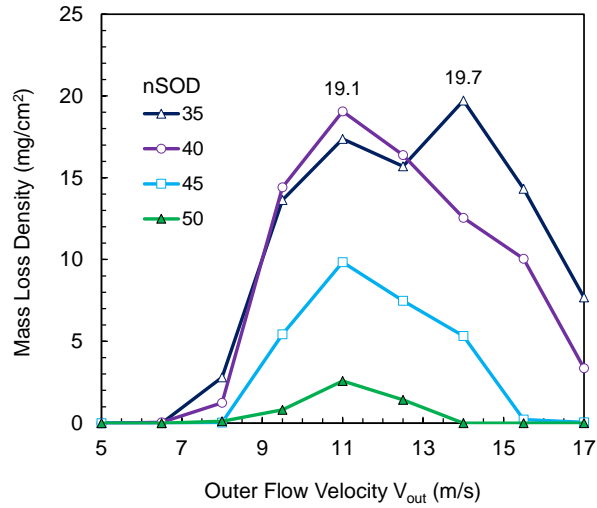
Figure 4-20 Mass loss density as a function of the outer flow velocity V_{out} for different normalized stand-off distances s_n. (V_{in} = 110 m/s, Al 1100-O, t_e = 3 min).
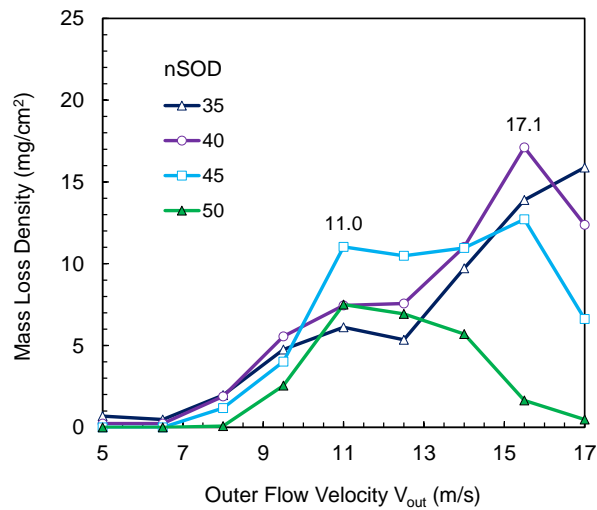
Figure 4-21 Mass loss density as a function of the outer flow velocity V_{out} for different normalized stand-off distances s_n. (V_{in} = 130 m/s, Al 1100-O, t_e = 3 min).

The mass loss density M_D is computed for all the flow conditions reported in Table 4-1 for an exposure time t_e of 3 min and the results are shown in Figure 4-20 to Figure 4-22. While the trends for V_{in} =110 m/s (Figure 4-20) are found to closely follow those observed for the

mass loss results shown in Figure 4-7, the mass loss density for V_{in} =130 m/s reveals a shift

toward V_{out} =15.5 m/s for the maximum values reported in Figure 4-8. Finally, for V_{in} =150

m/s (Figure 4-22), the trends are substantially different from those observed in the mass

loss plots, and two distinct regimes of operation, namely *center regime* and *ring regime*,

appear to exist.
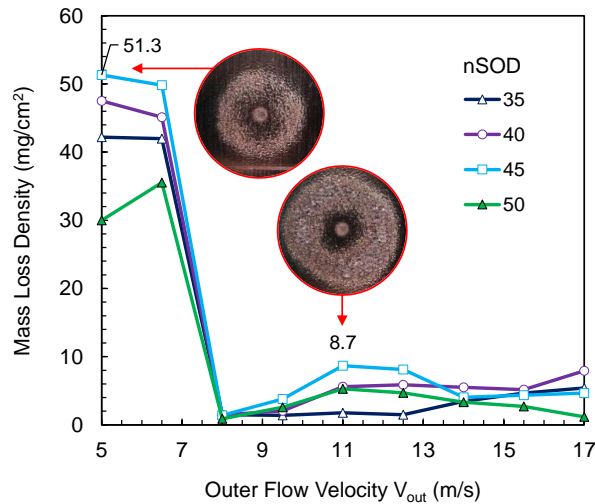
Figure 4-22 Mass loss density as a function of the outer flow velocity V_{out} for different normalized stand-off distances s_n. (V_{in} = 150 m/s, Al 1100-O, t_e = 3 min, Crater images to scale).

The center regime (Figure 4-15a) is characterized by low mass loss (<10 mg), focused in

the center crater with minor pitting in the ring region. Its onset occurs at a high inner jet

velocity (V_{in}=150 m/s) and low outer jet velocity (V_{out} <8.0 m/s), with mass loss density

increasing for high values of V_{in}. Mass loss in the ring region for the center regime

conditions is observed only for exposure times $t_e \gtrsim 5$ min Figure 4-23 shows the evolution

of mass loss for V_{in}=150 m/s and s_n = 45, where a sudden increase in mass loss is recorded

with the onset of ring erosion at t_e = 5 min This observation motivated the choice of t_e = 3

min for the quantification and evaluation of cavitation aggressiveness in terms of mass loss density for different flow conditions.
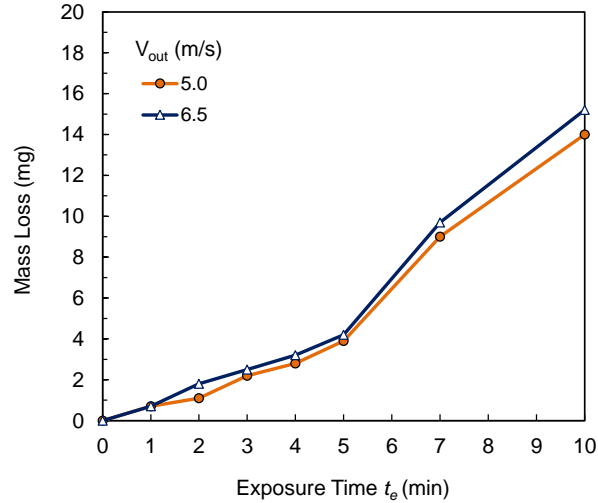
Figure 4-23 Evolution of mass loss for V_{in} =150 m/s, s_n = 45 and different outer flow velocities V_{out} (Center regime conditions).

The ring regime (Figure 4-15e) displays high mass loss values (up to ~35 mg) distributed in the ring area. It occurs at all inner jet velocities V_{in} and outer flow velocities $V_{out} > 8.0$ m/s. Similar to the mass loss trends, it displays a peak at the outer flow velocity of V_{out} =11.0 m/s for all V_{in} and at V_{out} =14.0 m/s for V_{in} = 110 and 130 m/s. Most notably, the maximum mass loss density is recorded in the center regime for V_{in} =150 m/s, while the mass loss density in the ring regime displays a local maximum at V_{out} =11.0 m/s but decreases for increasing V_{in}. It is important to notice that, while ring and center craters were previously observed by other authors in both submerged [98, 110] and co-flow configurations [97, 101], this is the first study to systematically describe the phenomenon, and to identify the flow conditions that determine the onset of the two distinct behaviors.
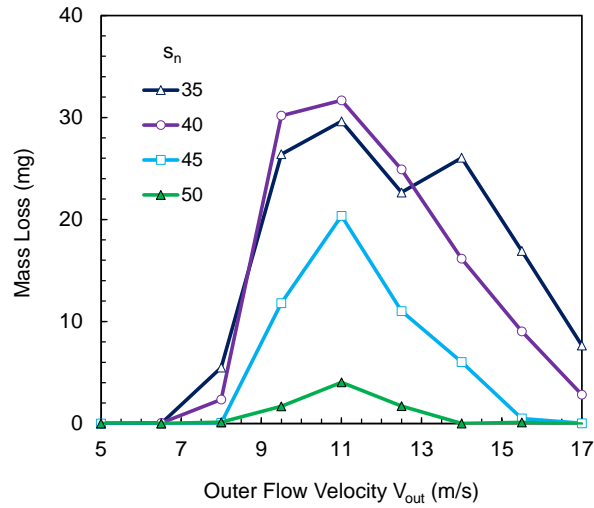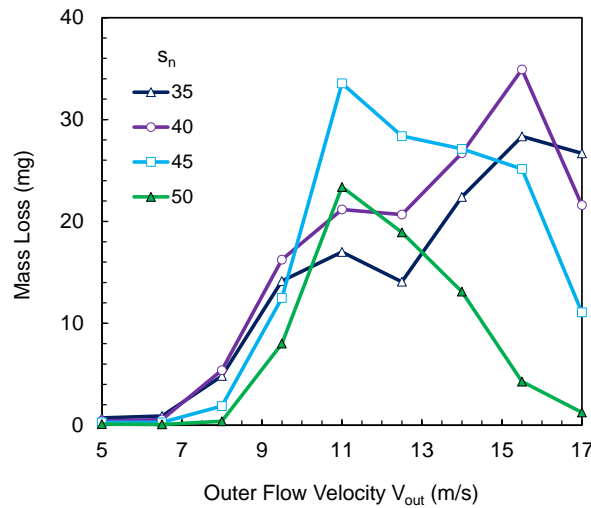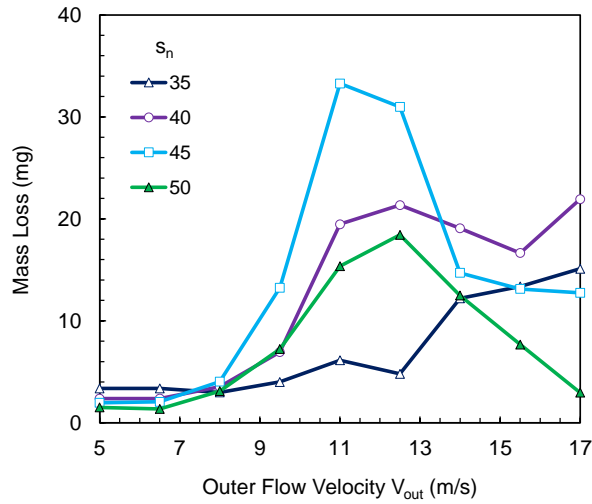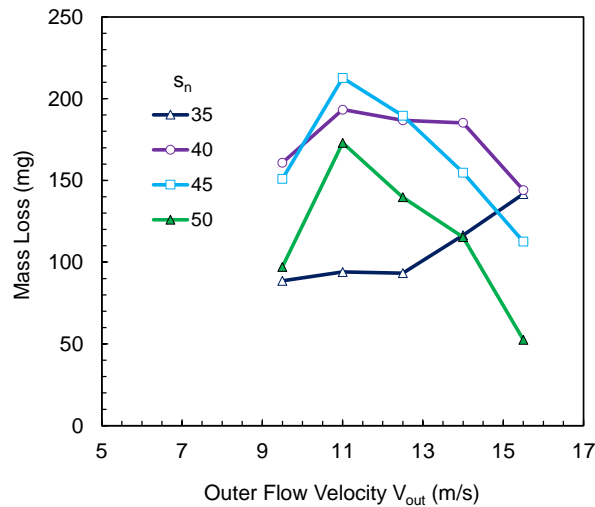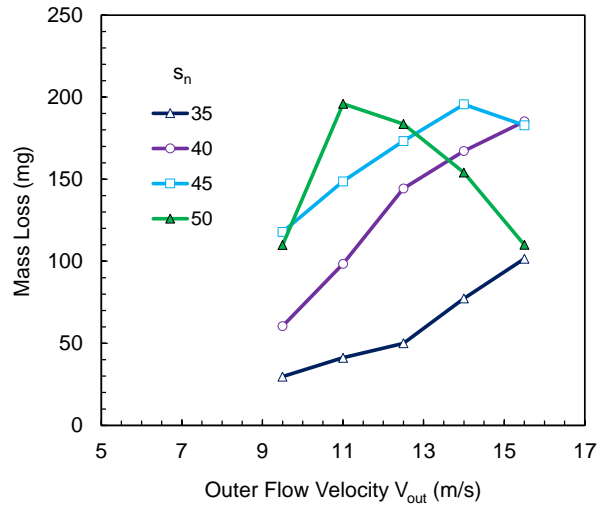
73
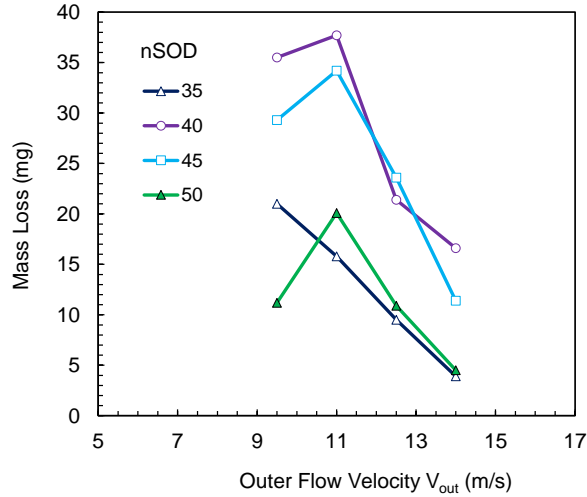
Figure 4-24 Mass loss as a function of the outer flow velocity V_{out} for different normalized stand-off distances s_n. (V_{in} = 150 m/s, Al 7075-T6, t_e = 30 min).

Finally, tests were performed on Al 7075-T6 in order to validate the assumption that cavitation erosion results are suitable for the identification of optimum peening parameters in co-flow based cavitation peening. The choice of flow parameters for these tests is based on the results obtained for Al 1100-O. Experiments for V_{in} of 110 and 130 m/s were performed at a standoff distance of s_n of 40 and 45, respectively, while preliminary tests were performed for the inner jet velocity V_{in} = 150 m/s given the variability of optimum standoff distance s_n observed at different exposure times t_e for Al 1100-O (see Figure 4-9 and Figure 4-12). Figure 4-24 shows the effect of outer flow velocity and standoff distance on the mass loss for Al 7075-T6 at V_{in} = 150 m/s. Mass loss peaks are once again observed at V_{out} = 11 m/s with standoff distance s_n = 40. No local maxima are registered at $V_{out} \geq$ 14 m/s as previously seen for Al 1100-O. This difference in results is believed to be caused by the substantial difference in strength exhibited by the two materials. As reported by several authors [17, 97, 116, 137, 139], the cavitation cloud

responsible for erosion is composed of a multitude of single impacts displaying a wide range of sizes and impact forces. In the case of soft Al 1100-O, since the cavitation cloud population contains a sufficiently large fraction of bubbles that exhibit a sufficiently large impact pressure capable of plastically deforming the material, the flow condition (high flow rate) that maximizes the number of impacts is likely to increase the amount of material eroded by cavitation. On the contrary, for high strength alloys such as Al 7075-T6, the flow condition that increases the production of high pressure impacts (i.e. for higher velocity difference) is most likely to be effective in eroding the material.
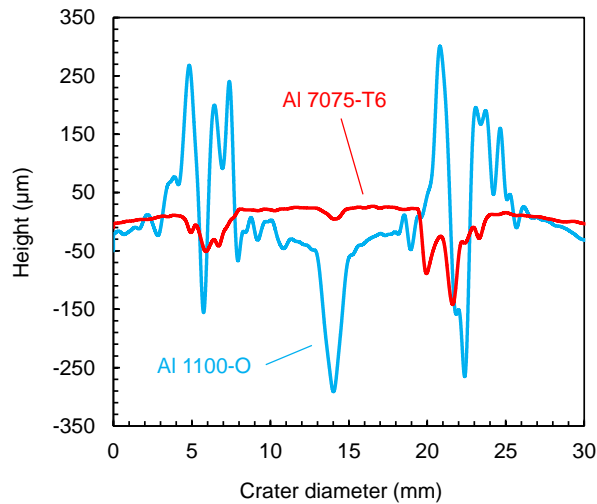
Figure 4-25 Crater profiles for Al 1100-O (t_e = 3 min, 33 mg total mass loss) and Al 7075-T6 (t_e = 30 min, 34 mg total mass loss). Other conditions: V_{in} = 150 m/s, V_{out} = 11 m/s, s_n = 45.

The different crater morphologies exhibited by the two materials is also a consequence of the differences in material behavior. Shockwaves and micro-jets easily deform soft aluminum 1100-O upon impact, generating large pits surrounded by plastically deformed material protruding from the surface produced in the early stages of cavitation erosion. These protrusions are weakly attached to the surface and can easily be removed by the

75

flow, generating a new surface to be eroded. On the other hand, aluminum 7075-T6 exhibits significantly smaller and shallower pits, resulting in an overall smoother surface as seen in Figure 4-25. Figure 4-26 summarizes the outcomes of the mass loss tests for Al 7075-T6 as a function of the inner and outer flow velocities at the chosen standoff distance. Remarkably, cavitation erosion is found to be proportional to the inner jet velocity V_{in}, with the highest mass loss recorded at V_{in} = 150 m/s and V_{out} = 11 m/s. The effect of outer flow velocity V_{out} is found to be consistent with the results shown in Figure 4-13 and Figure 4-14 for Al 1100-O.
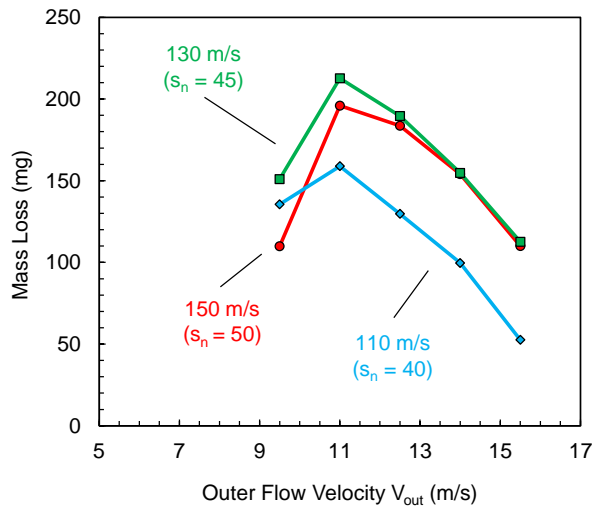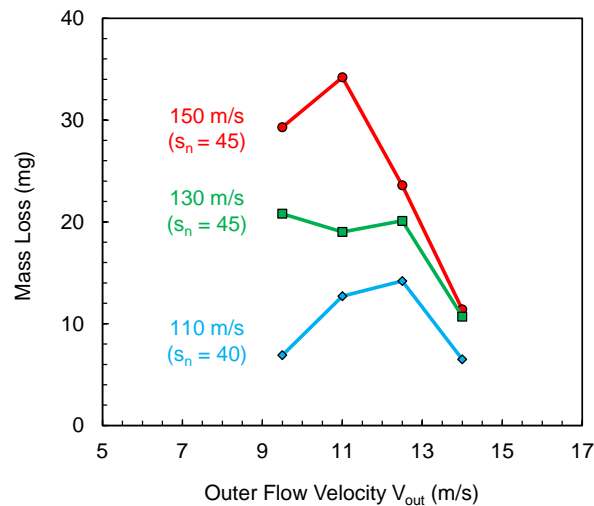

Figure 4-26 Mass loss as a function of the outer flow velocity V_{out} for different inner flow velocities V_{in} at the respective optimum normalized stand-off distances s_n. (Al 7075-T6, t_e = 30 min).

Strip curvature test results are analyzed next to confirm the observed cavitation aggressiveness trends.

4.3.2 Strip Curvature Results (Al 7075-T6)

76

The experimental parameters selected for the strip curvature experiments (peening tests) are summarized in that maximizes the flow aggressiveness is adopted for each velocity combination.

Table 4-2 Flow velocities (m/s) selected for strip curvature tests and the relative normalized standoff distance (s_n).

V_{in} (m/s)	Center Regime V_{out} (m/s)		Ring Regime V_{out} (m/s)						
	5.0	6.5	8.0	9.5	11.0	12.5	14.0	15.5	17.0
110	x	x	x	(40)	(40)	(40)	(40)	x	x
130	x	x	x	(40)	(45)	(45)	(45)	(40)	x
150	(25; 45)	x	x	(45)	(45)	(45)	(45)	x	x
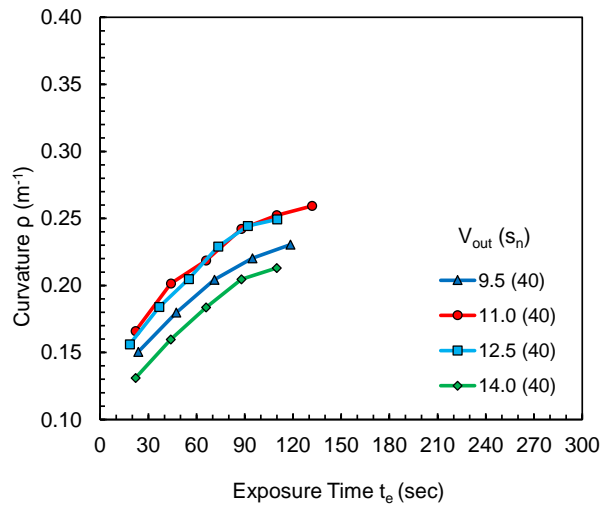
Figure 4-27 Strip curvature as a function of exposure time for V_{in} = 110 m/s and different outer flow velocities V_{out}.

77
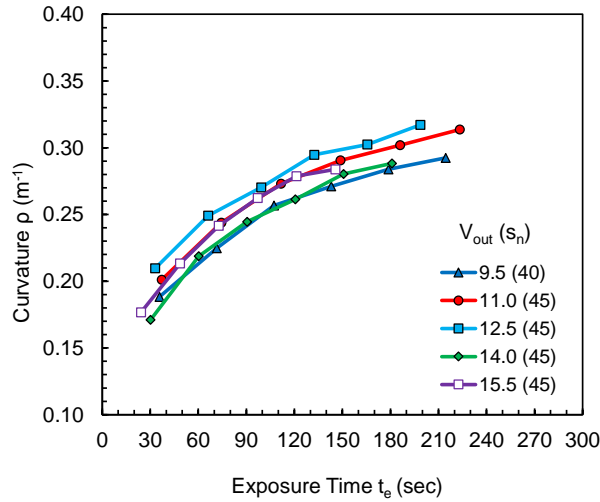
Figure 4-28 Strip curvature as a function of exposure time for V_{in} = 130 m/s and different outer flow velocities V_{out}.

Figure 4-27 shows the evolution of strip curvature for V_{in} =110 m/s for different outer jet velocities as a function of exposure time. The exposure time per unit area for each condition is computed using the method given in appendix A. It is important to note that the overall processing time is uniform for all the peening tests (t_p = 18 min), as the scanning feed rate and pitch are kept constant in all experiments. The variations observed in the exposure time per unit area are the result of the trends in crater area reported in Figure 4-18 and Figure 4-19. Peening tests confirm the results shown in Figure 4-7 and Figure 4-10; cavitation aggressiveness and strip curvature are maximized at the outer flow velocity of V_{out} =11.0 m/s.

Figure 4-28 shows the evolution of strip curvature for V_{in} =130 m/s as a function of exposure time for different outer jet velocities V_{out}. As seen in the previous case, the strip curvature results capture the maximum obtained from the erosion tests at the outer flow

78

velocity of 11.0< V_{out} <12.5 m/s. Remarkably, the peening tests do not confirm the presence

of a cavitation peak at V_{out} =14.0 m/s seen in Figure 4-8 and Figure 4-11.
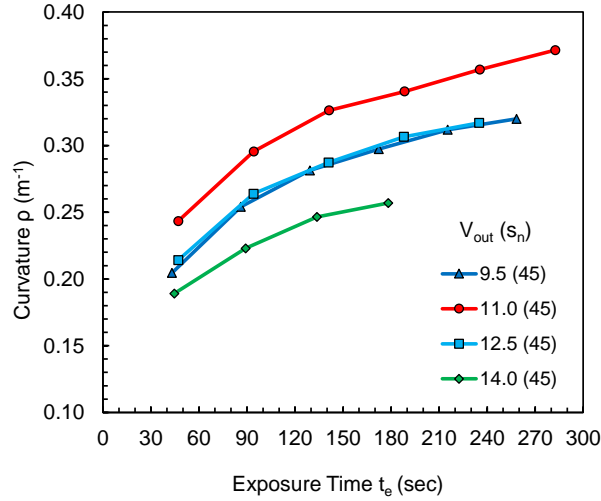
Figure 4-29 Strip curvature as a function of exposure time for V_{in} = 150 m/s and different outer flow velocities V_{out} in ring regime.
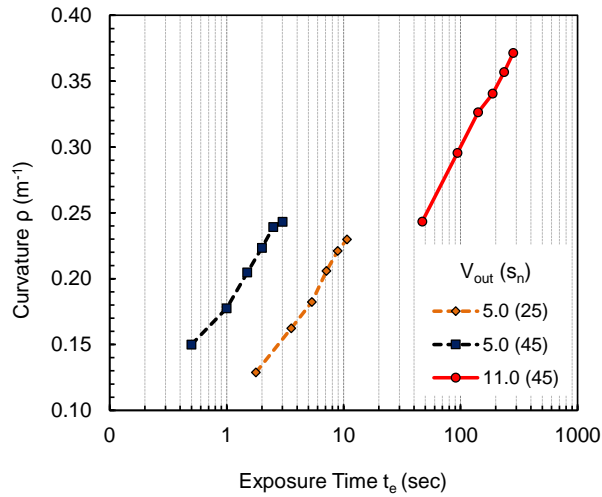
Figure 4-30 Strip curvature as a function of exposure time for V_{in} = 150 m/s and different outer flow velocity *Vout* in center regime.

79

Finally, Figure 4-29 presents the evolution of strip curvature for V_{in} =150 m/s as a function of the exposure time for different outer jet velocities V_{out}. Once again, the strip curvature tests capture the peak obtained in the erosion tests at the outer flow velocity V_{out} =11.0 m/s, confirming the trends seen in Figure 4-9, Figure 4-12 and Figure 4-24. However, the data for the center regime conditions shown in Figure 4-30 (V_{out} =5.0 m/s, s_n = 25 and 45) do not find a correspondence with the erosion test results for Al 1100-O shown in Figure 4-9 and Figure 4-16, with the strip curvature at s_n=45 yielding higher values than at s_n=25. This trend is believed to be caused once again by the substantial difference in mechanical properties exhibited by the two materials, as explained in the previous section.

Moreover, saturated strip curvatures for the center regime conditions are substantially lower than those for the ring regime conditions, contradicting the mass loss density trends shown in Figure 4-22.
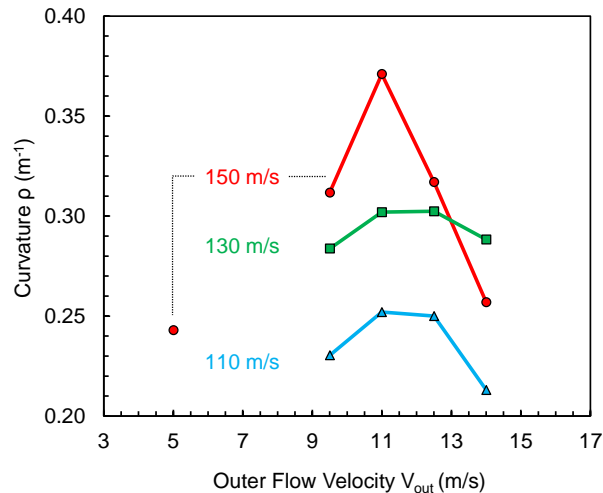
Figure 4-31 Saturated strip curvature as a function of outer jet velocity V_{out} for different inner jet velocities V_{in}.

The saturated strip curvature is plotted in Figure 4-31 as a function of the outer flow velocity V_{out} for different inner jet velocities V_{in}. Note that the strip curvature is assumed to saturate with increased exposure time when subsequent measurements differ by less than 5%. In addition, the saturated strip curvature represents the maximum curvature achievable under the specified flow conditions, and therefore it is independent of peening time. It is evident from the plot that, for each inner jet velocity V_{in}, the strip curvature is maximized in the same outer flow velocity range ($11.0 < V_{out} < 12.5$ m/s) and at the same normalized standoff distance ($40 < s_n < 45$), confirming, in part, the results of the accelerated erosion tests on the same material.

In order to confirm the conclusion regarding standoff distance, its effect on the strip curvature for $V_{in} = 150$ m/s and $V_{out} = 11.0$ m/s was also investigated. Results are shown in Figure 4-32 and they confirm the mass loss peak at $s_n=45$ seen in Figure 4-9.
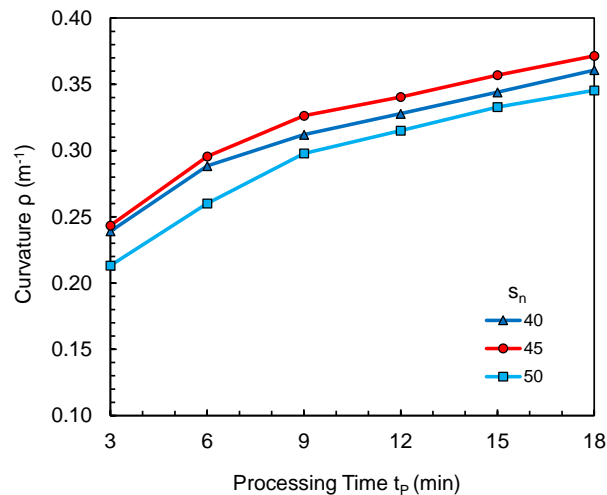
Figure 4-32 Strip curvature as a function of the normalized standoff distance s_n for $V_{in} = 150$ m/s and $V_{out} = 11$ m/s.

Not confirmed by the curvature tests are the peaks observed for Al1100-O at higher outer flow velocities (V_{out} >14.0 m/s) most evident in Figure 4-8, Figure 4-11 and Figure 4-12. Despite the different nozzle and flow velocities, the trends shown in this study also confirm the work of Vijay et al [22, 110].
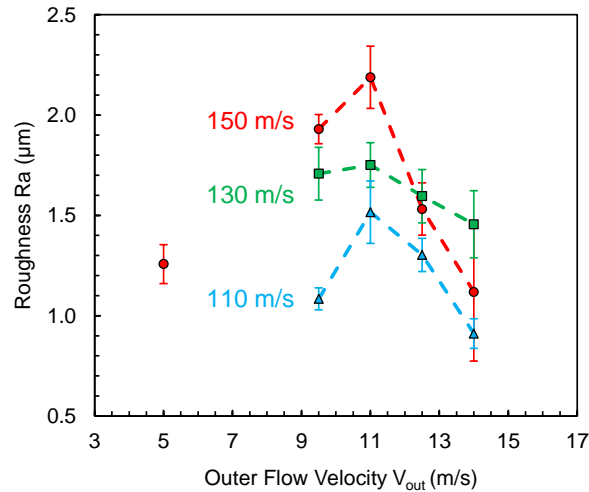
Figure 4-33 Roughness *Ra* as a function of the outer jet velocity *V_{out}* for different inner jet velocities *V_{in}*.

Finally, the strip curvature for a cavitating jet is proportional to the inner jet velocity V_{in}, a conclusion that cannot be drawn from the mass loss trends seen for Al1100-O and is in opposition to the mass loss density results for Al1100-O. Despite the mass loss density being highest in the center regime, the maximum (saturated) strip curvature is observed in the ring regime.

Figure 4-33 shows the surface roughness R_a for the saturated samples shown in Figure 4-31. Roughness values are averaged over 10 measurements for each sample; one standard deviation is included in the plot (initial R_a=0.514 µm). Remarkably, the surface roughness follows the same trend as the saturated strip curvature.

82

4.3.3 Repeatability

Repeatability was investigated for selected cases for both the accelerated erosion and the strip curvature tests. The chosen conditions were those relative to the local maxima observed in Figure 4-13, Figure 4-26 and Figure 4-31 and are summarized in Table 4-3. Five repetitions were performed for the erosion tests on Al 1100-O and Al 7075-T6, while three repetitions were performed on the strip curvature tests. The experiments were randomized to reduce bias from factors not included in the experimental design.

Table 4-3 Flow conditions selected for the repeatability study.

Test type	Material	V_{in} (m/s)	V_{out} (m/s)	s_n (-)	Repetitions
Cavitation erosion	Al 1100-O	130	11	45	5
	Al 1100-O	150	11	45	5
	Al 7075-T6	150	11	45	5
Strip curvature	Al 7075-T6	150	11	45	3

Figure 4-34 shows the repeatability results obtained for the erosion tests on Al 1100-O. All the data points are reported and the average is included as a function of exposure time t_e. There is considerable variability in the results and it is observed to increase with exposure time. This variability is believed to be inherent to the erosion process for the soft Al1100-O and is attributed to crater morphology evolution as described in the previous section. The ranges overlap for exposure times $t_e < 5$ min for the considered cases, preventing indisputable identification of the highest cavitation intensity condition for Al1100-O.

83
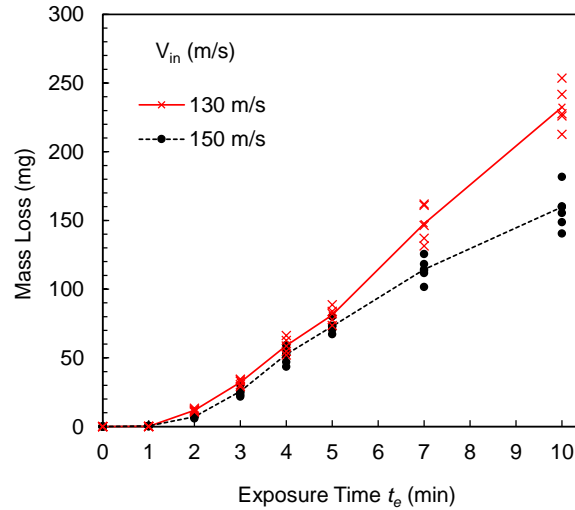
Figure 4-34 Cavitation erosion tests repeatability for Al 1100-O at different inner jet velocity V_{in} and exposure time t_e for V_{out} =11.0 m/s and s_n=45 (5 repetitions).
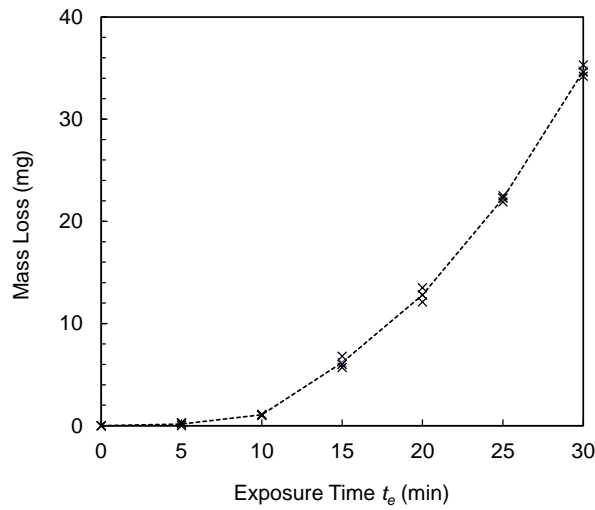
Figure 4-35 Cavitation erosion tests repeatability for Al 7075-T6 with V_{in} =150 m/s, V_{out} =11.0 m/s and s_n=45 (3 repetitions).

Finally, the results for exposure time t_e =10 min confirm the trends anticipated in Figure 4-14, with the inner jet velocity V_{in}=130 m/s yielding the highest mass loss at V_{out} = 11 m/s and s_n=45. Figure 4-35 and Figure 4-36 show the results for the erosion and strip

84

curvature tests on Al 7075-T6 for the flow condition reported in Table 4-3. Different from the results for Al1100-O, high repeatability is observed in both the erosion and curvature tests for Al7075-T6. Finally, variability range is not observed to increase with exposure time.
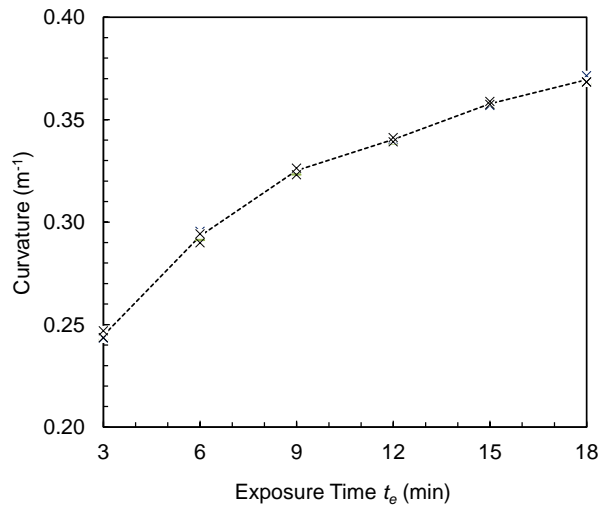
Figure 4-36 Strip curvature repeatability for Al 7075-T6 with V_{in} =150 m/s, V_{out} =11.0 m/s and s_n=45 (3 repetitions).

4.3.4   High Speed Imaging Results

The effect of inner and outer jet velocities was investigated by means of high speed imaging analysis and the results are discussed in this section.

Figure 4-37 offers of a comparison of the cavitating flow as the inner jet velocity V_{in} is increased from 50 m/s to 150 m/s. From the image, two significant features can be observed: the periodic nature of the cavitation cloud and the wavy pattern on the outside boundary of the outer flow. The periodicity of the cavitating clouds in Figure 4-37 has been previously described by Soyama et al. [101, 120, 121, 144] for both the submerged and co-

85

flow WCP configurations. The nozzle geometry and inlet pressures affect the shedding frequency of the cavitating cloud. This is a desirable feature of the flow, as pulsating jets are reported to produce higher cavitation intensity compared to non-pulsating jets [109]. The wavy pattern is the result of cavitation cloud pulsation and has the same characteristic frequencies as the cloud pulsation (0.5 – 2 kHz, Soyama [101]). Figure 4-37 also reveals that the intensity of the wavy pattern increases with inner jet velocity V_{in}.
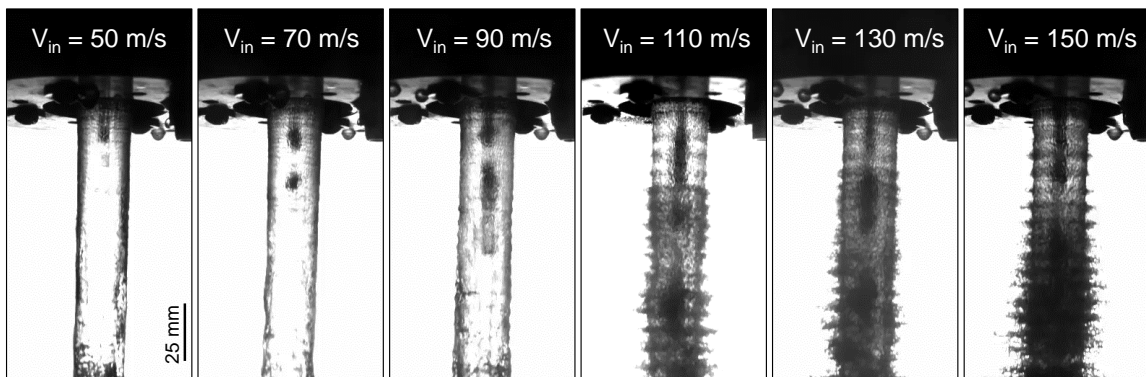
Figure 4-37 High speed imaging comparison of the cavitating jet for different inner jet velocities V_{in}.

The periodic nature of the cavitation cloud can be better observed in Figure 4-38 and Figure 4-39, where 15 representative high speed video frames at 7000^{-1} s intervals (143 µs) are shown for each inner jet velocity in Figure 4-37. As expected, the cloud penetration, the cloud size, and the wavy pattern intensity increase with inner jet velocity.

Figure 4-38 High speed video imaging of the cavitating flow for different inner jet velocities V_{in}. Video is captured at 14000 fps and frames are shown at 7000^{-1} s (143 μs) intervals (V_{out} = 11.0 m/s, frame numbers shown).
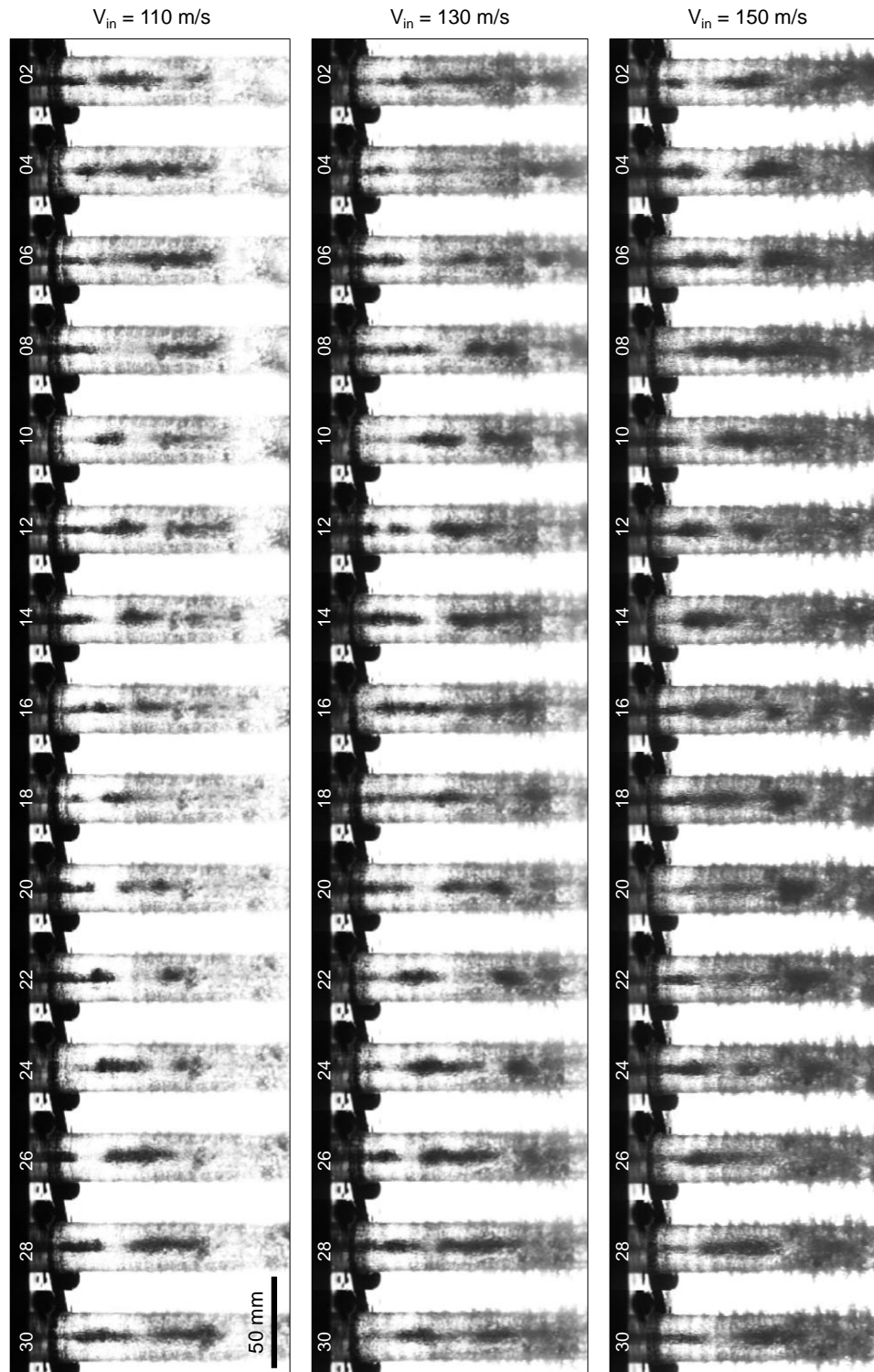
Figure 4-39 High speed video imaging of the cavitating flow for different inner jet velocities V_{in}. Video is captured at 14000 fps and frames are shown at 7000^{-1} s (143 µs) intervals (V_{out}= 11.0 m/s, frame numbers shown).

www.manaraa.com

In order to investigate this phenomenon quantitatively, the cloud width and the Power Spectral Density (PSD) were computed with the algorithm developed and described in section 4.2.3, and results are presented later in this section.
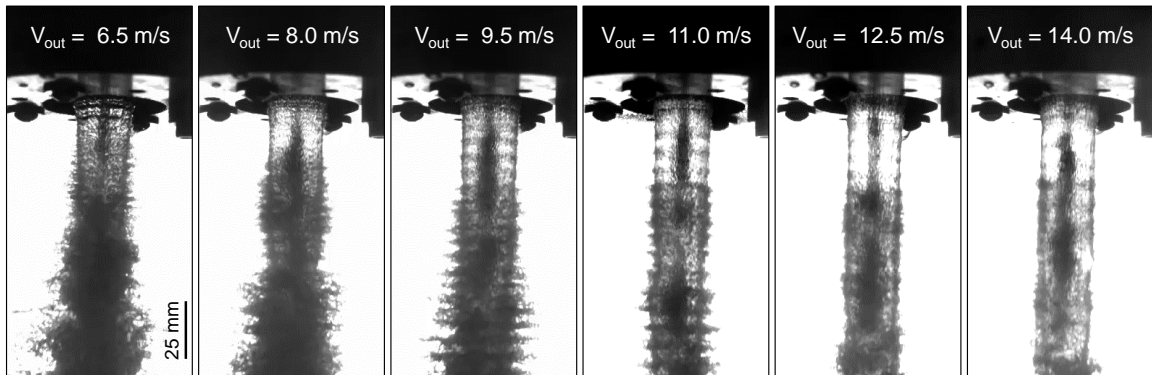
Figure 4-40 High speed imaging comparison of the cavitating jet for different outer jet velocities V_{out}.

Figure 4-40 shows of a comparison of the cavitating flows as the outer jet velocity V_{out} is increased from 6.5 m/s to 14.0 m/s. The figure reveals the disruption of the cavitating flow for $V_{out} \leq 8.0$ m/s. Flow disruption is caused by ability of the inner flow to accelerate the outer flow toward the center, reducing the cross section of the flow as well as its useful length. This phenomenon can be better observed in Figure 4-41 and Figure 4-42, where 15 representative high speed video frames at 7000^{-1} s intervals (143 µs) are shown for each outer jet velocity in Figure 4-40.
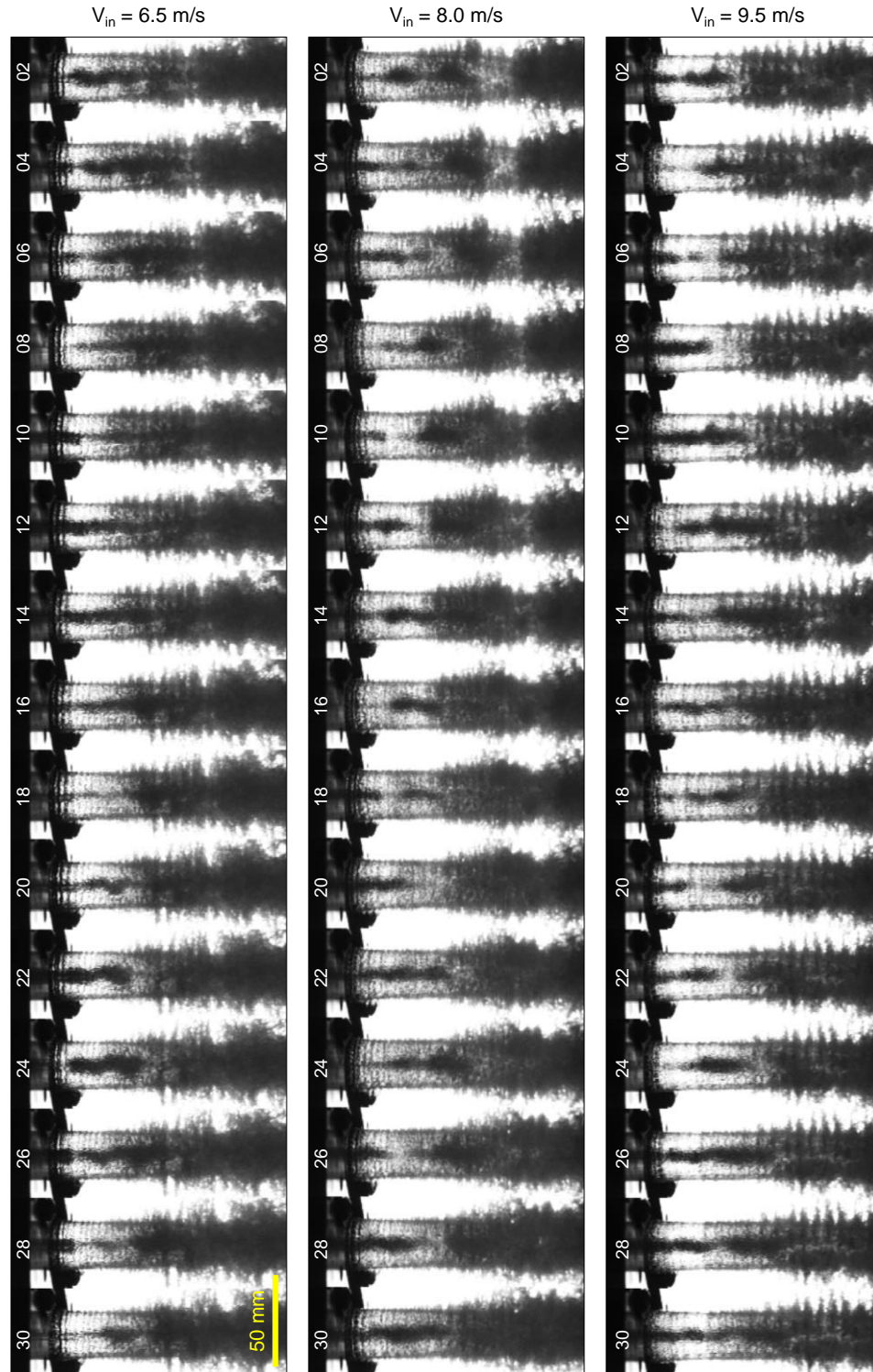
Figure 4-41 High speed video imaging of the cavitating flow for different outer jet velocities V_{out}. Video is captured at 14000 fps and frames are shown at 7000^{-1} s (143 μs) intervals (V_{in}= 150 m/s, frame numbers shown).
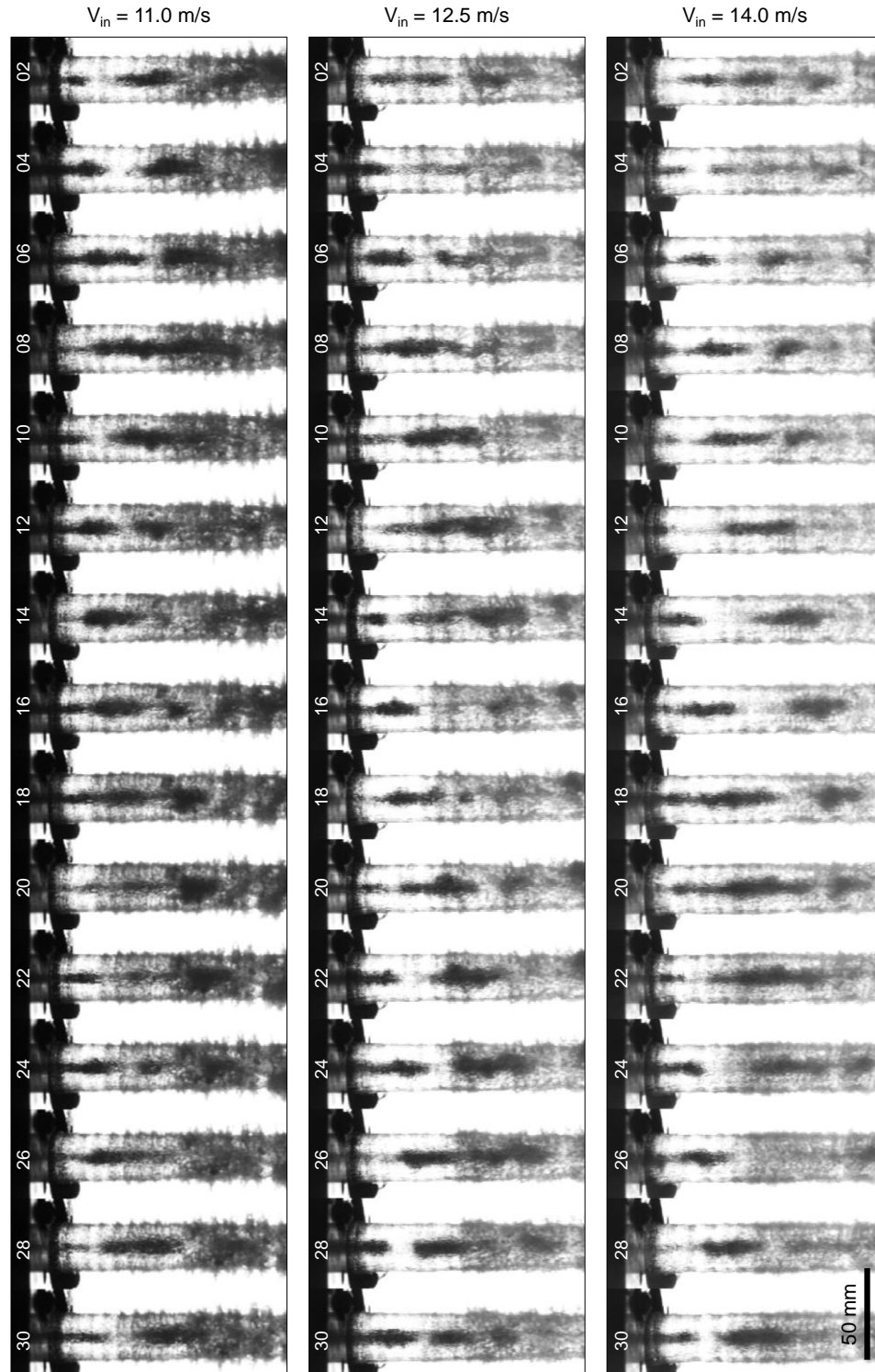
Figure 4-42 High speed video imaging of the cavitating flow for different outer jet velocities V_{out}. Video is captured at 14000 fps and frames are shown at 7000^{-1} s (143 μs) intervals (V_{in}= 150 m/s, frame numbers shown).

91

The maximum cloud width was computed for each cloud crossing a predetermined standoff distance as a function of the inner jet velocity, and the results are shown in Figure 4-43. Standard deviations and T-tests for statistical significance of the cloud width data reported in this chapter are available in Appendix A. As expected, an increase in the inner jet velocity from V_{in} = 90 m/s to V_{in} = 150 m/s causes an increase in the cloud width. Moreover, the cavitation cloud width is found to increase with the normalized standoff distance s_N for velocities $V_{in} \geq$ 110 m/s, as the cavitation cloud grows when it travels downstream. These results are in agreement with the trends seen in sections 4.3.1 and 4.3.2, where higher inner jet velocities led to higher cavitation intensities (mass loss) and strip curvatures.
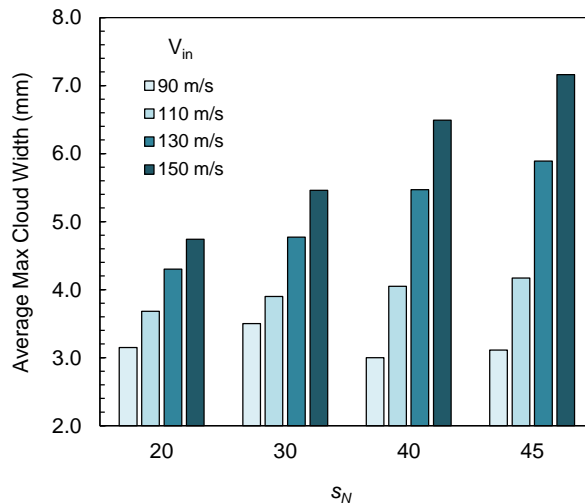
Figure 4-43 Average maximum cloud width as a function of inner jet velocity V_{in} for different standoff distances s_N (V_{out} = 11.0 m/s).

The maximum cloud width was also computed as a function of the outer jet velocity, and the results are reported in Figure 4-44. Larger cavitation cloud widths are found at lower outer flow velocities, since this condition maximizes the velocity difference between the inner and outer flows and therefore promotes the formation of the cavitation

cloud. This observation partially contradicts the accelerated erosion test results (Figure 4-26) where the outer flow velocity V_{out} = 9.5 m/s yielded a lower cavitation intensity compared to V_{out} = 11.0 m/s. An explanation for this contradiction can be found by looking at the total amount of cavitation produced by the flow, as shown in Figure 4-45, where the number of clouds per second is plotted for different outer flow velocities. In the plot, it can be seen that V_{out} = 9.5 m/s exhibits the lowest cloud count per second, and that the number of clouds per second rapidly decreases as the standoff distance increases to s_N =45. This observation suggests that overall more cavitation can be produced by reducing the velocity difference between the two flows (from 150-9.5 m/s to 150-11.0 m/s) allowing the cloud to be sustained at a larger standoff distance, with V_{out} = 11.0 m/s representing the condition that optimizes the trade-off between cloud size and cloud count for the cavitating flow analyzed in this study.
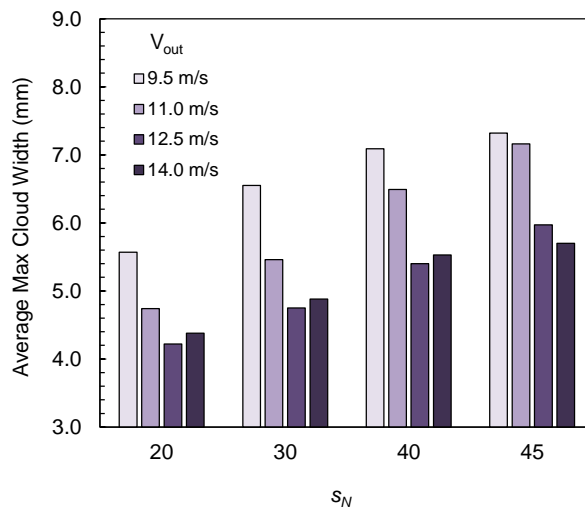
Figure 4-44 Average maximum cloud width as a function of outer jet velocity V_{out} for different standoff distances s_N (V_{in} = 150 m/s).
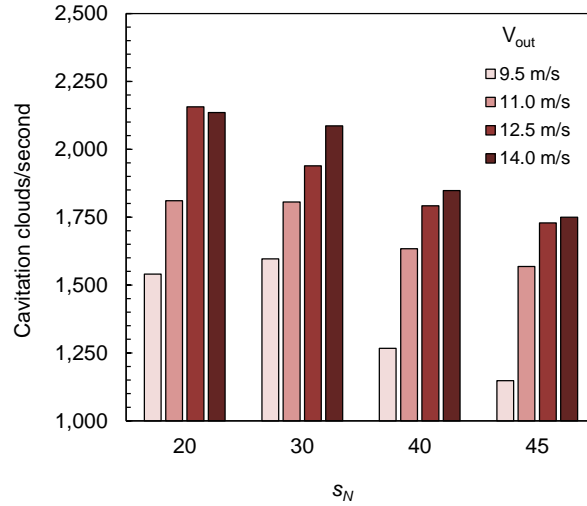
Figure 4-45 Number of cavitation clouds per second as a function of the outer jet velocity Vout for different standoff distances sN (Vin = 150 m/s).

The power spectral density (PSD) was computed for the inner jet velocity $V_{in} \geq 110$ m/s at standoff distances s_N of 20, 30, 40 and 45 and the results are shown in Figure 4-46. A peak near 2 kHz is observed for all the inner jet velocities at $s_N = 20$. The amplitude of this peak increases as V_{in} is increased, while its dominant frequency decreases slightly. As the standoff distance increases, the cavitation clouds grow in size as they flow downstream, in some cases merging with neighboring clouds as seen for $V_{in} = 150$ m/s mm in Figure 4-38. Consequently, the power distribution in the PSD shifts to lower frequencies with increase in s_N. Also, the total power is seen to increase monotonically as V_{in} and s_N increase. Finally, Figure 4-46 confirms the frequency range for the cavitation cloud reported by Soyama [101].

94
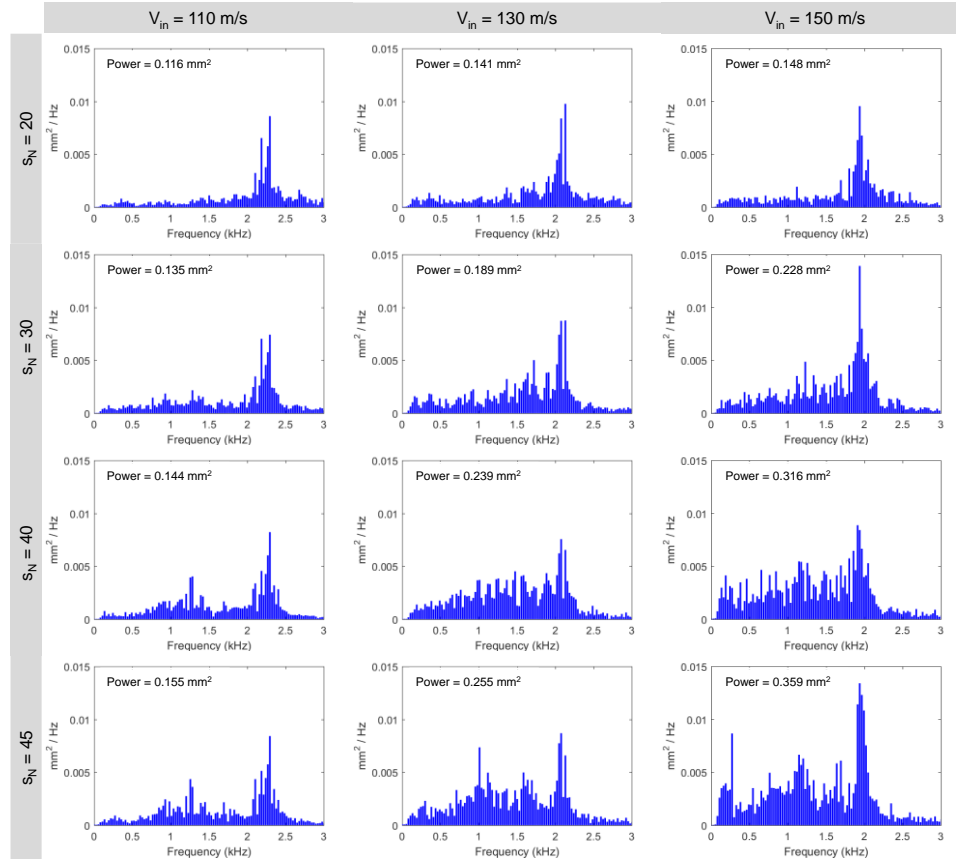
Figure 4-46 Power Spectral Density (PSD) of the cloud width variation for different V_{in} and different normalized standoff distances s_N (total power for each case reported in the top left of each PSD plot).

The PSD of the cloud width as a function of the outer jet velocity is shown in Figure 4-47 and Figure 4-48. As in the previous case, the flow exhibits frequency content in the [0 - 2kHz] range, with $V_{out} = 11.0$ m/s recording the highest power of all the cases presented, and matching the trends seen in the accelerated erosion tests and the strip curvature tests. Interestingly, at standoff distances $s_N = 30$, lower outer jet velocities ($V_{out} \leq$ 8.0 m/s) record higher total power in the considered [0 - 3kHz] band. Once again, this is believed to be due to the higher velocity difference between the two flows, allowing for more cavitation to be produced.
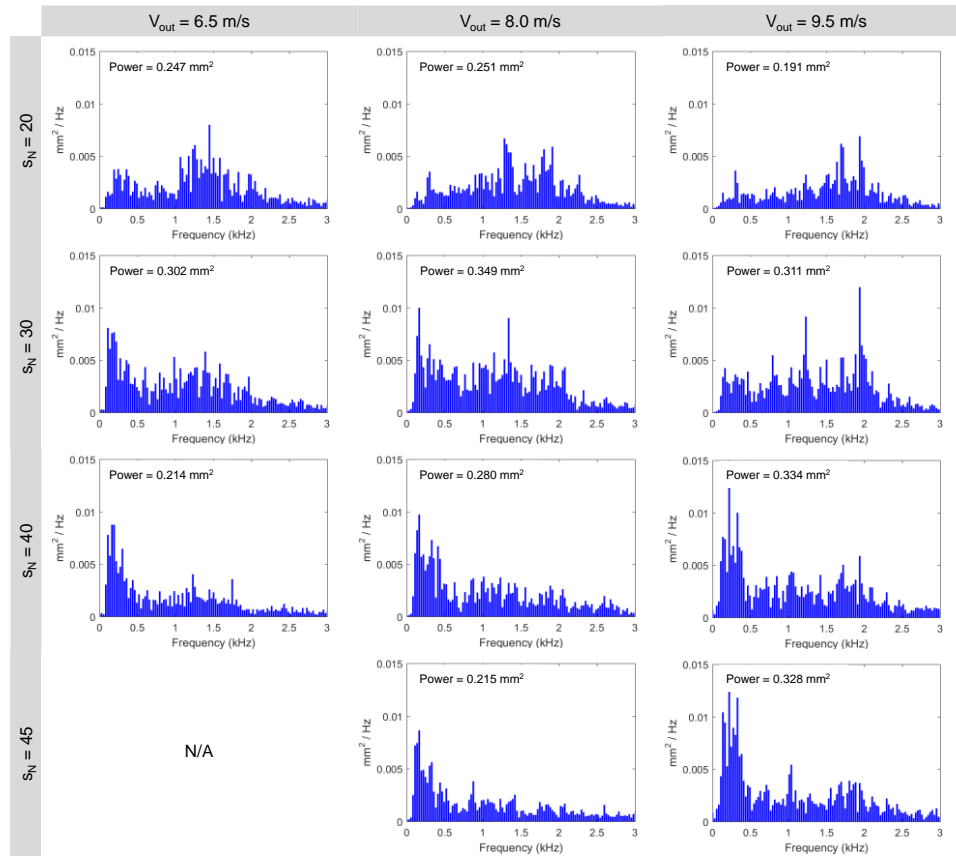
Figure 4-47 Power Spectral Density (PSD) of the cloud width variation for different V_{out} **(6.5-9.5 m/s) and different normalized standoff distances** s_N **(total power for each case reported in the top left of each PSD plot).**
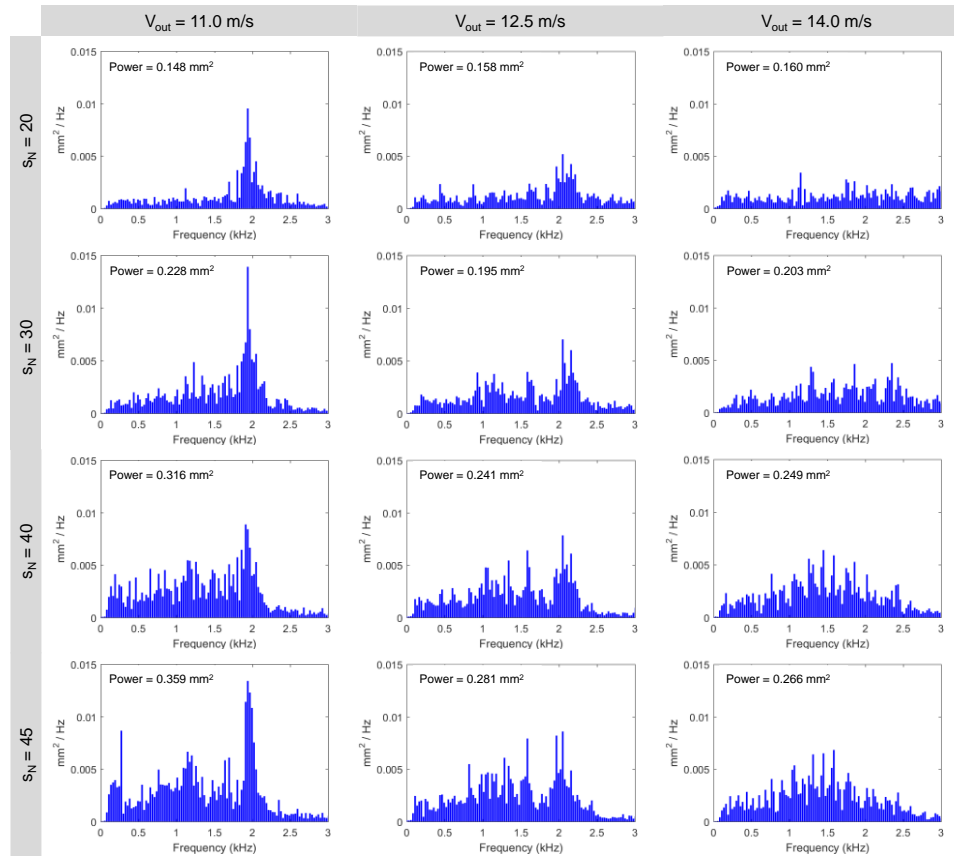
Figure 4-48 Power Spectral Density (PSD) of the cloud width variation for different V_{out} (11.0-14.0 m/s) and different normalized standoff distances s_N (total power for each case reported in the top left of each PSD plot).

4.4　Summary

This chapter presented an experimental study of the effect of flow velocities in co-flow type water cavitation jet peening. First, cavitation aggressiveness was assessed by means of accelerated erosion tests on soft aluminum Al 1100-O and Al 7075-T6. Second, peening performance was investigated through strip curvature tests on Al 7075-T6 samples for a selected subset of flow conditions. From the analysis of the results, the following conclusions can be drawn:

97

1. Two distinct regimes of operation exist in co-flow water cavitation peening, namely the *ring regime* and the *center regime*. The ring regime displays high mass loss distributed in a large ring-shaped region, while the center regime displays a low mass loss concentrated at the center of the cavitating jet. Despite the center regime showing a higher mass loss per unit area, the ring regime yielded the best performance in terms of the saturated strip curvature and therefore peening capability. The optimum peening conditions for the nozzle used in this study were found to be V_{in} =150m/s, V_{out} =11.0m/s and s_n=45 for the ring regime and V_{in} =150m/s, V_{out} =5.0 m/s and s_n=45 for the center regime. It is the author's belief that the performance of the center regime can be greatly enhanced by increasing the inner jet velocity through suitable redesign of the nozzle, as already shown by other authors [22]

2. The crater area in the accelerated erosion test (Al1100-O) increases with the inner jet velocity V_{in} and peaks at 9.5< V_{out} <12.5 m/s and 40<s_n<50.

3. For the nozzle used in this study, the outer jet velocity V_{out} that maximizes erosion and peening capability is independent of the inner jet velocity V_{in} and equal to V_{out} =11.0 m/s. This value is also found to maximize the crater area, and is believed to represent the equilibrium point between two competing phenomena, namely cavitation generation, which is proportional to (V_{in} -V_{out}) and cavitation transportation, which is proportional to V_{out}.

4. The optimum normalized standoff distance is equal to 40≤s_n≤45 for all the jet velocity combinations considered in this study. Major changes in optimum s_n are expected if the nozzle geometry is varied [142]

98

5. Erosion tests on Al1100-O lead to inaccurate conclusions regarding the influence of the inner and outer jet velocities on the peening performance of Al 7075-T6 strips. Moreover, higher variability is observed, which is believed to be inherent in the erosion process.

6. Erosion tests on Al 7075-T6 are found to capture the influence of different flow parameters on the peening capability for the same material. Moreover, both erosion tests and strip curvature tests on Al 7075-T6 show very good repeatability, which makes them more suitable for assessment of peening performance.

7. Surface roughness was found to increase during peening (up to 2.2 µm), and was observed to closely follow the strip curvature trends.

8. High speed video observations of the cavitation flow confirm the trends observed in the accelerated erosion tests showing an increase in cloud size as a function of inner jet velocity V_{in}. Moreover, cloud analysis showed the outer flow velocity $V_{out} = 11.0$ m/s being the optimum trade-off between cloud size and the amount of generated clouds by the flow. Finally, the spectral analysis of the cloud diameter evolution confirmed the results from the accelerated erosion tests showing the highest power content for the optimum case $V_{in} = 150$m/s, $V_{out} = 11.0$m/s and $s_n = 45$.

CHAPTER 5.   EFFECT OF NOZZLE GEOMETRY IN CO-FLOW WATER CAVITATION PEENING

5.1   Overview

Water Cavitation Peening (WCP) uses cavitation to introduce compressive residual stresses in metals while limiting the surface roughening typical of similar mechanical processes such as shot peening and laser shock peening. As shown by a number of studies, cavitation intensity depends strongly upon the jet velocity, as well as the nozzle geometry. This paper investigates how varying nozzle dimensions affects cavitation intensity and peening performance in co-flow WCP of Al 7075-T651. Cavitation intensity is observed to increase with both inner and outer jet diameters (D_1 and D_2, respectively) with no further increase for $D_2 > 24.0$ mm. The scalability of co-flow WCP is investigated by comparing nozzles of different diameters while keeping the diameter ratio D_1/D_2 constant. Results reveal a substantial increase in cavitation intensity with nozzle size and a considerable decrease in the processing time required for saturation of the strip curvature and residual stress. The process yields compressive residual stresses as high as 400 MPa that extend up to 350 µm below the surface, a significant improvement upon the results reported for shot peening. An increase in the nozzle offset h is found to marginally increase cavitation intensity. Finally, the optimum normalized standoff distance s_N and the outer flow velocity V_{out} identified in prior work are not affected by the changes in nozzle configuration studied here.

5.2 Experimental Procedure

5.2.1 Accelerated Erosion Tests

Cavitation intensities produced by different nozzle geometries were evaluated by exposing fixed locations on samples of Aluminum 7075-T651 to the cavitating flow for an extended period of time (beyond the *incubation period* [143]), according to the ASTM standard G134 [21], until the onset of erosion (and therefore mass loss). Although mass loss is not desirable in peening, it serves to quantify the nozzle's effectiveness in producing cavitation. Once cavitation intensity was established through the accelerated erosion tests, actual peening tests were performed by exposing the workpiece surface to the cavitating jet for a short duration (below the *saturation time* [15]) to induce residual stresses without any mass loss.

The flow conditions for the erosion tests were selected based on the results reported in [114], where optimum peening conditions for the standard nozzle geometry (reported in Table 5-1) were investigated and identified. Normalized standoff distance s_N ($s_N=s/D_1$) values of 40, 45 and 50 were used, while the outer flow velocity $V_{out} = 11$ m/s and inner flow velocity $V_{in} =150$ m/s were kept constant, except when D_2 and H were varied. Water temperature was maintained at $21\pm3°C$ with the help of a water chiller. Mass loss was measured using an analytical balance with 0.1 mg resolution and 0.3 mg repeatability. Average flow velocities at the nozzle exit was determined by dividing the volumetric flow rate Q, measured by an inline turbine flow meter (with 1% accuracy), by the orifice cross-sectional area A_o, determined from the diameter which was measured using an optical comparator with 5 μm accuracy.

101

Table 5-1 Dimensions for the standard peening nozzle.

Feature	Dimension	Ratio ($/D_1$)
D_1	0.85 mm	1
D_0	12.8 mm	15
D_2	24.0 mm	28.2
D_4	6.80 mm	8
L_1	2.98 mm	3.5
H	0	0
β, γ	75°, 70°	-

5.2.2 Strip Curvature Tests

Evaluation of residual stress using measurement techniques such as X-ray diffraction (XRD) and hole drilling is generally time consuming and expensive. In contrast, strip curvature tests are routinely used in industry to quickly evaluate the peening performance [23, 24]. The curvature produced by the plastic deformation induced by the peening process is assumed to be an indirect measure of the change in residual stress generated in the metal sample. Aluminum 7075-T651 was selected as the test material to ensure an approximately stress-free state in the strips prior to peening. The material follows the standard ASTM

102

B209 and was received in plate form with initial dimensions of 600 mm x 76 mm x 9.5 mm. The plates were cut by wire-EDM into 19 mm x 76 mm x 9.5 mm strips, which were used in the peening experiments. The scanning speed and pitch of the nozzle, which is mounted on an X-Y gantry, were 480 mm/min and 1 mm, respectively, for all flow conditions studied. The peening time t_P is defined as the time required to peen the entire sample, and for a given strip geometry it is a function of the scanning speed and pitch. To ensure homogeneous treatment of the strip, the samples were peened using the same scan path shown in the previous chapter, where the trajectory of the nozzle starts and ends outside the sample boundary. Each strip was subjected to six full passes amounting to a total peening time t_P of 18 min, which was previously identified as the saturation time for the material [114]. Based on the saturation criterion adopted, the strip curvature, and therefore the residual stresses, are not expected to increase beyond the processing time used in this study. The exposure time t_E is defined as the time duration a unit area of material is exposed to the cavitating flow. In the case of accelerated erosion tests, where the nozzle is stationary, the exposure time is equal to the entire duration of the erosion test. For peening tests, the exposure time t_E is a function of the scanning speed and pitch, as well as the cavitating jet area (A_C), which is a function of the nozzle geometry, jet velocities, and standoff distance. The procedure to compute the exposure time is the same as developed in the previous chapter.

The curvatures of the peened aluminum 7075-T651 strips were assessed from surface profile measurements made using a coordinate measuring machine (Brown & Sharpe 4.5.4 SF) as shown in Figure 5-1.

103
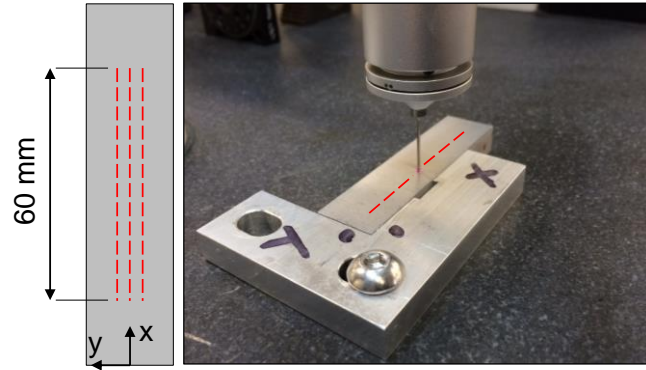
Figure 5-1 Strip curvature measurement.

As illustrated in Figure 5-1, three 60 mm long profiles at y=0, y= +3, and y= -3 mm were measured for each peened strip, respectively, then averaged along the x direction to obtain the average surface profile for a given strip. The average profile for the original (un-peened) strip was then subtracted from the average profile for the peened strip to obtain the net peened strip profile. Figure 5-2 shows examples of the measured and average surface profiles for the original and peened strips (left), as well as the net peened strip profile (right).
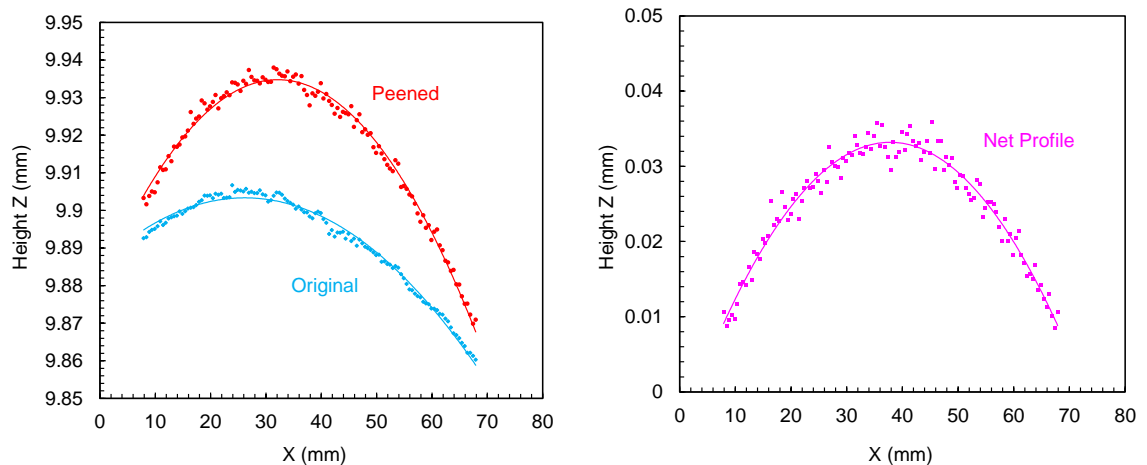
Figure 5-2 Strip profiles for the original and peened conditions (left),
and net strip profile (right).

104

5.2.3   Experimental Design

5.2.3.1   Effect of Inner Flow Diameter D_1

The effect of diameter D_1 on the peening capabilities of a cavitating jet in a co-flow configuration was studied by varying D_1 as shown in Table 5-2. These values were selected based on the pressure and flow rate limitations of the cavitation peening apparatus described earlier.

Table 5-2 Nozzle geometry for the inner flow diameter study.

D_1 (mm)	D_0 (mm)	D_2 (mm)	D_4 (mm)	L_1 (mm)
0.75				
0.85	12.8	24.0	6.80	2.98
0.95				

Nozzle dimensions such as orifice length L and nozzle internal diameter D_4 were kept constant. The normalized standoff distance s_N was varied between 35 and 50, while the outer flow velocity $V_{out} = 11$ m/s and the inner flow velocity $V_{in} = 150$ m/s were kept constant for both the accelerated erosion and the strip curvature tests.

Table 5-3 Test conditions for accelerated erosion and peening tests.

V_{in} (m/s)	V_{out} (m/s)	s_N (-)	t_E (min) (Erosion)	t_P (min) (Peening)
		35		
		40		
150	11.0	45	30	18
		50		

The exposure time t_E for the erosion tests was set to 30 min while the peening time t_P for the strip curvature tests was set to 18 min, which is equivalent to six full passes of the strip at the scanning speed and scanning pitch values stated earlier.

5.2.3.2   Effect of Outer Flow Diameter D_2

The effect of diameter D_2 on the peening capabilities of a cavitating jet in a co-flow configuration was investigated by varying D_2 according to Table 5-4 and using the flow conditions given in Table 5-3. The outer flow velocity V_{out} was kept constant by increasing the outer flow rate to compensate for changes in D_2.

Table 5-4 Nozzle geometry for outer flow diameter study.

D_1 (mm)	D_0 (mm)	D_2 (mm)	D_4 (mm)	L_1 (mm)
		21.2		
0.85	12.8	24.0	6.80	2.98
		26.8		

5.2.3.3   Nozzle Scalability Study

The goal of this experiment was to investigate how cavitation intensity and strip curvature scale with nozzle dimensions when D_1 is varied between 0.75 mm and 0.95 mm while keeping diameter ratios ($D_1{:}D_0{:}D_2$) constant. Three nozzles – designated S, M, and L – were fabricated. The corresponding nozzle dimensions and the flow conditions used in the experiment are summarized in Table 5-5. The dimensions of the S, M, and L nozzles were selected based on previous work [114] and the flow rate limitations of the cavitation peening apparatus. The flow velocities V_{in} and V_{out} were maintained constant by increasing the corresponding flow rates to compensate for the change in diameter.

107

Table 5-5 Nozzle dimensions and flow conditions for the scalability study.

Nozzle	D_1 (mm)	D_0 (mm)	D_2 (mm)	D_4 (mm)	L_1 (mm)	V_{in} (m/s)	V_{out} (m/s)	s_N (-)	t_E (min) (Erosion)	t_P (min) (Peening)
S	0.75	11.3	21.2	6.00	2.63					18
M	0.85	12.8	24.0	6.80	2.98	150	11.0	40 45 50	30	18
L	0.95	14.3	26.8	7.60	3.33					12

5.2.3.4   Effect of Nozzle Offset

The effect of normalized nozzle offset h ($h=H/D_1$) on the peening capabilities of a co-flow cavitating jet was investigated for h = 0, 4 and 7. Vijay et al. [22] previously observed that cavitation intensity varied considerably with h, reporting a 150% improvement for h=3.9 over the baseline of h=0. Unfortunately, the outer flow rate was constant in their study, thereby producing a variation in the outer flow velocity V_{out} as a function of the offset h. As a result, it cannot be conclusively determined if the changes in cavitation intensity reported by Vijay et al. are solely due to changes in the nozzle offset, or if they are due to the change in flow velocity derived from the variation in h. In order to address this issue, three co-flow experiments under flow conditions representative of the ring regime [6] were first conducted prior to investigating the effect of h. The first experiment investigated the effect of offset h on the optimum normalized standoff distance s_N and also

108

enabled the identification of the proper criterion for determining its value as h is varied. The second experiment investigated the difference between a constant flow velocity approach and a constant flow rate approach to determine how to adjust the flow conditions as a function of h in order to obtain meaningful and consistent results.

5.2.4   High Speed Imaging and Analysis

The cavitating flow was imaged and analyzed with the same technique developed for the characterization of the cavitating flow, the reader is invited to refer to Chapter 4 for the details on this analysis.

5.2.5   Residual Stress Measurement

The residual stress generated by WCP was measured by XRD using the two-angle $\sin^2\psi$ technique, in accordance with SAE HS-784, employing the Cr-Kα radiation from the (311) planes of the FCC structure of aluminum 7075-T65. The angular positions of the diffraction peaks at each of the ψ tilts (10° and 50°) employed for measurement were determined from the position of the $K\alpha 1$ diffraction peak.   For through-thickness residual stress measurement, layer removal via electro-polishing was used to minimize possible alteration of the subsurface residual stress distribution as a result of material removal. The results obtained as a function of depth were corrected for the effects of penetration of the X-ray into the subsurface and for stress relaxation caused by sectioning and layer removal. The residual stress measurements were performed by Lambda Technologies (Cincinnati, OH).

5.3   Results and Discussion

5.3.1   Effect of Inner Flow Diameter D_1

109

The effect of nozzle diameter D_I on the cavitation intensity and crater area in accelerated erosion tests can be observed in Figure 5-3 and Figure 5-4 respectively. As expected, an increase in mass loss is observed at larger D_I as the momentum of the jet is increased due to increase in the flow rate required to maintain a constant average velocity. The optimum normalized standoff distance s_N is observed to decrease with increasing inner jet diameter, confirming the results of Vijay et al.[22]. Crater area increases with inner jet diameter for $D_I \leq 0.85$ mm; for $D_I > 0.85$ mm; the maximum crater area remains constant, but occurs at lower standoff distances s_N. An explanation is offered later in this section. Overall, the results shown in Figure 5-4 confirm the findings reported elsewhere by the authors [6], with maximum cavitation intensity (mass loss) occurring at the flow conditions maximizing the crater area.

Inner jet diameters $D_I = 0.85$ mm and $D_I = 0.95$ mm at normalized standoff distances s_N of 45 and 40, respectively, were selected for the strip curvature study. Figure 5-5 shows the net strip profile (and hence curvature) for the $D_I = 0.95$ mm case is higher than that for the $D_I = 0.85$ mm, implying that a larger inner jet diameter produces a larger change in the residual stress state.
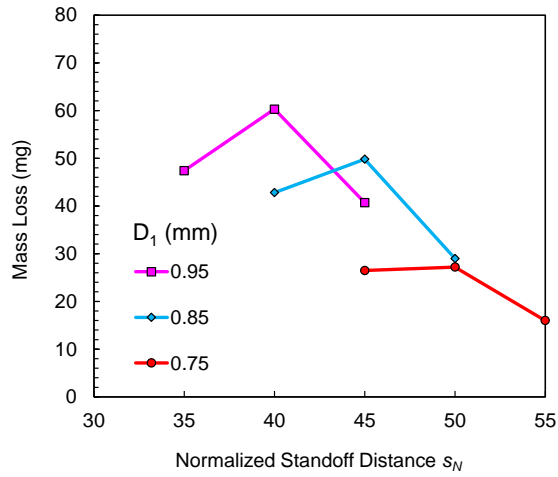
Figure 5-3 Mass loss as a function of normalized standoff distance s_N for different inner flow diameters D_1 (V_{in}= 150 m/s, V_{out}= 11.0 m/s, Al 7075-T651, t_E= 30 min).
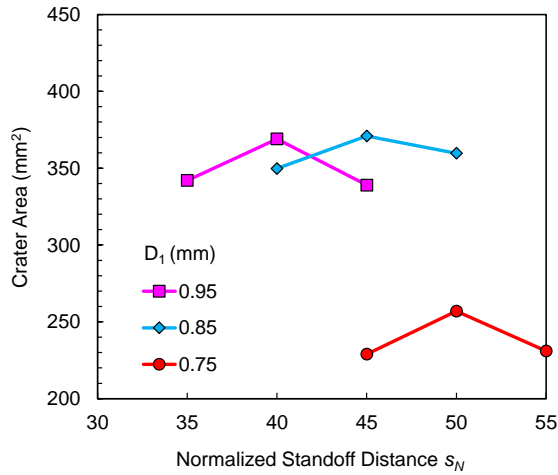
Figure 5-4 Crater area as a function of normalized standoff distance s_N for different diameters D_1 (V_{in}= 150 m/s, V_{out}= 11.0 m/s, Al 7075-T651, t_E= 30 min).

111
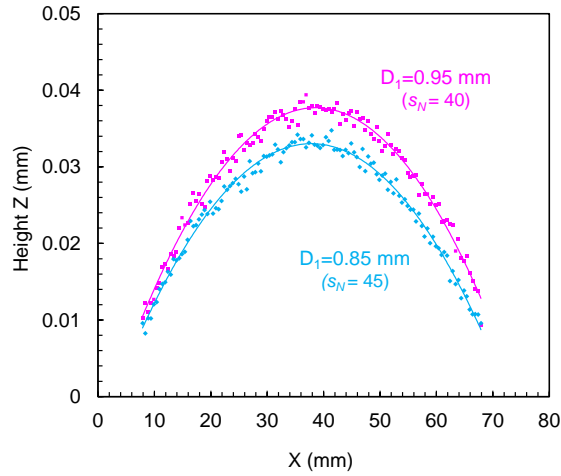
Figure 5-5 Net strip profile variation for different inner flow diameters D_1 ($D_2 = 24.0$ mm, $V_{in}= 150$ m/s, $V_{out}= 11.0$ m/s, Al 7075-T651, $t_P= 18$ min).

Figure 5-6 shows a sequence of 15 representative images at 7000 Hz (from a video obtained at 14000 Hz), corresponding to 143 µs between consecutive images, for each flow condition corresponding to the inner jet diameter experiment.

112
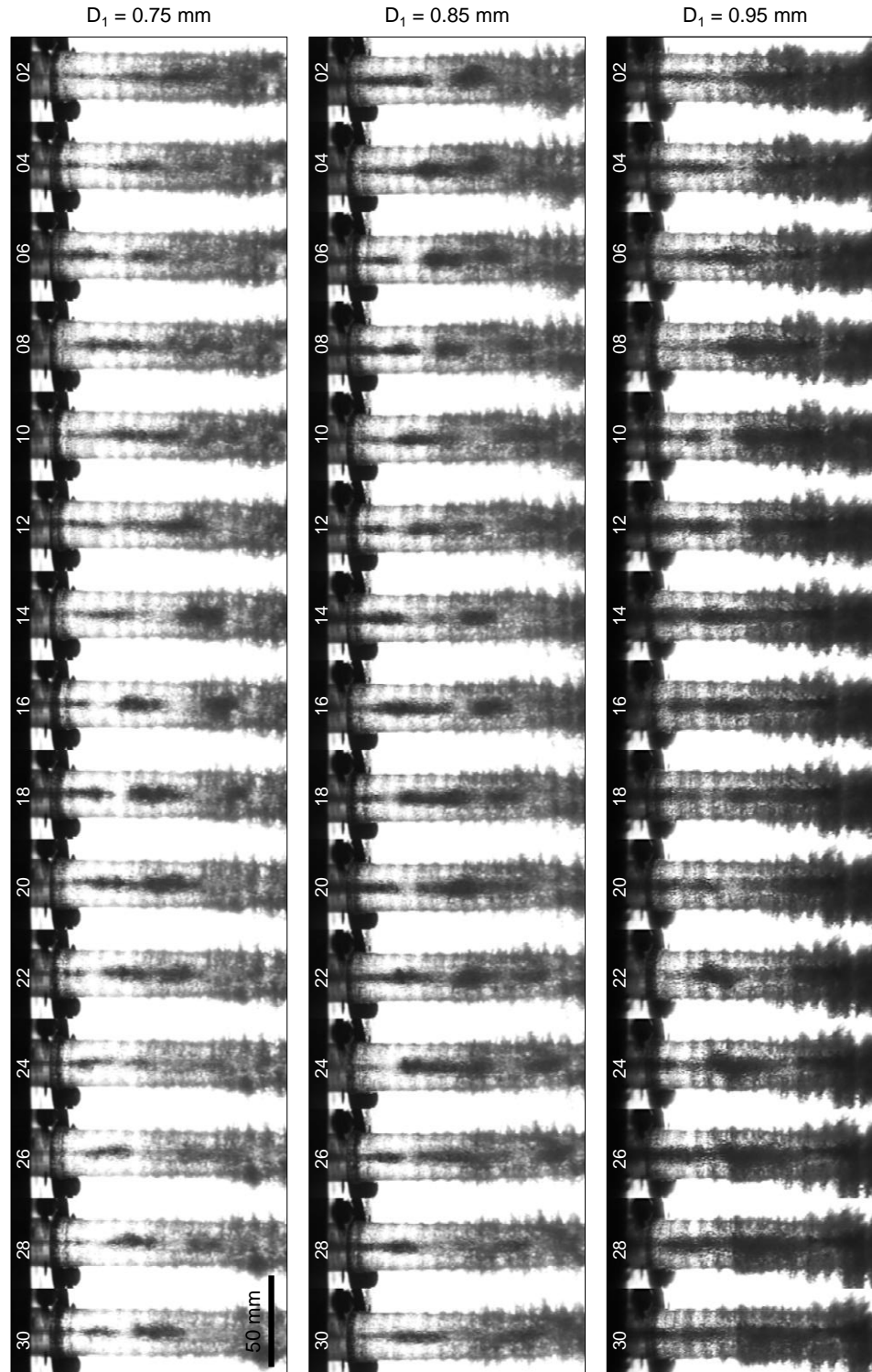
Figure 5-6 Sequence of 15 images of the cavitating flow for different diameters D_1. This sequence represents every second image of videos captured at 14000 fps; the interval between frames is 143 µs (V_{in}= 150 m/s, V_{out}= 11.0 m/s, frame numbers shown).

113

The periodic nature of the cavitating clouds in Figure 5-6 has been previously described by Soyama et al. [101, 120, 121, 144] for both the submerged and co-flow configurations. The periodicity of the cavitating cloud is a desirable feature of the flow, as pulsating jets are reported to produce higher cavitation intensity compared to non-pulsating jets [109]. The wavy pattern is the result of cavitation cloud pulsation and has the same characteristic frequencies as the cloud pulsation (0.5 – 2 kHz, Soyama [101]). Figure 5-6 also reveals that the intensity of the wavy pattern increases with nozzle diameter D_I for a given inner jet velocity V_{in}. This is believed to be caused by an increase in cavitation cloud size with increase in the inner jet diameter, as shown in Figure 5-7, with large diameters D_I generating larger cavitation clouds. The increase in cloud size can also explain the change in optimum standoff distance described previously. The inner flow accelerates the outer flow in the mixing layer, causing, by continuity, a reduction in the cross sectional area of the combined jets and the consequent earlier disruption of the cavitating flow. An increase in D_I promotes an earlier disruption of the flow, therefore shifting upstream the location of the maximum crater area as seen in Figure 5-4. It is important to note that while the cloud size analysis captures the overall trends observed in the erosion and curvature tests, the width of the cavitation cloud increases monotonically with standoff distance. These visualizations therefore do not capture the decrease in cavitation erosion generally observed downstream of $s_N \sim 45$ (Figure 5-3). The case $D_I = 0.95$ mm and $s_N = 40$ gave higher average maximum cloud width (7.63 mm) and mass loss (60.3 mg) than the case $D_I = 0.85$ mm and $s_N = 45$ (7.16 mm and 49.8 mg, respectively), thus establishing a good correlation between the optimum cases for the two inner jet diameters. Downstream of $s_N \approx 45$, cavitation cloud width alone cannot explain the results proposed in Figure 5-3 and

114

Figure 5-5, and other factors, such as crater area (Figure 5-4), have to be taken into consideration.
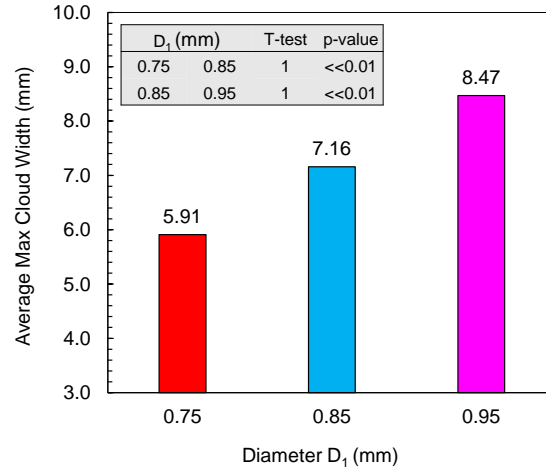
Figure 5-7 Average maximum cloud width as a function of inner jet diameter D_1 for different standoff distances s_N.

The power spectral density (PSD) was computed for each diameter D_1 at standoff distances s_N of 20, 30, 40 and 45 and the results are shown in Figure 5-8. A peak near 2 kHz is observed for all the diameters at $s_N = 20$. The amplitude of this peak increases as D_1 is increased from 0.75 to 0.95 mm. As the standoff distance increases, the cavitation clouds grow in size as they flow downstream, in some cases merging with neighboring clouds as seen Figure 5-6 for $D_1 = 0.95$ mm (frames 26-30). Consequently, the PSD peak shifts to lower frequencies with increase in s_N, with $D_1 = 0.95$ mm in particular yielding the highest amplitude at frequencies ≤ 300 Hz. Also, no significant increase in the total power is observed for $D_1 = 0.95$ mm past $s_N = 40$, which corresponds to the optimum standoff distance for this case. Finally, Figure 5-8 shows that the frequency range for the cavitation cloud observed here is similar to that reported by Soyama [101].
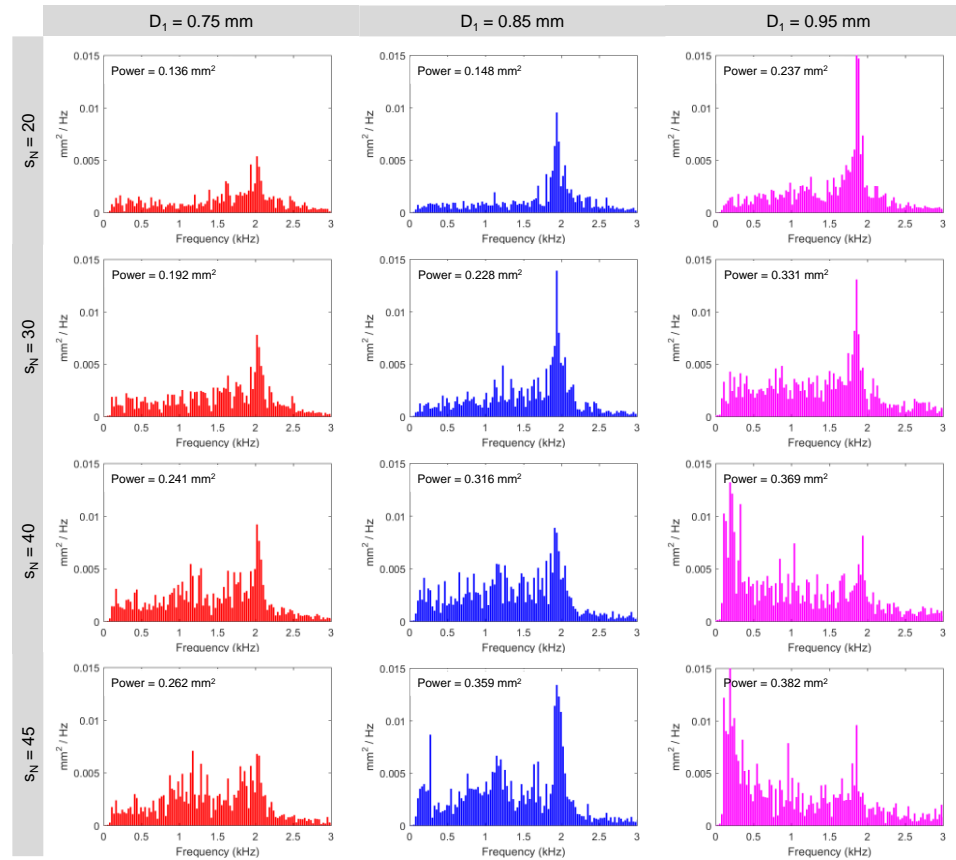
Figure 5-8 Power Spectral Density (PSD) of the cloud width variation for different D_1 and different normalized standoff distances s_N (total power for each case reported in the top left of each PSD plot).

5.3.2   Effect of Outer Flow Diameter D_2

Figure 5-9 shows the results of the accelerated erosion tests as a function of the outer flow diameter D_2. A significant increase in mass loss is observed when the outer diameter increases from 21.2 mm to 24 mm, but a further increase in D_2 to 26.8 mm produces no measurable increase in mass loss. This suggests that for a given inner jet velocity V_{in} and diameters D_1 and D_0, a minimum outer flow rate and outer diameter combination is required to achieve a condition approaching the fully submerged jet case for $s_N \leq 45$, where the boundary conditions of the outer flow are no longer affecting the inner jet and no additional benefit is derived from further increasing the outer flow diameter D_2. It can also

be seen that with a decrease in D_2 from 24.0 mm to 21.2 mm, the maximum mass loss

occurs at a shorter normalized standoff distance. This is due to the ability of the inner flow

to accelerate the outer flow toward the center, reducing the crater area and causing earlier

disruption of the cavitating flow, as already discussed in this previous section. Crater area

(Figure 5-10) increases with outer diameter for all the considered cases, including $D_2 = 26.8$

mm. This is caused by an increase in the pitting region surrounding the cavitation crater

rather than the crater itself, as illustrated in Figure 5-11.
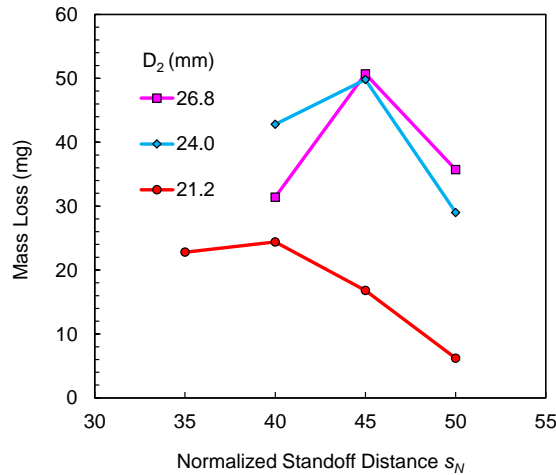
Figure 5-9 Mass loss as a function of normalized standoff distance s_N for different outer flow diameters D_2 (V_{in}= 150 m/s, V_{out}= 11.0 m/s, Al 7075-T651, t_E= 30 min).

The effect of outer flow velocity V_{out} was also investigated for D_2=26.8 mm to verify the

assumption of $V_{out} = 11$m/s as the optimum condition for the nozzle, as reported elsewhere

by the authors [6]. For this purpose, the outer flow velocity was varied between 9.5 and

12.5 m/s, and the normalized standoff distance was varied between 40 and 50. The results,

shown in Figure 5-12, confirm that the optimum outer flow velocity is not affected by D_2.

117
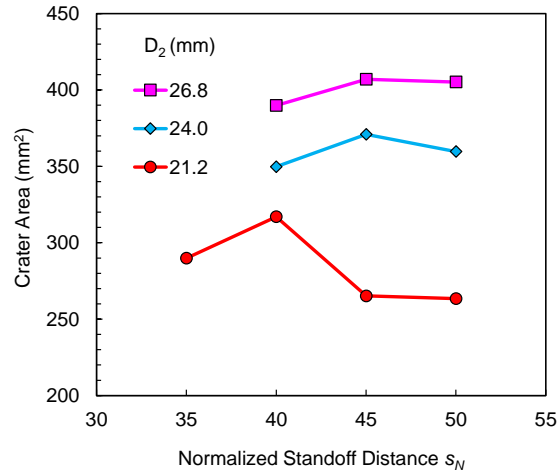
Figure 5-10 Crater area as a function of normalized standoff distance s_N for different diameters D_2 (V_{in}= 150 m/s, V_{out}= 11.0 m/s, Al 7075-T651, t_E= 30 min).
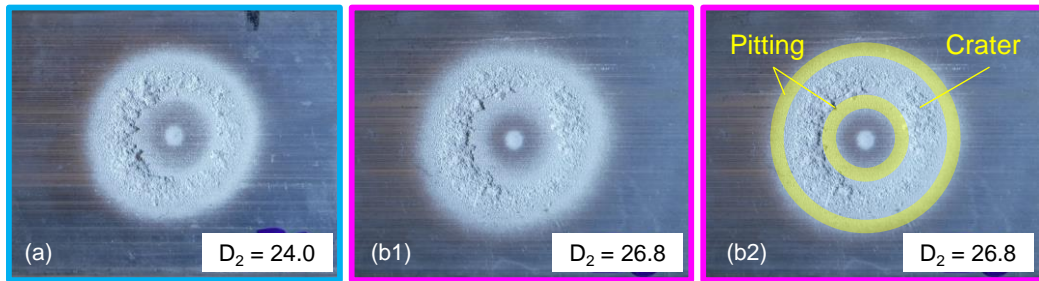
Figure 5-11 Crater area for different diameters D_2 at s_N = 45. Case (b) reports larger surface area because of the increased pitting region compared to case (a) (V_{in}= 150 m/s, V_{out}= 11.0 m/s, Al 7075-T651, t_E= 30 min).

The results for strip curvature tests at s_N = 45 for D_2 = 24 mm and D_2 = 26.8 mm, and at s_N = 40 for D_2 = 21.2 mm are shown in Figure 5-13. An exceptional correlation between the erosion tests and the strip curvature tests is found, with the mass loss and net strip profile results overlapping perfectly for D_2 = 24 mm and for D_2 = 26.8 mm.

118
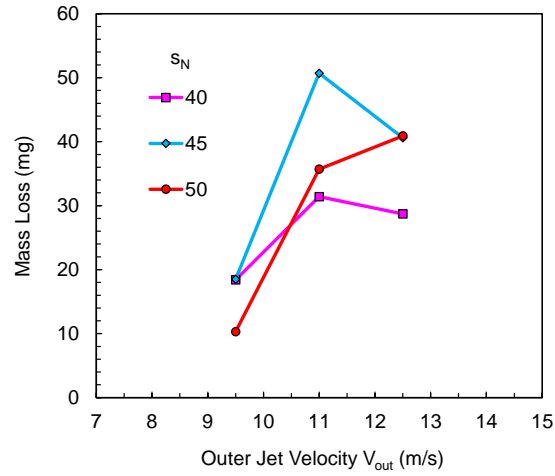
Figure 5-12 Mass loss as a function of normalized standoff distance s_N for different outer flow velocities V_{out} (V_{in}= 150 m/s, D_2 = 26.8 mm, Al 7075-T651, t_E= 30 min).
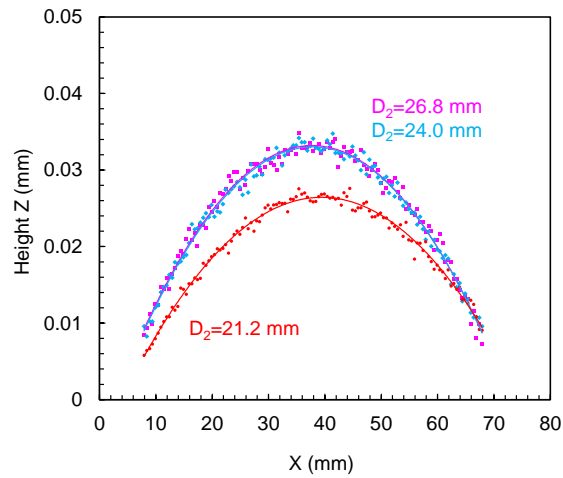
Figure 5-13 Net strip profiles for different outer flow diameters D_2 (D_1 = 0.85 mm, V_{in}= 150 m/s, V_{out}= 11.0 m/s, Al 7075-T651, t_P= 18 min).

119
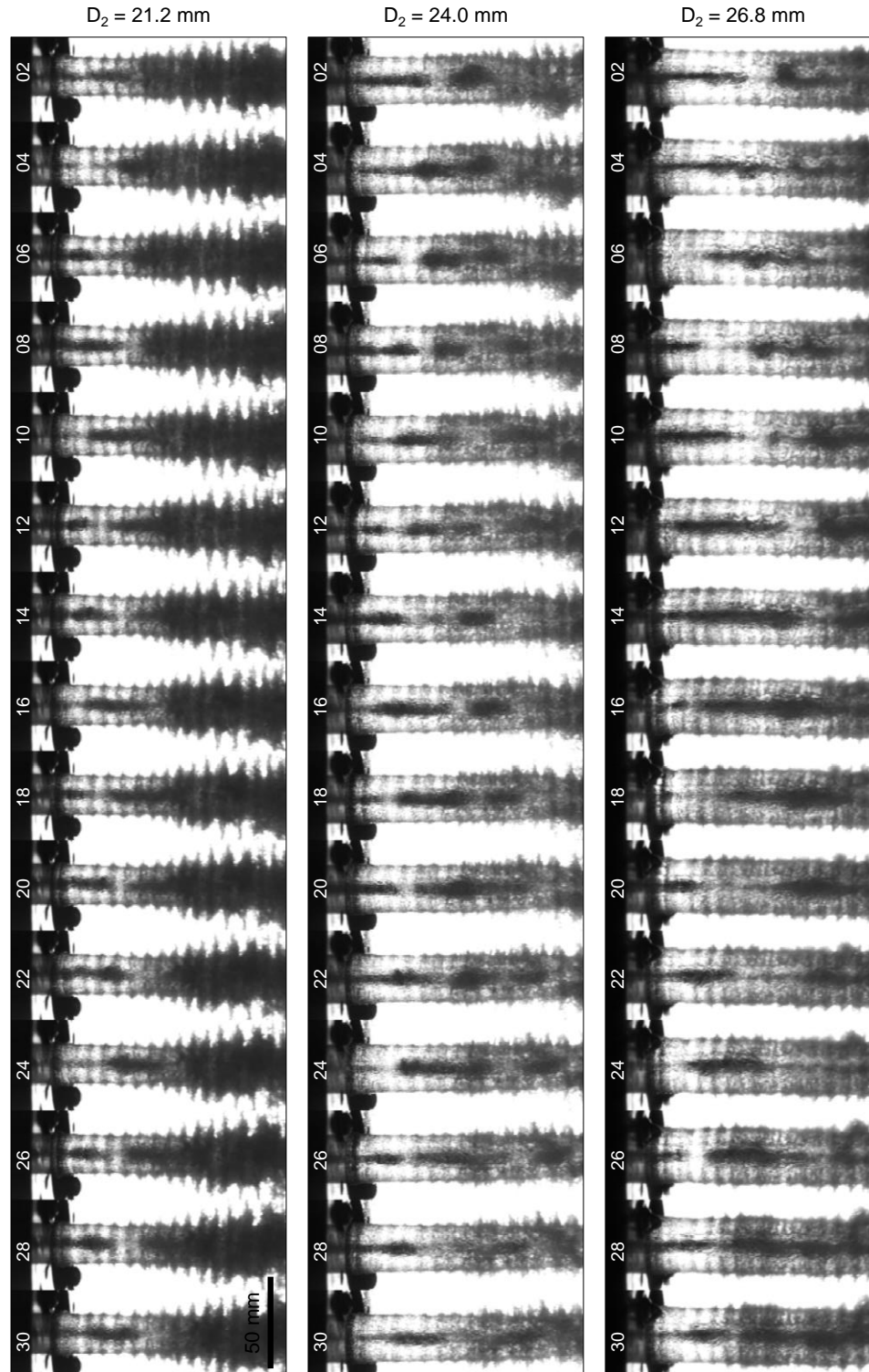
Figure 5-14 Sequence of 15 images of the cavitating flow for different diameters D_2. This sequence represents every second image of videos captured at 14000 fps; the interval between frames is 143 µs (V_{in}= 150 m/s, V_{out}= 11.0 m/s, frame numbers shown).

120

Figure 5-14 shows a sample of the high speed video frames as a function of D_2. It can be seen from the figure that the flow is disrupted farther upstream at lower values of D_2. This flow disruption is believed to be responsible for the shift in optimum standoff distance s_N as discussed previously. No significant changes are observed in the average maximum cloud width for $D_2 = 24.0$ mm and $D_2 = 26.8$ mm, with the average maximum cloud width for $D_2 = 26.8$ mm being marginally less than for $D_2 = 24.0$ mm. This observation supports the explanation discussed earlier of the flow approaching the fully submerged jet case for $s_N \leq 45$ where the boundary conditions in the outer flow are no longer affecting the inner jet (Figure 5-15). Note that the average maximum cloud width results for D_2=21.2 mm are not reported in Figure 5-15 because of the interference of the wavy pattern at short standoff distances, causing the cloud width to be consistently overestimated.

Figure 5-15 Average maximum cloud width as a function of outer jet diameter D_2 for different standoff distances s_N.

The PSD was also computed for $D_2 = 24.0$ mm and $D_2 = 26.8$ mm at increasing standoff distances and the results are shown in Figure 5-16. Once again, a peak around 2 kHz at s_N =20 is observed, with energy content at lower frequencies increasing with standoff

121

distance. The variation in total power with increase in D_2 is considerably lower than the variation observed for D_1, with $s_N = 40$ showing the same total power across the frequency spectrum.

Figure 5-16 Power Spectral Density (PSD) of the cloud width variation as a function of time for different D_2 and different normalized standoff distances s_N.

5.3.3   Nozzle Scalability

The results of the nozzle scalability experiment are shown in Figure 5-17.
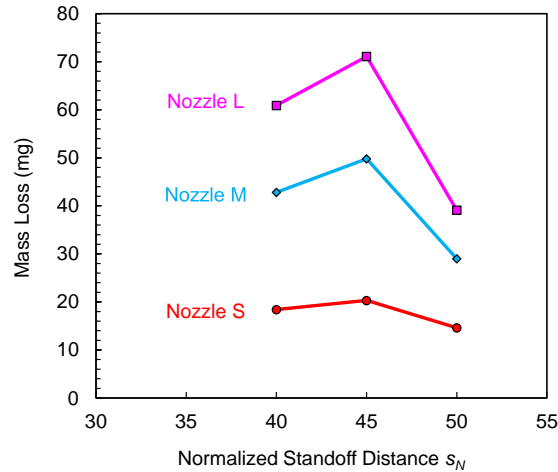
Figure 5-17 Mass loss as a function of normalized standoff distance s_N for different nozzle sizes ($V_{in}=$ 150 m/s, $V_{out}=$ 11.0 m/s, Al 7075-T651, $t_E=$ 30 min).
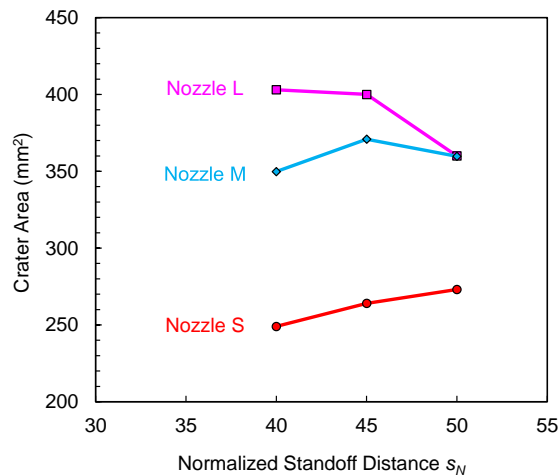
Figure 5-18 Crater area as a function of normalized standoff distance s_N for different nozzle sizes ($V_{in}=$ 150 m/s, $V_{out}=$ 11.0 m/s, Al 7075-T651, $t_E=$ 30 min).

It can be seen that mass loss, and therefore cavitation intensity, increases significantly from nozzle S to nozzle L, with a 59% increase seen between nozzles S and M and a 43% increase between nozzles M and L (where nozzle M is taken to be the baseline nozzle). The erosion crater area, measured as described in [114], is plotted in Figure 5-18. As can be

seen, the crater area at s_N=45 is consistent with mass loss trend, with a large (29%) increase in the crater area seen between nozzles S and M and a relatively small increase (8%) seen between nozzles M and L. This observation suggests that the cavitation intensity improvement seen in Figure 5-17 is due to the increase in nozzle size and therefore due to the quantity of cavitation produced by the nozzle. No conclusions can be drawn on the quality (i.e. impact load of single cavitation events) of the cavitation produced by the two nozzles. Pitting tests were performed in order to evaluate the difference in pit morphology for nozzles *M* and *L*, under the assumption that higher impact loads are necessary to induce deeper pits. A detailed description of the pitting test methodology is offered later in Chapter 6.2. Figure 5-19 shows the pit depth of the first 500 pits obtained under the same flow conditions for nozzle *M* and *L*. As can be seen, the pit depth, and therefore the impact loads, are not affected by the dimension of the nozzle, meaning that the cavitation intensity trends observed in Figure 5-17 can be attributed uniquely to the increase in amount of cavitation produced by nozzle *L*.
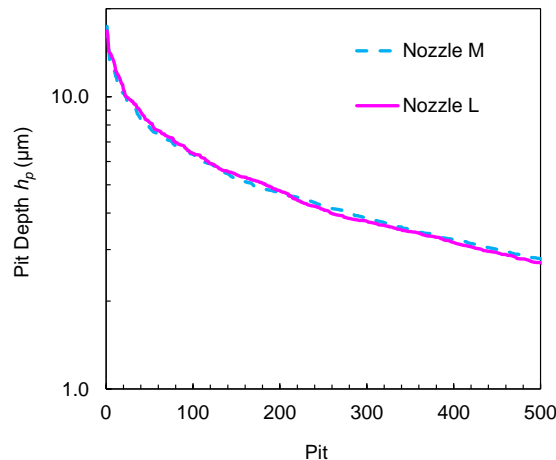
Figure 5-19 Pit depth as a function of nozzle dimension
(V_{in} =150 m/s, V_{out} = 11.0 m/s and s_N = 45, t_E = 5s).

124

Finally, different from the results for D_1 shown in Figure 5-3, the optimum normalized standoff distance s_N is not affected by the scaling of the nozzle dimensions. Having both high pressure nozzles at the same diameter D_1 but with different internal geometries, it is possible that nozzle geometry parameters such as D_0, D_4 and L_1 affect the optimum normalized standoff distance s_N. Further investigation is required to explain the anomaly compared to results shown earlier in Figure 5-3.

The peening time t_P in the peening test for nozzle L was decreased from 18 to 12 min due to the appearance of cavitation erosion marks on the treated strip when peening for the full duration of the experiment. To further investigate this phenomenon, the experiment was repeated and the strip profiles were recorded after 6, 12, and 15 min The corresponding results, given in Figure 5-20, show no further increase in strip curvature when the processing time is increased beyond 12 min This is due to the increase in crater area and cavitation intensity observed in Figure 5-17, causing the strip to saturate at a faster rate compared to the standard nozzle. This also indicates that for the material and flow conditions used in the experiment, the saturation and incubation times are 12 and 18 min, respectively.

125
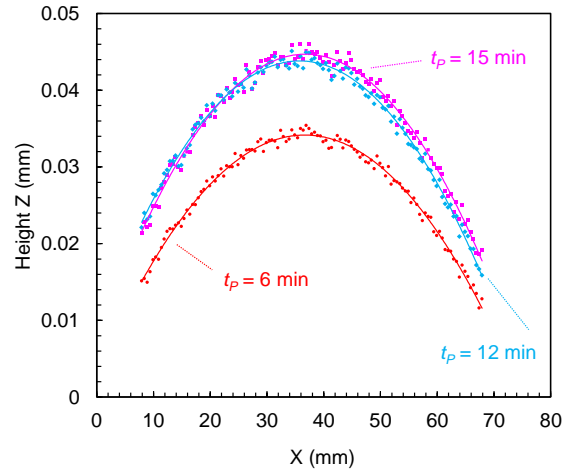
Figure 5-20 Net strip profiles for different processing times t_P (Nozzle L, V_{in}= 150 m/s, V_{out}= 11.0 m/s, s_N = 45, Al7075-T651).
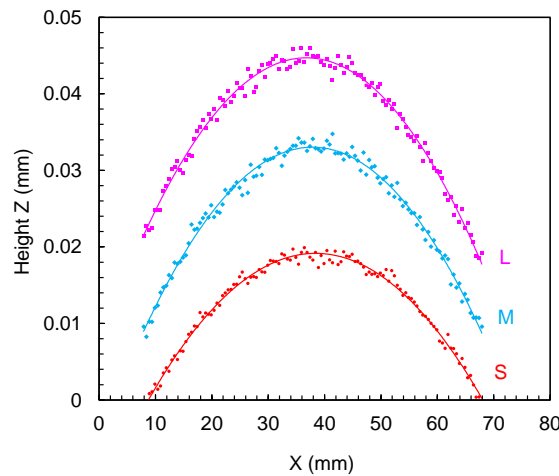
Figure 5-21 Net strip profiles for different nozzle sizes (V_{in}= 150 m/s, V_{out}= 11.0 m/s, s_N = 45, Al 7075-T651).

The net strip height variation was computed for the best case for each nozzle and plotted in Figure 5-21. It can be seen that the strip curvature closely follows the mass loss trends shown in Figure 5-17, once again confirming that the accelerated erosion and strip curvature tests yield consistent results when performed on the same material and can both

126

be used to characterize the flow. Remarkably, nozzle L shows a 33% increase in the net strip height compared to the standard nozzle M, which, when combined with the reduction in processing time required to achieve it, represents a considerable improvement over the reference nozzle M used in this study and in the authors earlier work [114]. Figure 5-22 summarizes the percentage change in the measured process responses for the S and L nozzles relative to the reference nozzle (M).
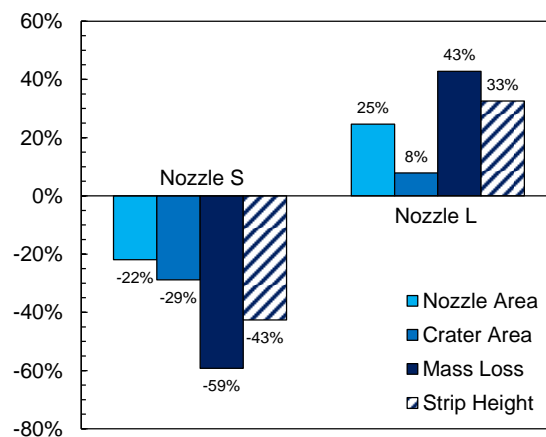
Figure 5-22 Comparison of nozzles S, M and L with nozzle M used as reference (V_{in}= 150 m/s, V_{out}= 11.0 m/s, s_N = 45, Al 7075-T651, refer to Table 5-5 for processing time t_P).

The through-thickness residual stresses measured in the tests performed with nozzles M and L are shown in Figure 5-23. For comparison, shot peening results for 7075-T651 from the literature are also presented. In particular, Benedetti et al. [33] employed medium sized (~500 µm) ceramic beads to obtain an Almen intensity of 4.5A, while Grum et al. [145] employed medium sized (~400 µm) cast steel beads to obtain an Almen intensity of 12A. The corresponding surface roughness results are shown in Figure 5-24.
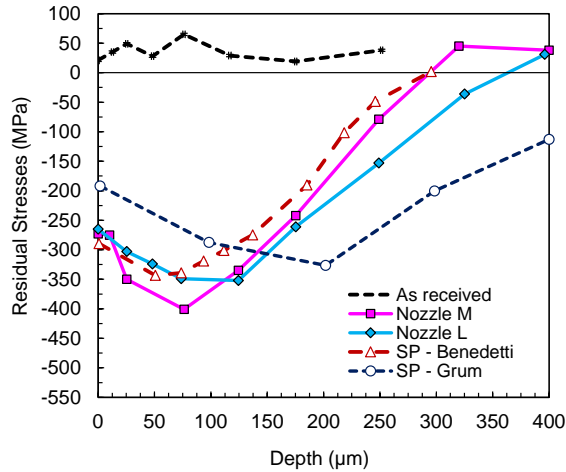
Figure 5-23 Residual stress as a function of depth for the As-Received, Nozzle M, Nozzle L, and Shot Peening (SP) (Benedetti 2009, Grum 2010) conditions.
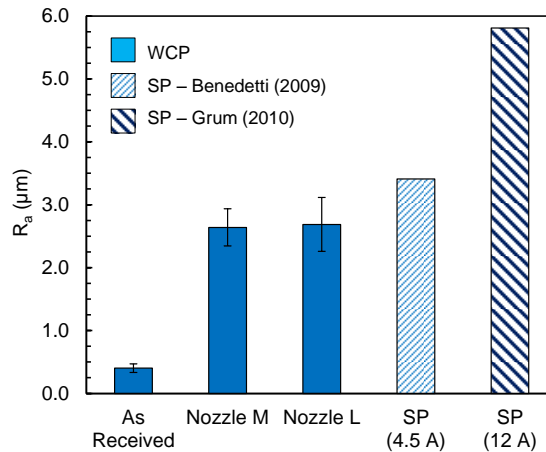
Figure 5-24 Surface roughness R_a for the As-Received, Nozzle M, Nozzle L and Shot Peened (SP) conditions (Almen intensity reported for the SP cases).

The results show that water cavitation peening yields higher compressive residual stresses and lower surface roughness. Nozzles M and L generated the largest compressive residual stresses of -401 and -352 MPa, respectively. These results do not capture the strip profile trends shown in Figure 5-21, but it must be noted that while strip height tests

128

describe the overall effect of the WCP process on the entirety of the strip surface, residual stresses are the results of a localized X-ray diffraction measurements performed at the center of the strip. Interestingly, a study conducted by Soyama et al. [15] showed that the surface residual stresses in water cavitation peened SUS304 stainless steel decrease after reaching a maximum because of prolonged exposure to the cavitating flow [15]. These results are particularly significant because they occur when no measurable mass loss is observed, meaning that the residual stresses could be partially neutralized by the cavitating flow before the onset of measurable erosion. Future work will investigate the effect of peening time t_P on the surface residual stresses in order to clarify this behavior.

129
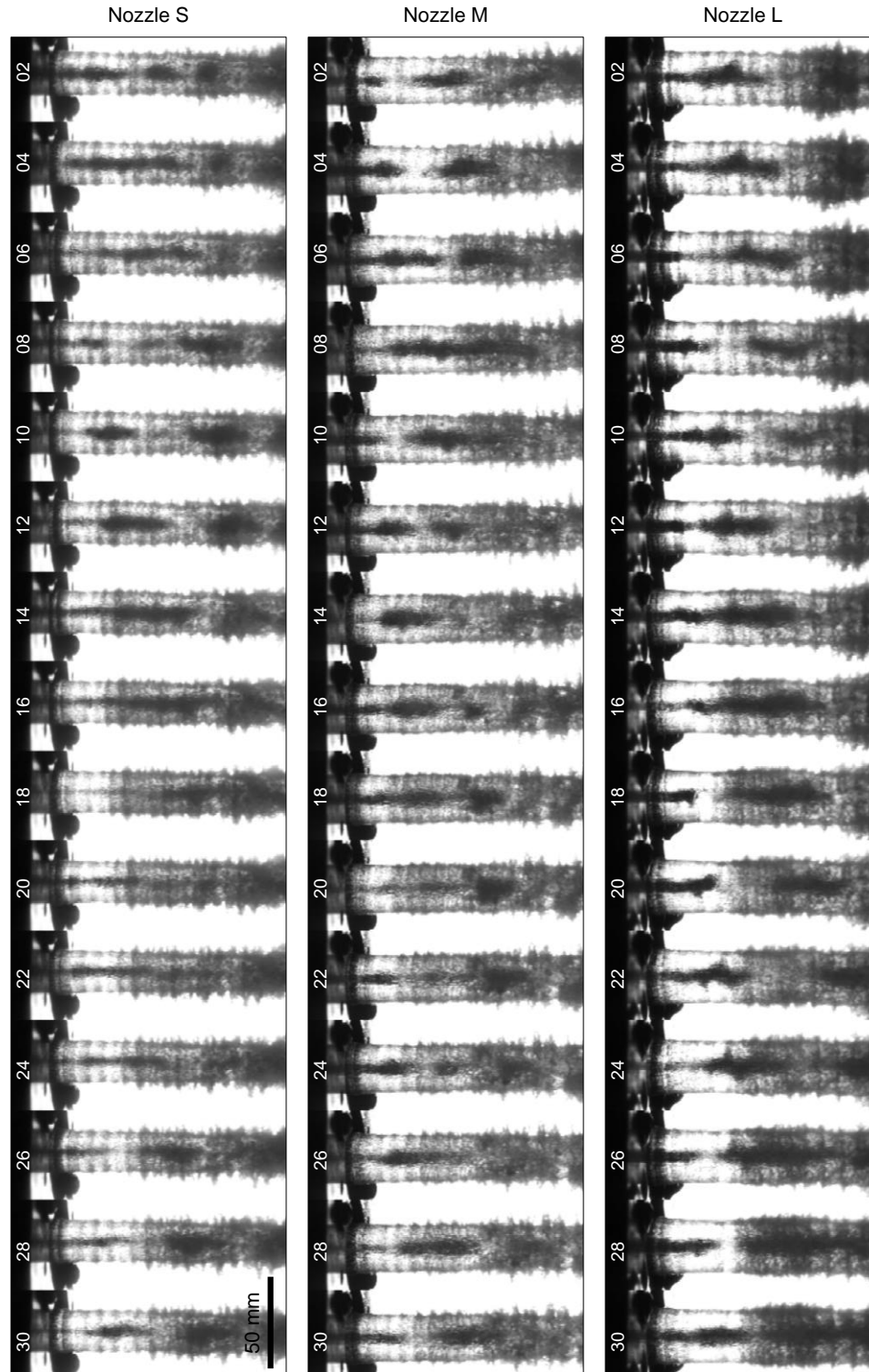
Figure 5-25 Sequence of 15 images of the cavitating flow for different nozzle sizes (constant D_1: D_0: D_2). This sequence represents every second image of videos captured at 14000 fps; the interval between frames is 143 µs (V_{in}= 150 m/s, V_{out}= 11.0 m/s, frame numbers shown).

High speed imaging frames and the average maximum cloud width are shown in Figure 5-25 and Figure 5-26, respectively. As expected, the average maximum cloud width increases with nozzle size, showing a good correlation with the erosion test results shown earlier in Figure 5-17 (e.g. maximum cloud width for nozzle L at $s_N = 40$ is larger than the maximum cloud width for nozzle M at $s_N = 45$). Results for nozzle S are not reported as once again the interference of the wavy pattern at short standoff distances causes the cloud width to be consistently overestimated.
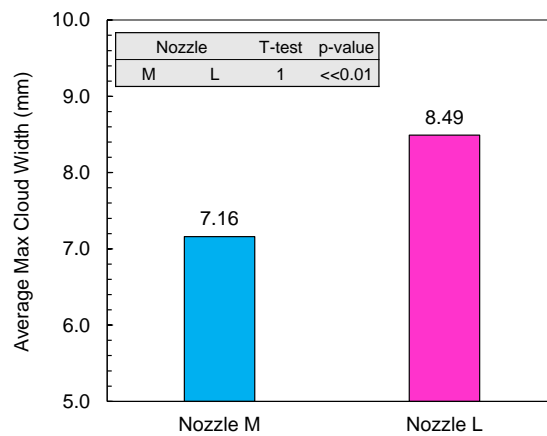
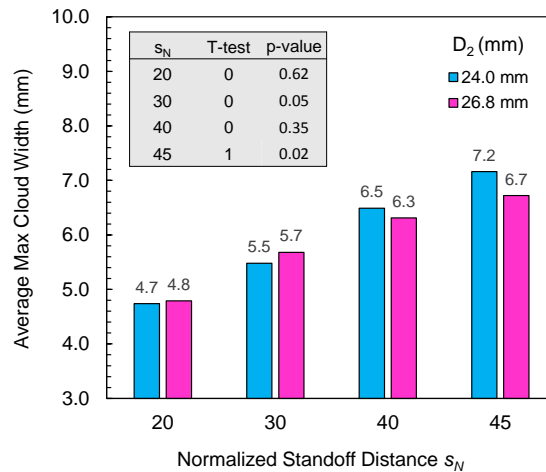**Figure 5-26 Average maximum cloud width for nozzles M and L at different standoff distances s_N.**

The PSD plot for the scalability study is shown in Figure 5-27. A remarkable increase in the overall power content is observed between the two nozzles, while the transition from the 2 kHz peak for $s_N=20$ to the lower frequencies is more pronounced for nozzle L.
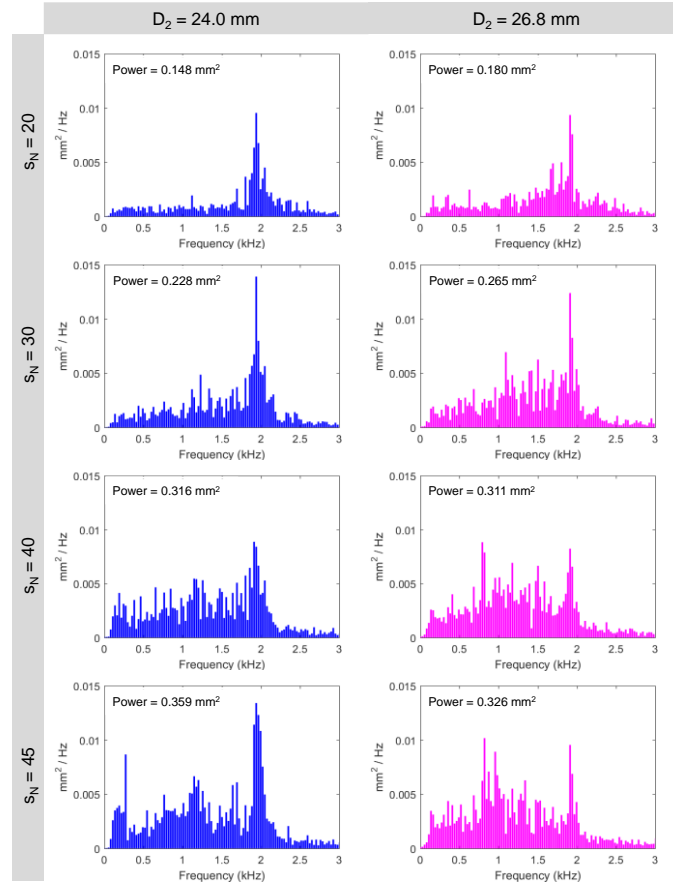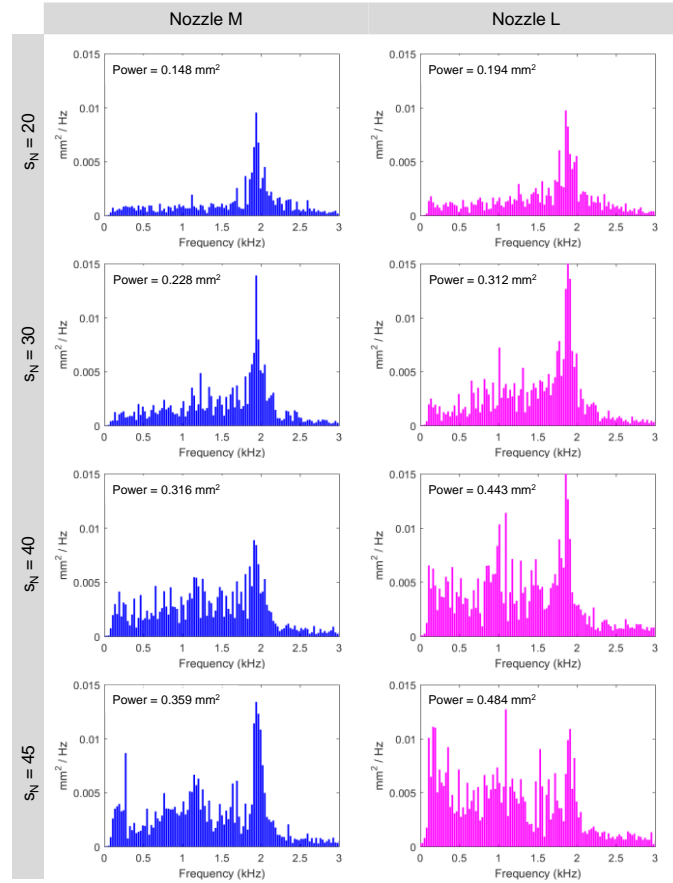
Figure 5-27 Power Spectral Density (PSD) of the cloud width variation as a function of time for nozzles M and L at different normalized standoff distances s_N.

5.3.4 Effect of Nozzle Offset

Figure 5-28 shows the results of accelerated erosion tests for different standoff distances s_N at h=4. Despite the nozzle offset, s_N=45 remains the standoff distance that yields the highest cavitation intensity, as seen for the reference case of h=0. Consequently, the standoff distance s_N=45 is used in the subsequent investigation of the effect of h on cavitation intensity. Figure 5-29 shows the mass loss as a function of exposure time for the flow conditions listed in Table 5-3. The case *a* (h=0, reference Q_{out}, V_{out}) refers to the standard nozzle configuration in Table 5-1 with D_2=D_{2H}, where D_{2H} is the outer nozzle diameter of the cross section at a distance H from the nozzle outlet. In this configuration,

132

the outer flow rate of $Q_{out} = 0.214$ m^3/min generates an outer flow velocity $V_{out} = 11$ m/s, and the results shown in Figure 5-29 for this configuration are the same as those previously reported in Figure 5-3, Figure 5-9, and Figure 5-17. Case b (h=4, constant Q_{out}) refers to the condition where the nozzle offset is h=4 and the flow rate is $Q_{out} = 0.214$ m^3/min. With the flow rate constant and $D_{2H} > D_2$, the outer flow velocity at the section H is reduced to $V_{out} = 9.1$ m/s. Case c (h=4, constant V_{out}) refers to the case where the nozzle offset is h=4 and the outer flow rate Q_{out} is increased to maintain the outer flow velocity V_{out} =11 m/s. The results clearly show an improvement in cavitation intensity for h=4 when the outer flow velocity V_{out} relative to the cross section identified by the inner nozzle is constant, while the cavitation intensity is considerably less when the flow rate is constant and not adjusted for the new nozzle configuration. This finding could explain the dramatic variation in mass loss reported by Vijay et al., where the flow parameters optimized for h=4 were not adjusted to compensate for the variation in nozzle size.
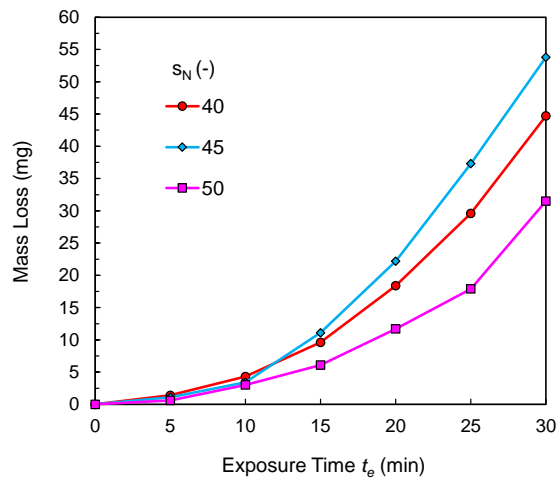
Figure 5-28 Mass loss as a function of exposure time t_E for different standoff distances s_N at h=4 (V_{in}= 150 m/s, V_{out}= 11.0 m/s, Al 7075-T651).

133
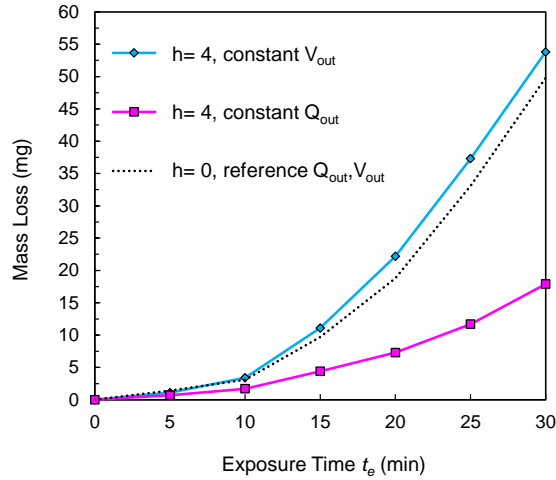
Figure 5-29 Mass loss as a function of exposure time t_E at different flow conditions (V_{in}= 150 m/s, s_N = 45, Al 7075-T651, other parameters reported in Table 5-3).

Table 5-6 Nozzle and flow conditions for the experiments reported in Figure 5-29.

#	h (-)	D_1 (mm)	H (mm)	D_2 (mm)	D_{2H} (mm)	Q_{out} x10^{-3} (m^3/s)	V_{out} (m/s)
(a)	0	0.85	0	24.0	24.0	3.56	11.0
(b)	4	0.85	3.4	24.0	25.8	3.56	9.1
(c)	4	0.85	3.4	24.0	25.8	5.19	11.0

The third experiment was conducted to identify the optimum outer flow velocity at $h \neq$ 0 and to confirm if the results reported in [114] are valid for a different nozzle configuration. Erosion tests were conducted at h=4 with the outer flow velocity varying between 9.1 and 12.5 m/s. Remarkably, Figure 5-30 shows that the cavitation intensity is

134

once again maximum at $V_{out} = 11$ m/s, which was obtained by adjusting the outer flow rate to compensate for variation in the nozzle diameter D_{2H}.

Finally, the effect of nozzle offset was investigated for $V_{in}= 150$ m/s, $V_{out}= 11$ m/s and $s_N = 45$, and the results are shown in Figure 5-31. The cavitation intensity increases when going from $h=0$ to $h=4$, but increasing it to $h=7$ is found to be detrimental compared to the baseline case of $h=0$. Interestingly, these results confirm the work of Vijay et al. [22] in terms of the optimum offset condition, although smaller variations are observed as explained previously.
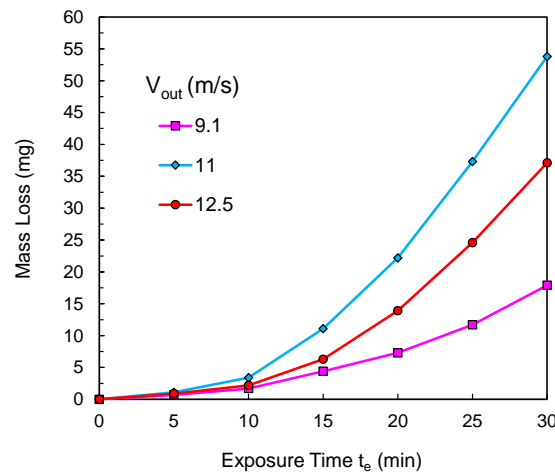
Figure 5-30 Mass loss as a function of exposure time t_E for different outer flow velocities V_{out} ($V_{in}= 150$ m/s, $h=4$, $s_N = 45$, Al 7075-T651).
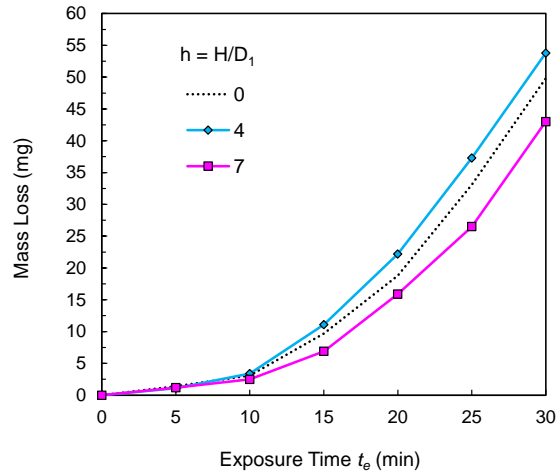
Figure 5-31 Mass loss as a function of exposure time t_E for different offsets h=4 (V_{in}= 150 m/s, V_{out}= 11.0 m/s, s_N = 45, Al 7075-T651).

5.4   Summary

This paper presented an experimental study of the effect of specific nozzle features on the cavitation intensity and peening performance of co-flow water cavitation peening. Accelerated erosion and strip curvature tests were performed and the results analyzed to obtain the following key findings:

1.   Cavitation intensity and strip curvature increase with inner jet diameter D_1, while the relative optimum normalized standoff distance s_N is unaffected. High speed imaging observations show an increase in the average maximum cloud width as a function of D_1.

2.   Cavitation intensity and strip curvature increase with outer jet diameter from D_2 =21.2 mm to D_2 =24 mm, but no further increase is observed for D_2 =26.8 mm. This is believed to be due to the development of a condition approaching the fully submerged jet case for $s_N \leq 45$, where the boundary conditions in the outer flow are

136

no longer affecting the inner jet and where no additional benefits are derived from further increasing the outer flow diameter D_2. High speed imaging observations support the explanation by showing no significant increase in the average maximum cloud width between D_2 =24.0 mm and D_2 =26.8 mm at $s_N = 40 - 45$.

3. Cavitation intensity and strip curvature increase as the nozzle dimensions are dimensions are up while keeping the diameter ratios constant. Nozzle L reduces in peening time t_P required to saturate the strip curvature (and therefore residual stress) compared to nozzle M when peening aluminum 7075-T651.

4. Water cavitation peening produces higher compressive residual stresses and less surface roughening of aluminum 7075-T651 than shot peening. While nozzle M produces the highest residual stresses (401 MPa), nozzle L produces the deepest compressive residual stress extending up to 350 µm below the surface.

5. The normalized offset h=4 maximizes the cavitation intensity and strip curvature. The optimum normalized standoff distance s_N and the outer flow velocity V_{out} are not affected by the change in nozzle geometry.

6. Frequency analysis of the cavitating flows shows a frequency peak around 2 kHz at standoff distance $s_N = 20$. The peak progressively shifts to lower frequencies as the standoff increases from 20 to 45.

CHAPTER 6.   CAVITATION PIT ANALYSIS IN CO-FLOW
WATER CAVITATION PEENING

6.1   Overview

Residual stress is an important aspect at every stage of a manufacturing process involving the thermo-mechanical evolution of the microstructure [146]. Machining [147, 148], welding [149] and deformation processes [150], among others, have been the object of extensive investigation by the research community, in an effort to develop tools and models capable of predicting the residual stress in the part after the material transformation is complete. For peening techniques, the introduction of compressive residual stress is the goal rather than a byproduct of the process, and knowledge of the residual stress is of fundamental importance to the functional performance of the component and for the correct application of the process. The measurement of residual stress is expensive and time consuming [151], and hence the multitude of studies predicting stress levels, with variable degrees of success, produced in the most common peening processes such as shot peening [30, 32] and in laser shot peening [40, 51].

Water cavitation peening (WCP) is a recently developed process that has been shown to produce compressive residual stresses in engineering materials such as A7075-T651 (Figure 5-23) while limiting the surface roughening generally associated with other peening processes [25]. The mechanisms of interaction between the flow and the surface have been an object of interest of the research community for several decades [123, 131, 143, 152]. There are two fundamental ways by which this interaction occurs: shock waves

and re-entrant jets. Shock waves are generated by the rapid collapse of the vapor-filled cavities or cavitation clouds. The stresses imposed on the material surface as a consequence of the collapse have been estimated to be as high as 2 GPa [127, 153, 154], greatly exceeding the yield strength of most common engineering materials. Re-entrant jets are generated upon the collapse of micro-bubbles in close proximity of a solid boundary [127], acting as water-hammer impacts and generating highly localized pressure pulses. Plesset et al. [123] proposed an analytical model of the collapse of a single cavity in the proximity of a solid boundary, predicting jet velocities up to 130 m/s. Tzanakis et al. [17] adopted a different approach and estimated the jet velocity from the analysis of cavitation pits, reporting velocities on the order of V_{jet} = 600 m/s. Independent of the mechanism of interaction, the cavitation phenomenon is characterized by extremely high loads applied over short durations between 5 and 40 µs [127, 137, 155, 156], which can easily cause plastic deformation in common engineering metals. The estimation of cavitation loads has been investigated by several authors, with the main focus being characterization and prediction of cavitation erosion. The pitting rate, coverage time, and incubation time [128] are quantities of great interest in order to estimate cavitation erosion. The same quantities are also relevant to water cavitation peening, since coverage and incubation time are measures of the peening time. Choi et al. [116, 128] investigated the scaling of cavitation pitting and erosion from cavitating jets, and proposed an effective normalization capable of capturing erosion trends for several engineering materials. Franc et al. [129, 130] investigated the effect of material and velocity on cavitation erosion pitting and incubation time for work hardening metals and Chahine et al. [131] proposed a collection of advanced experimental and numerical techniques for the prediction of cavitation erosion. The

estimation of the cavitation collapse impact load has drawn significant attention over the years. Recent developments in sensing technology have allowed several researchers to count the number of impacts of an impinging cavitating cloud and thereby measure the load distributions [132-137, 155]. A different approach, developed by Knapp [138] and recently adopted by Carnelli et al. [139, 140] and Tzanakis et al. [17], employs the material surface as a sensor, and involves conducting stress-strain analysis of individual pits to derive the hydrodynamic impulse pressure of cavitation impact.

As seen in the previous chapters and documented by several other authors [17, 85, 97, 122, 128, 137], cavitation intensity is greatly affected not only by the method used to produce cavitation (e.g. submerged jets, ultrasonic horns, hydrofoils), but for the specific case of submerged jets, cavitation can vary dramatically with flow conditions and nozzle geometry. Accelerated erosion tests and strip curvature tests were successfully employed to characterize the cumulative effect of the cavitating flow on the material response, but limited insight into the effect of flow conditions on the composition of the bubble clouds produced in co-flow WCP can be gained from these studies. In this chapter, pitting tests designed to evaluate the pit morphology produced by the co-flow configuration under different flow conditions are described. Stress-strain analysis is performed on single pits to estimate the stress imposed on the material through a 2D dynamic axisymmetric finite element model designed to study the material behavior under the load conditions experienced in co-flow WCP.

6.2 Materials and Methods

6.2.1 Pitting Tests

Pitting tests were conducted on Aluminium 7075-T651 samples employing the standard nozzle described in Chapter 3. The effect of inner jet velocity, outer jet velocity, and normalized standoff distance were investigated, and the flow conditions used in the tests are summarized in Table 6-1.

Table 6-1 Test condition in pitting tests.

V_{in}	110	130	150	(m/s)
V_{out}	9.5	11.0	12.5	(m/s)
$s_n = s/D_1$	35	45	55	(-)

Samples were mirror finished to a consistent surface roughness of $R_a < 0.05$ µm. A total depth of 500 µm was removed by mechanical polishing to neutralize the effect of the turning process that generated the surface. The samples were exposed to the cavitating flow for a short duration, which was selected based on preliminary experiments where exposure times up to 30 s were tested. Given the extreme aggressiveness of the flow, and in order to limit the overlapping of pits, a duration of 5 s was selected. The pitted samples were measured by means of a Zygo Zegage scanning white light profilometer. For each experiment, four ~ 2000x6800 µm sections, located 90° apart (see Figure 6-1), were surface

141

mapped using the optical profilometer to account for the uneven radial distribution of the cavitation cloud.
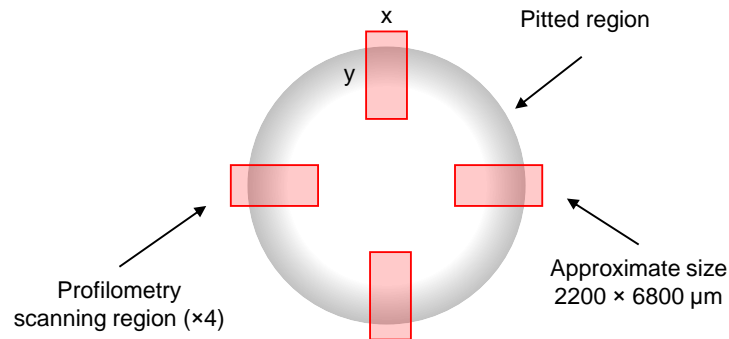
Figure 6-1 Profilometry mapping procedure for the evaluation of cavitation pitting.

The length *y* of the regions scanned by the optical profilometer was selected with the goal to measure the entire cross section of the cavitating ring as seen in Chapter 4, while the width *x* was chosen based on the memory limitation of the instrument. Samples were indexed to maintain consistent alignment between the nozzle and the measured regions of the pitted surface.

6.2.2   Pit Analysis

An example of the result obtained in the pitting test performed at V_{in} = 150 m/s, V_{out} = 11.0 m/s and s_N =45 is shown in Figure 6-2. The profilometer data were subjected to several processing steps to identify and analyze each pit. First, a high pass filter with cutoff wavelength λ_c = 1 mm was applied to the data to remove undesired waviness. Shallow pits were discarded by applying a peak threshold of -0.5 µm across the sample. The threshold was applied consistently and was chosen based on previous work by Choi et al. [128] and

142

Tzanakis et al. [17]. Finally, local minima were identified by means of a 2D min-max algorithm (Figure 6-3).
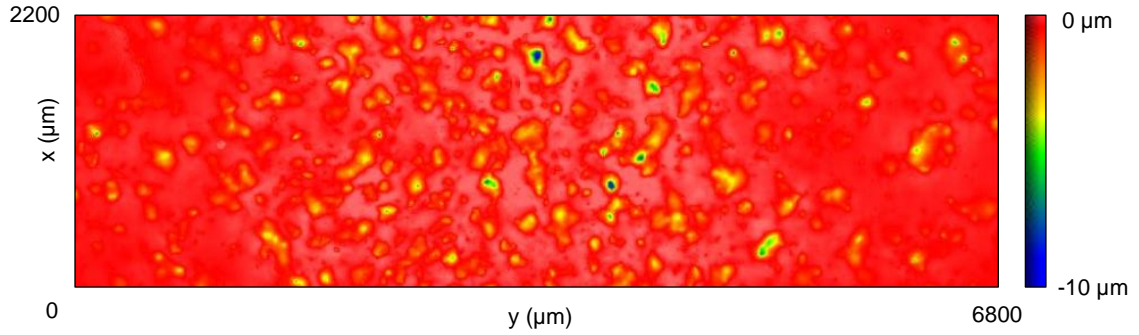
Figure 6-2 Example of pitting test obtained at V_{in} = 150 m/s, V_{out} = 11.0 m/s and s_N =45 (image size: 6800x2200 µm).
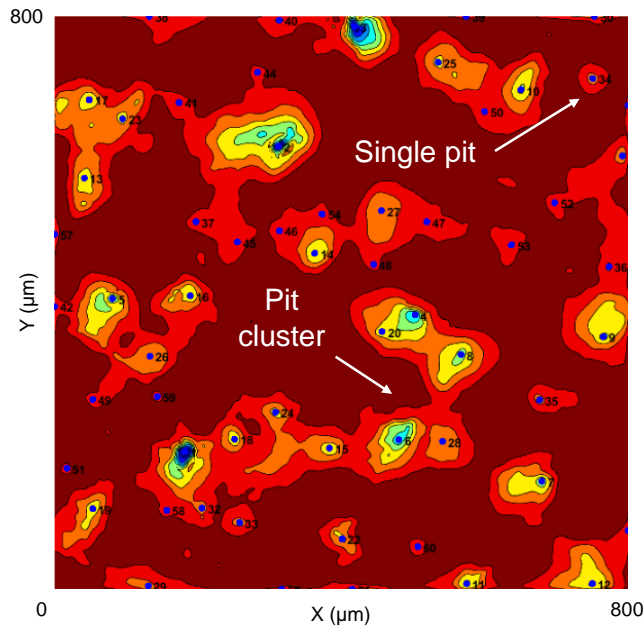
Figure 6-3 Contour plot of pitted surface and local minima (image size: 800x800 µm).

Despite the short duration of the experiment, peaks were found in many cases to be clustered in groups, posing a problem of how to correctly evaluate the volume and surface area of each pit. This behavior has been observed before [17, 127] and it is believed to be due to the dual nature of the flow-surface interaction mechanism, with shock waves released by the collapse of cavitation clouds generating large pitted areas, and with the water-hammer impact generated by re-entrant jets causing the small isolated pits seen in Figure 6-3. In order to have a meaningful characterization of the load applied on the material, each cluster was subdivided into its dominant local minimums and the entire volume/surface area was allocated to each peak by modelling each pit as a spherical cap of volume:

$$V_{cap} = \frac{1}{6}\pi\left(3\frac{d_p^2}{4}h_p + h_p^3\right)$$

Equation Chapter (Next) Section 1(1)

The total volume and surface area of each cluster were partitioned between the different peaks proportionally to ($h_p + h_p^3$), h_p being the depth of the pit as shown in Figure 6-4. Finally, the pit depth h_p and the projected diameter d_p were calculated and are used in the next section to compute the pit strain and pit stress.

6.2.3   *Evaluation of Pit Stress*

The first step in calculating the pit stress is to compute the true strain in the pits whose geometry was established using the procedure described in the previous section. Contact mechanics theory developed for the response of hard materials to spherical nano-

144

indentation was used to characterize the pits generated by cavitation. From the work of Tabor [157] and Francis [158], the indentation (true) stress on a metal surface is equal to:

$$\sigma_{pit} = \frac{1}{\psi} \frac{L_{pit}}{A_c} \tag{2}$$

where σ_{pit} is the true pit stress, L_{pit} is the indentation load, A_c is the projected area of contact, and ψ is a constraint factor equal to 2.87 in plastic regime representing the ratio between the mean contact pressure over the projected area A_c and the representative uniaxial flow stress of the indentation [158]. The uniaxial plastic strain ε_p along the contact edge of the spherical indenter is equal to:

$$\varepsilon_p = 0.2 \frac{h_p d_p}{\left(\dfrac{d_p}{2}\right)^2 + h_p^2} \tag{3}$$

with h_p and d_p being the pit depth and diameter, respectively, as shown in Figure 6-4.
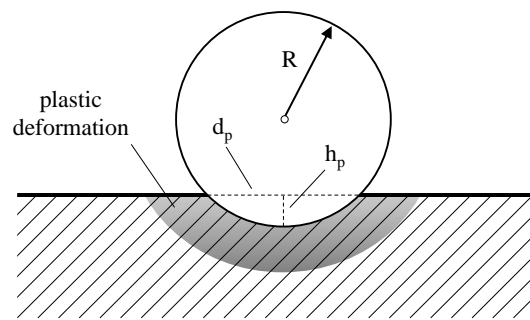
Figure 6-4 Schematic of the spherical cap modeling for the formation of the cavitation pit.

In the case of work-hardening materials such as Aluminum 7075, the stress-strain relationship in the plastic regime can be expressed as:

145

$$\sigma = \sigma_0 \left(\frac{\varepsilon}{\varepsilon_0} \right)^n \tag{4}$$

with σ_0 and ε_0 being the reference stress and strain at the yield point. Equation (4) does not take into consideration the strain rate effect generally associated with the application of extremely rapid loads, and needs to be accounted in the material constitutive model. Given that the cavitation phenomena are characterized by high loads and durations on the order of ~20 µs, strain rates in the range of 10^3 -10^5 s^{-1} [139, 159] are expected in the material as a consequence of the cavitation-surface interaction. In order to account for such high strain rates, the well-established Johnson-Cook model [160] is introduced in equation (5), and a strain rate $\dot{\varepsilon}_p = 1 \times 10^4$ s^{-1} is adopted.

$$\sigma = \left(A + B \varepsilon_p^n \right) \left(1 + C \ln \frac{\dot{\varepsilon}_p}{\dot{\varepsilon}_0} \right) \tag{5}$$

The material constants in equation (5) were developed by Brar et al. [161] and are summarized in Table 6-2.

Table 6-2 Johnson-Cook parameters for Al 7075-T651.

A	B	n	C	$\dot{\varepsilon}_0$
527	575	0.72	0.017	1
MPa	MPa	(-)	(-)	1/s

Finally, the pit load was calculated from the equation:

146

$$L_{pit} = \sigma_{pit} A_c \psi \tag{6}$$

where L_{pit} is the force exerted by the indenter on the pitted surface, σ_{pit} is the pit stress, A_c is the projected area of contact, and ψ is equal to 2.87 as fully plastic deformation is expected during the process.

6.2.4 FEM Model Details

The response to the load exerted by cavitation was investigated through a dynamic, 2D axisymmetric model developed using the finite element code ABAQUS/Explicit. The purpose of the model was to obtain an estimate of the longitudinal residual stress introduced in the material surface by the cavitation phenomenon using the information collected through the stress-strain analysis described in the previous sections.

The domain of the model was set considerably larger (500µm x 500µm) than the cavitation impact radius (~ 25-50 µm) to simulate the semi-infinite condition encountered by the flow and to mitigate the stress-wave reflection from the model boundary. Details of the model domain such as mesh size and element type are summarized in Figure 6-5. The material plastic behaviour was characterized by the rate-dependent Johnson-Cook model given by Equation (5), with the constants summarized in Table 6-2. Equation (7) represents the Gaussian distribution used to model the load spatial distribution and amplitude:

$$\sigma(r,t) = \sigma_p \, e^{\left(-\left(\frac{2r}{d_c}\right)^2\right)} e^{\left(-\left(\frac{2(t-t_c)}{t_c}\right)^2\right)} \tag{7}$$

where σ_p is the peak stress magnitude, r is the distance from the axis of symmetry, d_c is the characteristic diameter, t_c is the characteristic time, and t is the time step used in the

147

simulation. The load described in equation (6.7) was centered on the axis of the model ($r = 0$) and completely removed after the characteristic time t_c in order to evaluate the longitudinal residual stresses along the axis of symmetry. Based on the results of the pitting tests summarized in the next section, simulations were conducted using three stress levels σ_p (0.9, 1.2 and 1.5 GPa), two characteristic diameters d_c (25 and 50 µm) and one characteristic time t_c of 20 µs for all the considered cases. Three levels of the peak stress magnitude σ_p are selected based on the results on pit stress σ_{pit} described in the next section, being the stress pit σ_{pit} the flow stress of the material after deformation and representing a lower bound for the expected stress magnitude exerted by the cavitation phenomena upon collapsing onto the rigid surface.
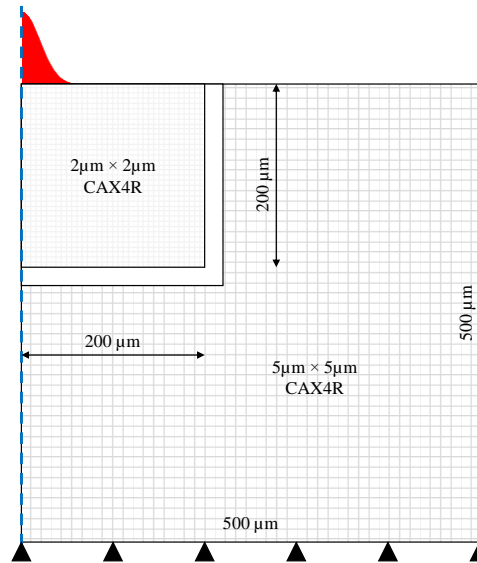
Figure 6-5 2D axisymmetric model used in the simulations.

6.3   Results

6.3.1 *Effect of Inner Jet Velocity on Pitting and Cavitation Impact Loads*

Pitting tests and pit analysis were carried out to investigate the effect of inner jet velocity V_{in} on the pitting of aluminium 7075-T651 samples. Based on the work presented in Chapter 4, three levels were selected for this investigation: V_{in} =150, 130 and 110 m/s, while the other parameters were maintained at the previously determined optimum of V_{out} = 11.0 m/s and s_N = 45. Figure 6-6 shows the experimentally measured coverage as a function of the inner jet velocity. Coverage is defined as the percentage of the area scanned by the profilometer (shown in Figure 6-2) that is covered by pits. The results shown are the average of the four scanned sections shown in Figure 6-1. It can be seen that the coverage tends to increase as the inner jet velocity increases. This is due to the increase in the amount of cavitation generated with V_{in} as reported in Figure 4-26 and also observed in the high speed video analysis.
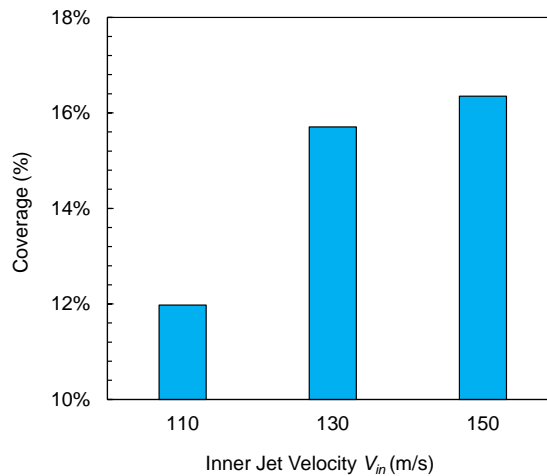
Figure 6-6 Average surface coverage as a function of inner jet velocity V_{in}
(V_{out} = 11.0 m/s and s_N = 45).

The pit diameter and pit depth are plotted in Figure 6-7 in descending order. For each flow condition, between 2200 and 2500 pits were counted, and the first 2200 are

149

presented. The highest inner jet velocity (150 m/s) was found, on average, to yield larger and deeper pits, resulting in higher average loads, as shown in Figure 6-8. No substantial difference can be seen between the inner jet velocities of 110 and 130 m/s. This observation suggests that the difference in cavitation intensity observed in Figure 4-26 for the two velocities is due to the increased amount of cavitation produced by the flow rather than the inherent intensity of the cavitation (pit depth) and that the pitting test results obtained from 5 s of exposure cannot characterize the cumulative effect of the accelerated erosion test, which is characterized by an exposure time of 30 min
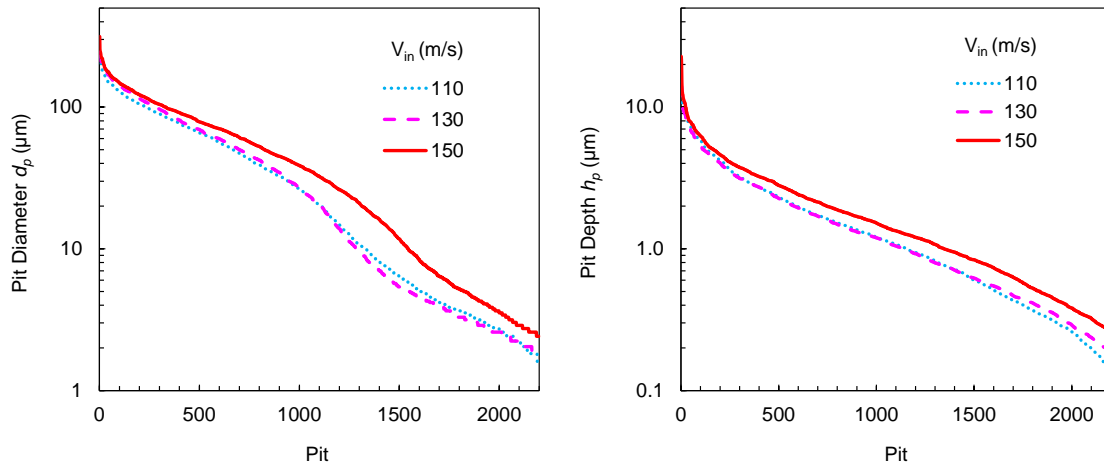
Figure 6-7 Pit diameter and pit depth as a function of inner jet velocity V_{in}
($V_{out} = $ **11.0 m/s and** $s_N = $ **45).**
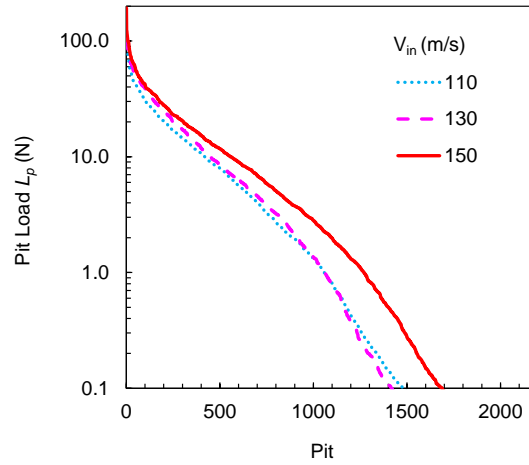
Figure 6-8 Pit load (N) as a function of inner jet velocity V_{in}
($V_{out} = 11.0$ m/s and $s_N = 45$).

151

6.3.2   Effect of Outer Jet Velocity on Pitting and Cavitation Impact Loads

The effect of outer jet velocity was investigated by means of pitting tests and pit analysis. Based on the work presented in Chapter 4, three levels of the outer jet velocity were selected for this investigation: V_{out} =9.5, 11.0 and 12.5 m/s, while other parameters were maintained at V_{in} = 150 m/s and s_N = 45. Figure 6-9 shows the measured coverage as a function of the outer jet velocity. The peak at V_{out} =11.0 m/s is once again explained by the increased cavitation production as a function of V_{out} reported in Figure 4-26 and observed in the high speed image analysis discussed in the same chapter.
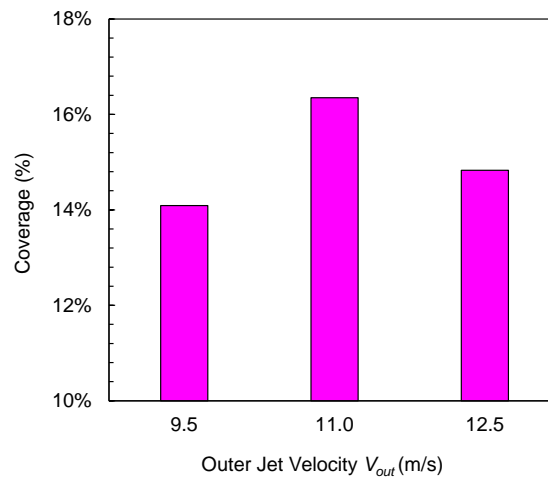
Figure 6-9 Average surface coverage as a function of outer jet velocity V_{out}
(V_{in} = 150 m/s and s_N = 45).

The pit diameter and pit depth as a function of the outer flow velocity are plotted in Figure 6-10. The optimum outer jet velocity V_{out} = 11.0 m/s identified in Chapter 4 yields, on average, larger diameters and deeper pits, leading to a higher average pit load as seen in Figure 6-11. The results are in agreement with the accelerated erosion tests and the strip curvature tests reported in Chapter 4 and summarized in Figure 4-26.

152
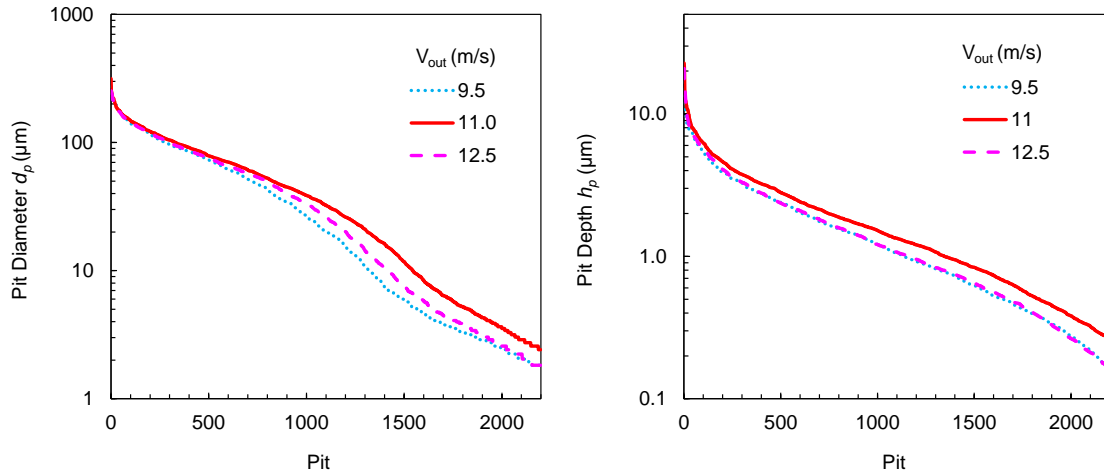
Figure 6-10 Pit diameter and pit depth as a function of outer jet velocity V_{out} ($V_{in} = 150$ m/s and $s_N = 45$).
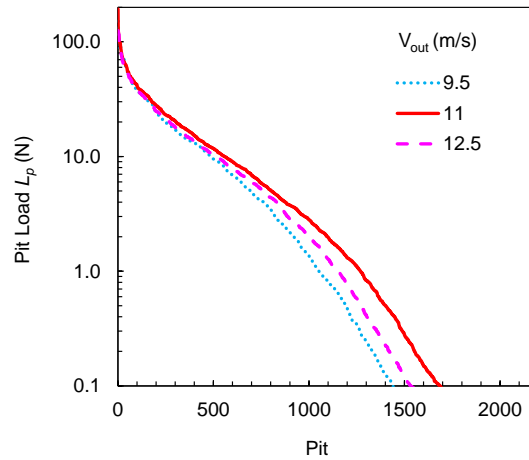
Figure 6-11 Pit load (N) as a function of outer jet velocity V_{out} ($V_{in} = 150$ m/s and $s_N = 45$).

6.3.3 Effect of Standoff Distance on Pitting and Cavitation Impact Loads

The effect of normalized standoff distance was investigated by means of pitting tests and pit analysis. Based on previous work, three levels were selected for this investigation: $s_N = 35$, 45 and 55, while the other parameters were maintained at $V_{in} = 150$

153

m/s and V_{out} = 11.0 m/s. The average surface coverage obtained is shown in Figure 6-12. Once again, the surface coverage confirms the results reported in Chapter 4 and summarized in Figure 4-18, with s_N = 45 reporting the highest average surface coverage and the largest crater surface area.
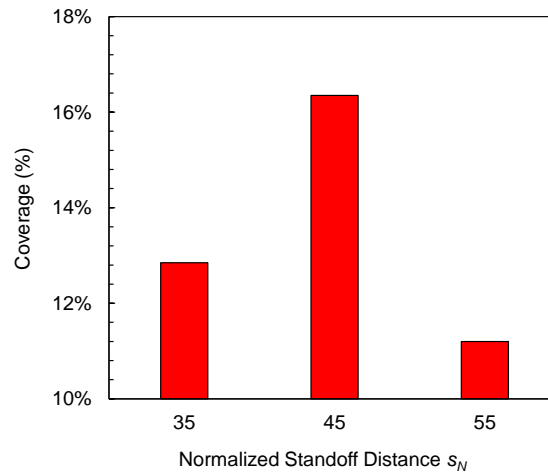
Figure 6-12 Average surface coverage as a function of normalized standoff distance s_N **(V_{in} = 150 m/s and V_{out} = 11.0 m/s).**

Figure 6-13 shows the pit diameter and pit depth as a function of the normalized standoff distance. The optimum standoff distance identified in Chapter 4 generates, on average, larger diameters and deeper pits, leading to an average higher pit load as seen in Figure 6-14. The results are in agreement with the accelerated erosion tests reported in Figure 4-24.

154
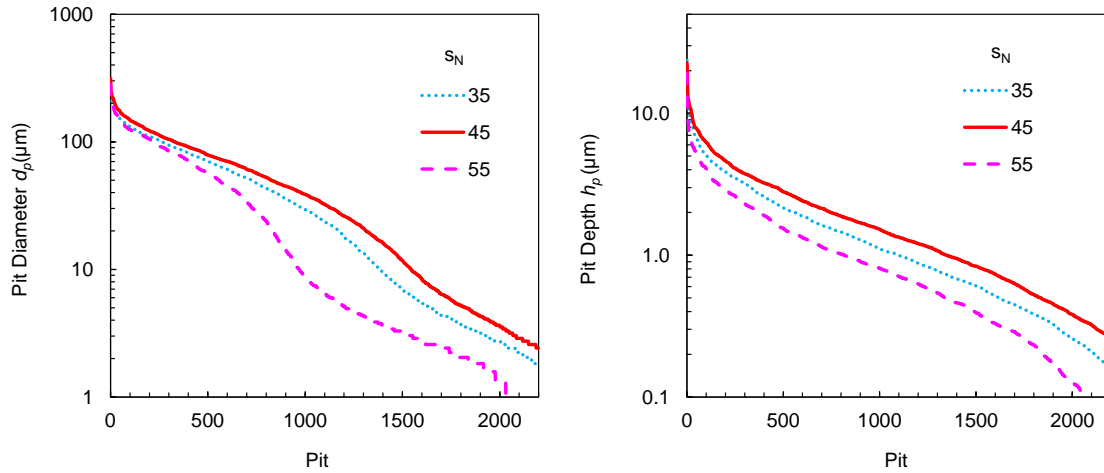
Figure 6-13 Pit diameter and pit depth as a function of normalized standoff distance s_N (V_{in} = 150 m/s and V_{out} = 11.0 m/s).
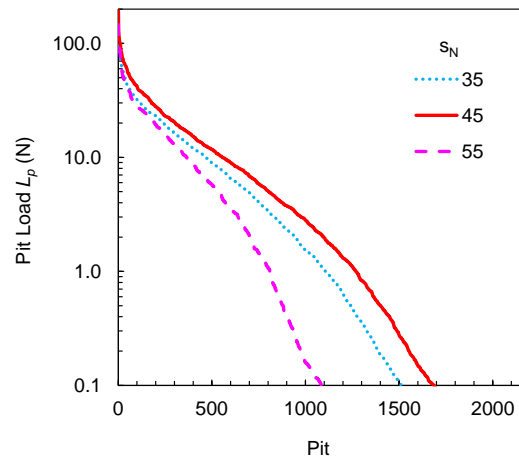
Figure 6-14 Pit load (N) as a function normalized standoff distance s_N
(V_{in} = 150 m/s and V_{out} = 11.0 m/s).

155

6.3.4.1   <u>Input to the FEM Model</u>

The data collected from the pitting tests were adopted as a starting point for the finite element model and used to guide the selection of the parameters used in the model.

The measured pit stress distribution for all the pits generated by the optimum peening conditions (V_{in} = 150 m/s, V_{out} = 11.0 m/s and s_N = 45) is reported in Figure 6-15. As can be seen, stresses up to 1.3 GPa are recorded, with a dominant peak at ~ 0.9 GPa and a secondary peak at ~ 1.15 GPa. These values are in agreement with stress levels derived by other authors [127, 153, 154].
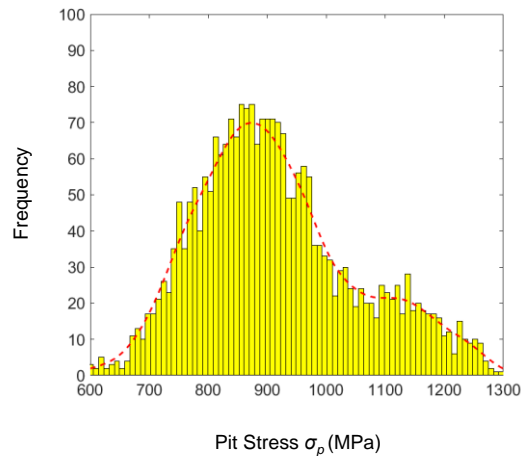
Figure 6-15 Pit stress σ_p distribution
(Vin = 150 m/s, Vout = 11.0 m/s and s_N = 45).

The peaks at ~0.9 GPa and ~1.15 GPa in Figure 6-15 were further analysed by subdividing the pit population in two groups. The first group was characterized by a pit stress of 0.8<σ_p<1.0 GPa, while the second group was characterized by a pit stress of 1.0<σ_p<1.2 GPa. The distribution of the pit diameter d_p was plotted for both groups, and can be seen

156

in Figure 6-16. The average pit diameter-to-depth d_p/h_p ratio was also computed for each subgroup and is reported in the same figure.
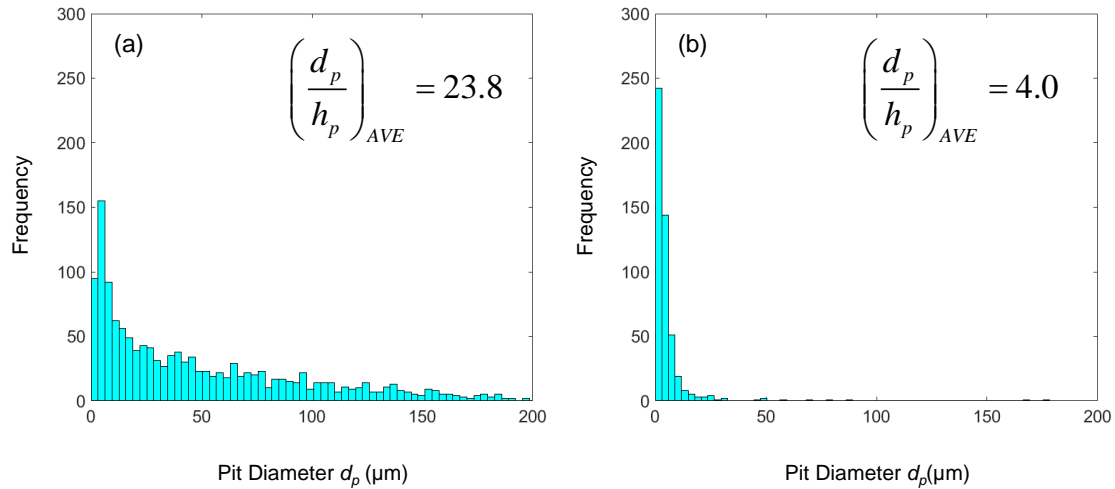
Figure 6-16 Diameter d_p distribution for pits having (a) 0.8<σ_p<1.0 GPa and (b) 1.0<σ_p<1.2 GPa.

Interestingly, the group with 0.8<σ_p<1.0 GPa (Figure 6-16a) has a larger d_p/h_p ratio and a population composed of pit diameters up to 200 µm, while the group with 1.0<σ_p<1.2 GPa has a small average d_p/h_p ratio and a population composed primarily of pits under 20 µm in diameter. Evidence reported elsewhere [17, 127] suggests that this behavior should be attributed to the dual nature of the flow-surface interaction mechanism, with shock waves generating large and shallow pits and reentrant-jets generating smaller needle-like craters. Because the maximum compressive residual stress obtained in WCP depends on the highest impact stress achieved in the process [15], it can be concluded that re-entrant jets are the driving mechanism in the both the introduction of residual stress in WCP and the crack initiation phenomenon leading eventually to cavitation erosion.

In light of these results, three pit stress σ_p values (0.9, 1.2 and 1.5 GPa) and two characteristic impact diameters d_c (25 and 50 µm) were selected.

157

6.3.4.2   Simulations Results

Longitudinal residual stresses as a function of stress amplitude σ_p for a single impact of diameters d_c = 25 µm are reported in Figure 6-17. Residual stresses along the axis of symmetry of the model, down to a depth of 100 µm below the material surface, are shown. Interestingly, the stress magnitude of σ_p =0.9 GPa reports no residual stress in the material, suggesting that the stress magnitude is severely underestimated by the model proposed in section 6.2.3. Higher stress amplitudes such as 1.2 and 1.5 GPa show increasing longitudinal residual stresses, reaching a maximum of ~ -173 MPa at ~10 µm below the surface.
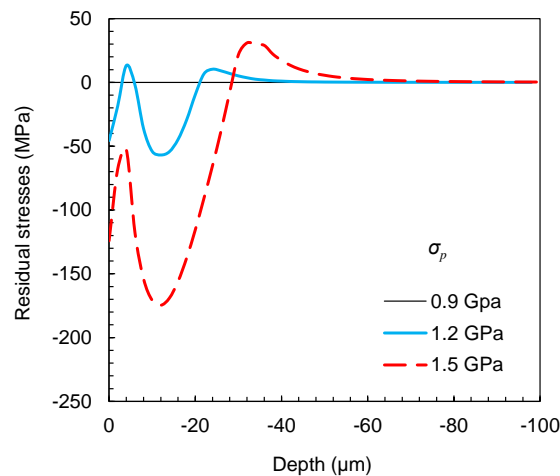
Figure 6-17 Longitudinal residual stress profile at the centerline as a function of stress amplitude σ_p (r = 0, d_c = 25 µm, t_c = 20 µs, single impact).

A marginal increase in residual stress is observed when the characteristic diameter d_p is increased to 50 µm, as seen in Figure 6-18. Once again the stress magnitude of σ_p =0.9

www.manaraa.com

GPa reports no residual stress in the material, while $\sigma_p = 1.5$ GPa results in a residual stress of about -185 MPa at ~20 µm below the surface.
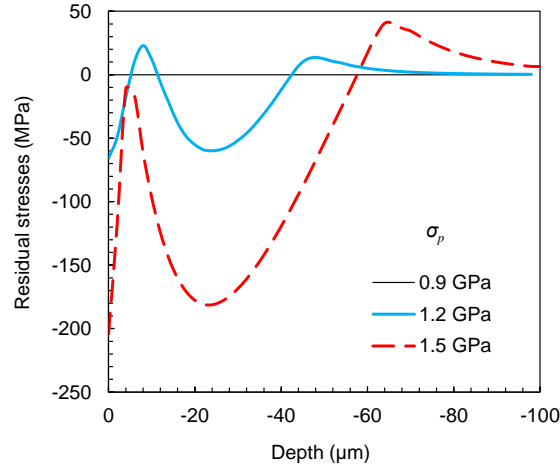
Figure 6-18 Longitudinal residual stress profile at the centerline as a function of stress amplitude σ_p ($r = 0$, $d_c = 50$ µm, $t_c = 20$ µs, single impact).

A direct comparison in terms of the characteristic diameter d_c is shown in Figure 6-19 and Figure 6-20 for two different load amplitudes. In both cases, the residual stress level is observed to remain fairly constant, while the depth profile is observed to become deeper as the impact diameter d_c increases. This observation suggests that re-entrant jets, which are characterized by small impact diameters, can produce higher compressive residual stresses, while the shock waves generated by wide cavitation clouds have the potential to reach higher depths in the material.

159
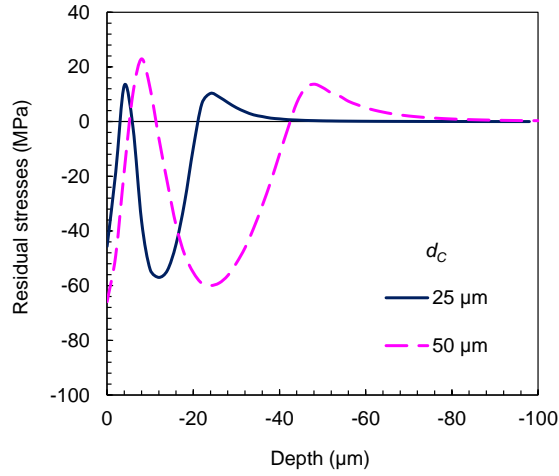
Figure 6-19 Longitudinal residual stress profile at the centerline as a function of characteristic impact diameter d_c ($r = 0$, $\sigma_p = 1.2$ GPa, $t_c = 20$ μs, single impact).
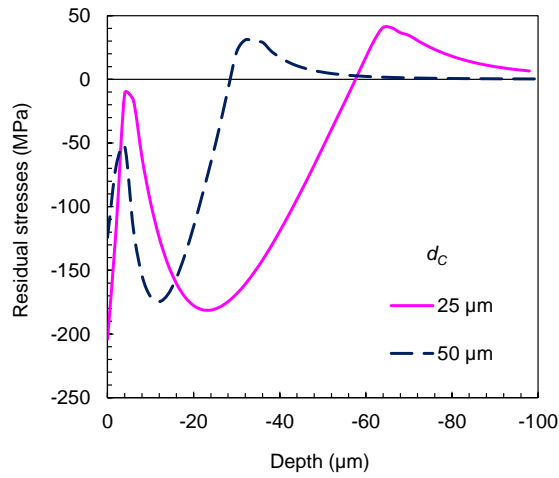
Figure 6-20 Longitudinal residual stress profile at the centerline as a function of characteristic impact diameter d_c ($r = 0$, $\sigma_p = 1.5$ GPa, $t_c = 20$ μs, single impact).

160

Finally, the evolution of residual stress was investigated by simulating the application of two consecutive distinct loads, with both pulses possessing the same Gaussian distribution described in Equation (6.7). Interestingly, for the case of $d_c. = 25\ \mu m$ (Figure 6-21) no substantial change in the residual stress profile was recorded after the second load was applied, while the case $d_c = 50\ \mu m$ registered a dramatic increase in compressive residual stresses reporting a maximum value (~650 MPa) above the yield strength of the material (~ 568 MPa).
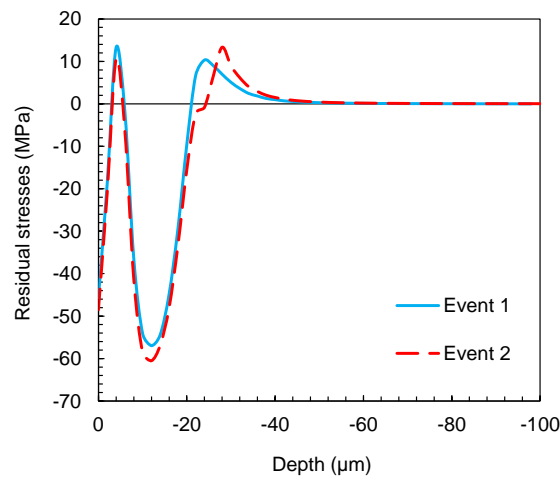
Figure 6-21 Longitudinal residual stress profile history at the centerline after two consecutive impacts ($r = 0$, $d_c = 25\ \mu m$, $\sigma_p = 1.2$ GPa, $t_c = 20\ \mu s$).

161
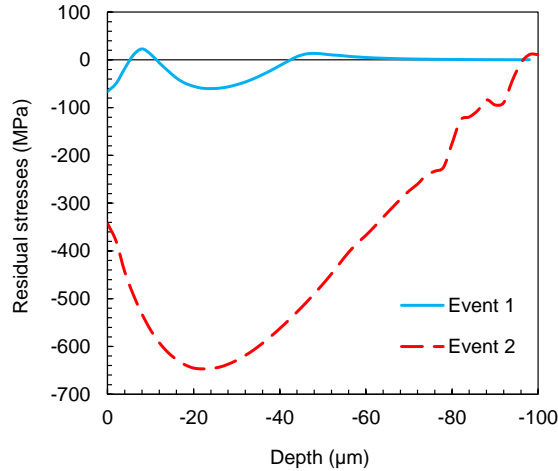
Figure 6-22 Longitudinal residual stress profile history at the centerline after two consecutive impacts ($r = 0$, $d_c = 50$ μm, $\sigma_p = 1.2$ GPa, $t_c = 20$ μs).
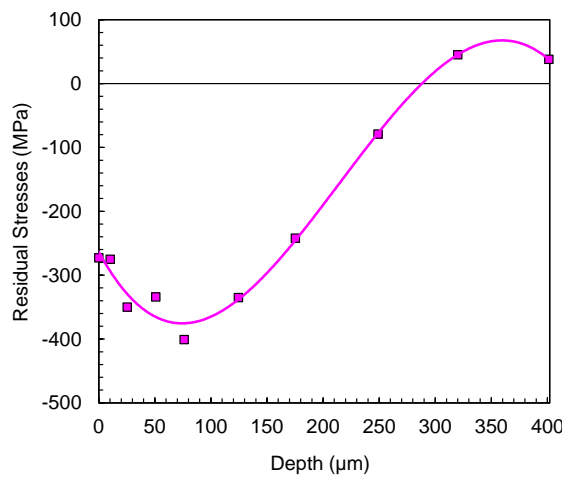
Figure 6-23 Longitudinal residual stress profile in WCP
($V_{in} = 150$ m/s, $V_{out} = 11.0$ m/s and $s_N = 45$, $t_p = 30$ min)

A direct comparison of the results obtained for the case of a single cavitation event and the cumulative measured residual stresses shown in Figure 6-23 can be made only after recognizing the following limitations of the model proposed in this chapter relative to the physical process:

1. The WCP is a cumulative process characterized by an estimated ~ 900 events per unit area (mm^2) per second over the exposure time of t_e ~ 30 s used in the experimental case shown in Figure 6-23.

2. The strain rate assumed in the simulation (10^4 s^{-1}) belongs to rather large range estimated for the cavitation phenomena (10^3~10^5 s^{-1}) that can drastically impact the material response to impulsive loads.

3. The impact load diameter (~25 µm) is potentially of the same order of magnitude as the grain size of common engineering materials.

4. The stress-strain analysis used in this chapter is based on nano-indentation mechanics employing an infinitely rigid indenter.

Useful insights into the different interaction mechanisms was obtained by the simulation of the material response to a single impact. The simulations showed promising results for the estimation of residual stresses in WCP but require further development in order to fully understand the potential and limitations of this approach.

6.4 Summary

This chapter presented a study of the surface pitting generated by WCP. The effect of several flow conditions were investigated and impulsive loads estimated trough stress-strain analysis of individual pits produced by cavitation. A numerical model of the material behavior while undergoing a single cavitation impact was presented and the results analyzed to obtain the following key findings:

1. Pitting tests confirm the results obtained in previous chapters which indicated higher cavitation loads for the optimum flow conditions of $V_{in} = 150$ m/s, $V_{out} = 11.0$ m/s and $s_N = 45$.

2. The pit stress distribution reported two peaks of different stress intensities. The two peaks can be attributed to different flow-material interaction mechanisms. The large cluster of pit diameters and lower impact loads are attributed to the shock wave mechanism while small, isolated impact diameters and higher impact loads are attributed to the effect of re-entrant jets.

3. The simulations suggest that an increase in the impact load σ_p beyond a critical value can dramatically increase the magnitude of residual stresses, while little influence is observed on the depth at which such peaks occur.

4. The impact diameter d_c has a major effect on the depth of penetration of the residual stress, suggesting that the shock wave-generated large pits determine the residual stress state penetration in the material surface.

CHAPTER 7.   CONCLUSIONS

This chapter summarizes the main conclusions of this thesis and suggest related area of further investigation.

7.1   Main Conclusions

7.1.1   Flow Characterization in Co-Flow WCP

The chapter presented an experimental study of the effect of flow velocities in co-flow type water cavitation jet peening. First, cavitation aggressiveness was assessed by means of accelerated erosion tests on soft aluminum Al 1100-O and Al 7075-T6. Second, peening performance was investigated through strip curvature tests on Al 7075-T6 samples for a selected subset of flow conditions. From the analysis of the results, the following conclusions can be drawn:

1.   Two distinct regimes of operation exist in co-flow water cavitation peening, namely the *ring regime* and the *center regime*. The ring regime displays high mass loss distributed in a large ring-shaped region, while the center regime displays a low mass loss concentrated at the center of the cavitating jet. Despite the center regime showing a higher mass loss per unit area, the ring regime yielded the best performance in terms of the saturated strip curvature and therefore peening capability. The optimum peening conditions for the nozzle used in this study were found to be V_{in} =150m/s, V_{out} =11.0m/s and s_n=45 for the ring regime and V_{in} =150m/s, V_{out} =5.0 m/s and s_n=45 for the center regime. It is the author's belief that the performance of the center regime can be greatly enhanced

by increasing the inner jet velocity through suitable redesign of the nozzle, as already shown by other authors [22]

2. The crater area in the accelerated erosion test (Al1100-O) increases with the inner jet velocity V_{in} and peaks at $9.5 < V_{out} < 12.5$ m/s and $40 < s_n < 50$.

3. For the nozzle used in this study, the outer jet velocity V_{out} that maximizes erosion and peening capability is independent of the inner jet velocity V_{in} and equal to $V_{out} = 11.0$ m/s. This value is also found to maximize the crater area, and is believed to represent the equilibrium point between two competing phenomena, namely cavitation generation, which is proportional to ($V_{in} - V_{out}$) and cavitation transportation, which is proportional to V_{out}.

4. The optimum normalized standoff distance is equal to $40 \leq s_n \leq 45$ for all the jet velocity combinations considered in this study. Major changes in optimum s_n are expected if the nozzle geometry is varied [142]

5. Erosion tests on Al1100-O lead to inaccurate conclusions regarding the influence of the inner and outer jet velocities on the peening performance of Al 7075-T6 strips. Moreover, higher variability is observed, which is believed to be inherent in the erosion process.

6. Erosion tests on Al 7075-T6 are found to capture the influence of different flow parameters on the peening capability for the same material. Moreover, both erosion tests and strip curvature tests on Al 7075-T6 show very good repeatability, which makes them more suitable for assessment of peening performance.

7. Surface roughness was found to increase during peening (up to 2.2 µm), and was observed to closely follow the strip curvature trends.

8. High speed video observations of the cavitation flow confirm the trends observed in the accelerated erosion tests showing an increase in cloud size as a function of inner jet velocity V_{in}. Moreover, cloud analysis showed the outer flow velocity $V_{out} = 11.0$ m/s being the optimum trade-off between cloud size and the amount of generated clouds by the flow. Finally, the spectral analysis of the cloud diameter evolution confirmed the results from the accelerated erosion tests showing the highest power content for the optimum case $V_{in} = 150$m/s, $V_{out} = 11.0$m/s and $s_n = 45$.

7.1.2 *Nozzle Characterization in Co-Flow WCP*

This chapter presented an experimental study of the effect of specific nozzle features on the cavitation intensity and peening performance of co-flow water cavitation peening. Accelerated erosion and strip curvature tests were performed and the results analyzed to obtain the following key findings:

9. Cavitation intensity and strip curvature increase with inner jet diameter D_1, while the relative optimum normalized standoff distance s_N is unaffected. High speed imaging observations show an increase in the average maximum cloud width as a function of D_1.

10. Cavitation intensity and strip curvature increase with outer jet diameter from $D_2 = 21.2$ mm to $D_2 = 24$ mm, but no further increase is observed for $D_2 = 26.8$ mm. This is believed to be due to the development of a condition approaching the fully

submerged jet case for $s_N \leq 45$, where the boundary conditions in the outer flow are no longer affecting the inner jet and where no additional benefits are derived from further increasing the outer flow diameter D_2. High speed imaging observations support the explanation by showing no significant increase in the average maximum cloud width between $D_2 = 24.0$ mm and $D_2 = 26.8$ mm at $s_N = 40 - 45$.

11. Cavitation intensity and strip curvature increase as the nozzle is scaled up while keeping the diameter ratios constant. Nozzle L yields 30% reduction in peening time t_P required to saturate the strip curvature (and therefore residual stress) compared to nozzle M when peening aluminum 7075-T651.

12. Water cavitation peening produces higher compressive residual stresses and less surface roughening of aluminum 7075-T651 than shot peening. While nozzle M produces the highest residual stress (401 MPa), nozzle L produces the deepest compressive residual stress that extends up to 350 µm below the surface.

13. The normalized offset $h=4$ maximizes the cavitation intensity and strip curvature. The optimum normalized standoff distance s_N and the outer flow velocity V_{out} are not affected by the change in nozzle geometry.

14. Frequency analysis of the cavitating flows shows a frequency peak around 2 kHz at standoff distance $s_N = 20$. The peak progressively shifts to lower frequencies as the standoff increases from 20 to 45.

7.1.3 *Pitting Analysis*

The chapter presented a study of the surface pitting generated by WCP. The effect of several flow conditions were investigated and impulsive loads estimated trough stress-strain analysis of individual pits produced by cavitation. A numerical model of the material

behavior while undergoing a single cavitation impact was presented and the results analyzed to obtain the following key findings:

5. Pitting tests confirm the results obtained in previous chapters which indicated higher cavitation loads for the optimum flow conditions of $V_{in} = 150$ m/s, $V_{out} = 11.0$ m/s and $s_N = 45$.

6. The pit stress distribution reported two peaks of different stress intensities. The two peaks can be attributed to different flow-material interaction mechanisms. The large cluster of pit diameters and lower impact loads are attributed to the shock wave mechanism while small, isolated impact diameters and higher impact loads are attributed to the effect of re-entrant jets.

7. The simulations suggest that an increase in the impact load σ_P beyond a critical value can dramatically increase the magnitude of residual stresses, while little influence is observed on the depth at which such peaks occur.

8. The impact diameter d_c has a major effect on the depth of penetration of the residual stress, suggesting that the shock wave-generated large pits determine the residual stress state penetration in the material surface.

170

7.2 Recommendations for Future Work

Related areas for further research include the following:

- Development of a model to predict saturation time in common materials.

- Identification of the cavitation cloud properties responsible for the observed surface modification and correlation of such properties to pit morphology.

- Investigation of nozzle geometry effect on WCP in center regime.

- Evaluation of the micro-structure evolution as a consequence of WCP in common aerospace materials.

- The evaluation of fatigue life improvement as a consequence of the WCP treatment compare do conventional shot peening.

- The WCP can be used to explore alternative processes to peening. Such processes include forming, rust removal, paint stripping and cleaning.

APPENDIX A. SUPPORTING DATA

T-Test on cavitation cloud width as a function of inner jet velocity V_{in} and normalized standoff distance s_N.

s_N	V_{in}	t-test	p-value	V_{in}	t-test	p-value	V_{in}	t-test	p-value	V_{in}
20	90	1	1.16E-11	110	1	3.74E-13	130	1	5.44E-07	150
30	90	1	3.09E-06	110	1	1.30E-14	130	1	1.64E-08	150
40	90	1	9.45E-25	110	1	1.28E-28	130	1	6.65E-11	150
45	90	1	7.80E-20	110	1	1.22E-36	130	1	7.15E-15	150

V_{in}	s_N	t-test	p-value	s_N	t-test	p-value	s_N	t-test	p-value	s_N
90	20	1	5.58E-06	30	1	1.98E-08	40	0	3.19E-01	45
110	20	1	9.00E-03	30	0	8.70E-02	40	0	2.05E-01	45
130	20	1	3.14E-05	30	1	3.29E-07	40	1	5.00E-03	45
150	20	1	3.89E-13	30	1	1.74E-14	40	1	2.44E-05	45

T-Test on cavitation cloud width as a function of outer jet velocity V_{out} and normalized standoff distance s_N.

V_{out}	s_N	t-test	p-value	s_N	t-test	p-value	s_N	t-test	p-value	
6.5	20	1	2.73E-06	30	1	7.14E-04	40	n/a	n/a	45
8.0	20	1	6.63E-08	30	1	0.142	40	0	0.558	45
9.5	20	1	1.13E-11	30	1	0.004	40	0	0.309	45
11.0	20	1	3.89E-13	30	1	1.74E-14	40	1	2.44E-05	45
12.5	20	1	9.95E-07	30	1	5.16E-07	40	1	9.01E-05	45
14.0	20	1	7.37E-06	30	1	3.12E-07	40	0	0.268	45

s_N	V_{out}	t-test	p-value	V_{out}	t-test	p-value	V_{out}	t-test	p-value	V_{out}	t-test	p-value	V_{out}
20	6.5	0	5.42E-01	8.0	1	2.00E-03	9.5	1	3.28E-16	11.0	1	4.10E-09	12.5
30	6.5	0	3.20E-01	8.0	1	2.30E-02	9.5	1	6.89E-15	11.0	1	4.67E-09	12.5
40	6.5	0	6.00E-01	8.0	1	3.44E-02	9.5	1	6.00E-04	11.0	1	5.85E-13	12.5
45	6.5	0	n/a	8.0	0	1.18E-01	9.5	0	1.56E-01	11.0	1	8.18E-13	12.5

REFERENCES

[1] S. Suresh, Fatigue of Materials, Cambridge University Press, 1998.

[2] X. Zhang, D. Liu, Effect of shot peening on fretting fatigue of Ti811 alloy at elevated temperature, International Journal of Fatigue, 31 (2009) 889-893. http://dx.doi.org/10.1016/j.ijfatigue.2008.10.004

[3] C.S. Montross, T. Wei, L. Ye, G. Clark, Y.-W. Mai, Laser shock processing and its effects on microstructure and properties of metal alloys: a review, International Journal of Fatigue, 24 (2002) 1021-1036. http://dx.doi.org/10.1016/S0142-1123(02)00022-1

[4] P. Peyre, C. Carboni, A. Sollier, L. Berthe, C. Richard, E. de Los Rios, R. Fabbro, New trends in laser shock wave physics and applications, International Symposium on High-Power Laser Ablation, International Society for Optics and Photonics, 2002, pp. 654-666.

[5] I. Altenberger, R.K. Nalla, Y. Sano, L. Wagner, R.O. Ritchie, On the effect of deep-rolling and laser-peening on the stress-controlled low- and high-cycle fatigue behavior of Ti–6Al–4V at elevated temperatures up to 550°C, International Journal of Fatigue, 44 (2012) 292-302. http://dx.doi.org/10.1016/j.ijfatigue.2012.03.008

[6] G.H. Majzoobi, K. Azadikhah, J. Nemati, The effects of deep rolling and shot peening on fretting fatigue resistance of Aluminum-7075-T6, Materials Science and Engineering: A, 516 (2009) 235-247. http://dx.doi.org/10.1016/j.msea.2009.03.020

[7] I. Nikitin, I. Altenberger, Comparison of the fatigue behavior and residual stress stability of laser-shock peened and deep rolled austenitic stainless steel AISI 304 in the temperature range 25–600°C, Materials Science and Engineering: A, 465 (2007) 176-182. http://dx.doi.org/10.1016/j.msea.2007.02.004

[8] M. Salahshoor, Y.B. Guo, Surface integrity of biodegradable Magnesium–Calcium orthopedic implant by burnishing, Journal of the Mechanical Behavior of Biomedical Materials, 4 (2011) 1888-1904. http://dx.doi.org/10.1016/j.jmbbm.2011.06.006

[9] H.K. Tönshoff, F. Kroos, C. Marzenell, High-Pressure Water Peening-a New Mechanical Surface-Strengthening Process, CIRP Annals - Manufacturing Technology, 46 (1997) 113-116. http://dx.doi.org/10.1016/S0007-8506(07)60787-2

[10] D. Arola, M.L. McCain, S. Kunaporn, M. Ramulu, Waterjet and abrasive waterjet surface treatment of titanium: a comparison of surface texture and residual stress, Wear, 249 (2001) 943-950. http://dx.doi.org/10.1016/S0043-1648(01)00826-2

[11] A.S. Grinspan, R. Gnanamoorthy, Surface modification by oil jet peening in Al alloys, AA6063-T6 and AA6061-T4: Residual stress and hardness, Applied Surface Science, 253 (2006) 989-996. DOI: 10.1016/j.apsusc.2006.02.060

[12] A.S. Grinspan, R. Gnanamoorthy, Surface modification by oil jet peening in Al alloys, AA6063-T6 and AA6061-T4: Part 2: Surface morphology, erosion, and mass loss, Applied Surface Science, 253 (2006) 997-1005. http://dx.doi.org/10.1016/j.apsusc.2005.12.164

[13] S. Kunaporn, A. Chillman, M. Ramulu, M. Hashish, Effect of waterjet formation on surface preparation and profiling of aluminum alloy, Wear, 265 (2008) 176-185. http://dx.doi.org/10.1016/j.wear.2007.09.008

[14] R. Foschino, C. Picozzi, A. Civardi, M. Bandini, P. Faroldi, Comparison of surface sampling methods and cleanability assessment of stainless steel surfaces subjected or not to shot peening, Journal of Food Engineering, 60 (2003) 375-381. http://dx.doi.org/10.1016/S0260-8774(03)00060-8

[15] H. Soyama, J.D. Park, M. Saka, Use of Cavitating Jet for Introducing Compressive Residual Stress, Journal of Manufacturing Science and Engineering, 122 (2000) 83-89. http://dx.doi.org/10.1115/1.538911

[16] M. Dular, O.C. Delgosha, M. Petkovšek, Observations of cavitation erosion pit formation, Ultrasonics Sonochemistry, 20 (2013) 1113-1120. http://dx.doi.org/10.1016/j.ultsonch.2013.01.011

[17] I. Tzanakis, D.G. Eskin, A. Georgoulas, D.K. Fytanidis, Incubation pit analysis and calculation of the hydrodynamic impact pressure from the implosion of an acoustic cavitation bubble, Ultrasonics Sonochemistry, 21 (2014) 866-878. http://dx.doi.org/10.1016/j.ultsonch.2013.10.003

[18] H. Soyama, Introduction of Compressive Residual Stress Using a Cavitating Jet in Air, Journal of Engineering Materials and Technology, 126 (2004) 123-128. http://dx.doi.org/10.1115/1.1631434

[19] D.O. Macodiyo, H. Soyama, M. Saka, Effect of cavitation number on the improvement of fatigue strength of carburized steel using cavitation shotless peening, Advances in Fracture and Failure Prevention, Pts 1 and 2, 261-263 (2004) 1245-1250.

[20] H. Soyama, F. Takeo, Comparison between cavitation peening and shot peening for extending the fatigue life of a duralumin plate with a hole, Journal of Materials Processing Technology, 227 (2016) 80-87. http://dx.doi.org/10.1016/j.jmatprotec.2015.08.012

[21] ASTM, ASTM G134 - 95(2010)e1 Standard Test Method for Erosion of Solid Materials by a Cavitating Liquid Jet, ASTM International, 2010, pp. 14.

[22] H.S.G. Vijay M.M., Lai M.K.Y., Enhancing the Performance of Cavitating Jets, 7th American Water Jet Conference, Seattle, 1993, pp. 17.

[23] L. Wagner, Mechanical surface treatments on titanium, aluminum and magnesium alloys, Materials Science and Engineering: A, 263 (1999) 210-216. http://dx.doi.org/10.1016/S0921-5093(98)01168-X

174

[24] M. Guagliano, Relating Almen intensity to residual stresses induced by shot peening: a numerical approach, Journal of Materials Processing Technology, 110 (2001) 277-286. http://dx.doi.org/10.1016/S0924-0136(00)00893-1

[25] L. Wagner, M. Mhaede, M. Wollmann, I. Altenberger, Y. Sano, Surface layer properties and fatigue behavior in Al 7075-T73 and Ti-6Al-4V, International Journal of Structural Integrity, 2 (2011) 185-199. doi:10.1108/17579861111135923

[26] V. Schulze, Modern mechanical surface treatment: states, stability, effects, John Wiley & Sons, 2006.

[27] P. Zhang, J. Lindemann, Influence of shot peening on high cycle fatigue properties of the high-strength wrought magnesium alloy AZ80, Scripta Materialia, 52 (2005) 485-490. http://dx.doi.org/10.1016/j.scriptamat.2004.11.003

[28] N. Sidhom, A. Laamouri, R. Fathallah, C. Braham, H.P. Lieurade, Fatigue strength improvement of 5083 H11 Al-alloy T-welded joints by shot peening: experimental characterization and predictive approach, International Journal of Fatigue, 27 (2005) 729-745. http://dx.doi.org/10.1016/j.ijfatigue.2005.02.001

[29] M. Kobayashi, T. Matsui, Y. Murakami, Mechanism of creation of compressive residual stress by shot peening, International Journal of Fatigue, 20 (1998) 351-357. http://dx.doi.org/10.1016/S0142-1123(98)00002-4

[30] M. Frija, T. Hassine, R. Fathallah, C. Bouraoui, A. Dogui, Finite element modelling of shot peening process: Prediction of the compressive residual stresses, the plastic deformations and the surface integrity, Materials Science and Engineering: A, 426 (2006) 173-180. http://dx.doi.org/10.1016/j.msea.2006.03.097

[31] R. Fathallah, A. Laamouri, H. Sidhom, C. Braham, High cycle fatigue behavior prediction of shot-peened parts, International Journal of Fatigue, 26 (2004) 1053-1067. http://dx.doi.org/10.1016/j.ijfatigue.2004.03.007

[32] S.A. Meguid, G. Shagal, J.C. Stranart, J. Daly, Three-dimensional dynamic finite element analysis of shot-peening induced residual stresses, Finite Elements in Analysis and Design, 31 (1999) 179-191. http://dx.doi.org/10.1016/S0168-874X(98)00057-2

[33] M. Benedetti, V. Fontanari, P. Scardi, C.L.A. Ricardo, M. Bandini, Reverse bending fatigue of shot peened 7075-T651 aluminium alloy: The role of residual stress relaxation, International Journal of Fatigue, 31 (2009) 1225-1236. http://dx.doi.org/10.1016/j.ijfatigue.2008.11.017

[34] M.A.S. Torres, H.J.C. Voorwald, An evaluation of shot peening, residual stress and stress relaxation on the fatigue life of AISI 4340 steel, International Journal of Fatigue, 24 (2002) 877-886. http://dx.doi.org/10.1016/S0142-1123(01)00205-5

[35] A. Wick, V. Schulze, O. Vöhringer, Effects of warm peening on fatigue life and relaxation behaviour of residual stresses in AISI 4140 steel, Materials Science and Engineering: A, 293 (2000) 191-197. http://dx.doi.org/10.1016/S0921-5093(00)01035-2

[36] R.W. Landgraf, R. Chernenkoff, Residual stress effects on fatigue of surface processed steels, Analytical and experimental methods for residual stress effects in fatigue, (1988) 1-12.

[37] Y.M. Xing, J. Lu, An experimental study of residual stress induced by ultrasonic shot peening, Journal of Materials Processing Technology, 152 (2004) 56-61. http://dx.doi.org/10.1016/j.jmatprotec.2004.02.057

[38] N.R. Tao, M.L. Sui, J. Lu, K. Lua, Surface nanocrystallization of iron induced by ultrasonic shot peening, Nanostructured Materials, 11 (1999) 433-440. http://dx.doi.org/10.1016/S0965-9773(99)00324-4

[39] V. Schulze, Introduction, Modern Mechanical Surface Treatment, Wiley-VCH Verlag GmbH & Co. KGaA, 2006, pp. 1-7.

[40] R. Fabbro, P. Peyre, L. Berthe, A. Sollier, E. Bartnicki, Physics and applications of laser shock processing of materials, Advanced High-Power Lasers and Applications, (2000) 155-164.

[41] P. Peyre, R. Fabbro, Laser shock processing: a review of the physics and applications, Optical and Quantum Electronics, 27 (1995) 1213-1229. 10.1007/bf00326477

[42] E. Maawad, Y. Sano, L. Wagner, H.G. Brokmeier, C. Genzel, Investigation of laser shock peening effects on residual stress state and fatigue performance of titanium alloys, Materials Science and Engineering: A, 536 (2012) 82-91. http://dx.doi.org/10.1016/j.msea.2011.12.072

[43] E. Maawad, H.G. Brokmeier, L. Wagner, Y. Sano, C. Genzel, Investigation on the surface and near-surface characteristics of Ti–2.5Cu after various mechanical surface treatments, Surface and Coatings Technology, 205 (2011) 3644-3650. 10.1016/j.surfcoat.2011.01.001

[44] H. Luong, M.R. Hill, The effects of laser peening on high-cycle fatigue in 7085-T7651 aluminum alloy, Materials Science and Engineering: A, 477 (2008) 208-216. http://dx.doi.org/10.1016/j.msea.2007.05.024

[45] R. Fabbro, J. Fournier, P. Ballard, D. Devaux, J. Virmont, Physical study of laser-produced plasma in confined geometry, Journal of Applied Physics, 68 (1990) 775-784. doi:http://dx.doi.org/10.1063/1.346783

[46] A. Sollier, L. Berthe, P. Peyre, E. Bartnicki, R. Fabbro, Laser-matter interaction in laser shock processing, 2003, pp. 463-467.

[47] P. Ballard, Contraintes résiduelles induites par impact rapide. Application au choc-laser., Ecole Polytechnique, 1991.

[48] C. Yang, P.D. Hodgson, Q. Liu, L. Ye, Geometrical effects on residual stresses in 7050-T7451 aluminum alloy rods subject to laser shock peening, Journal of Materials Processing Technology, 201 (2008) 303-309. http://dx.doi.org/10.1016/j.jmatprotec.2007.11.147

[49] A.W. Warren, Y.B. Guo, S.C. Chen, Massive parallel laser shock peening: Simulation, analysis, and validation, International Journal of Fatigue, 30 (2008) 188-197. http://dx.doi.org/10.1016/j.ijfatigue.2007.01.033

[50] K. Ding, L. Ye, Simulation of multiple laser shock peening of a 35CD4 steel alloy, Journal of Materials Processing Technology, 178 (2006) 162-169. http://dx.doi.org/10.1016/j.jmatprotec.2006.03.170

[51] W. Braisted, R. Brockman, Finite element simulation of laser shock peening, International Journal of Fatigue, 21 (1999) 719-724. http://dx.doi.org/10.1016/S0142-1123(99)00035-3

[52] W. Zhang, Y.L. Yao, I. Noyan, Microscale laser shock peening of thin films, part 1: experiment, modeling and simulation, Journal of Manufacturing Science and Engineering, 126 (2004) 10-17.

[53] W. Zhang, Y.L. Yao, I. Noyan, Microscale laser shock peening of thin films, part 2: high spatial resolution material characterization, Journal of Manufacturing Science and Engineering, 126 (2004) 18-24.

[54] H. Chen, J.W. Kysar, Y.L. Yao, Characterization of plastic deformation induced by microscale laser shock peening, Journal of applied mechanics, 71 (2004) 713-723.

[55] Y. Fan, Y. Wang, S. Vukelic, Y.L. Yao, Wave-solid interactions in laser-shock-induced deformation processes, Journal of Applied Physics, 98 (2005) 104904.

[56] M. Ramulu, S. Kunaporn, D. Arola, M. Hashish, J. Hopkins, Waterjet Machining and Peening of Metals, Journal of Pressure Vessel Technology, 122 (1999) 90-95. 10.1115/1.556155

[57] M. Ramulu, S. Kunaporn, M. Jenkins, M. Hashish, J. Hopkins, Fatigue Performance of High-Pressure Waterjet-Peened Aluminum Alloy, Journal of Pressure Vessel Technology, 124 (2001) 118-123. 10.1115/1.1398553

[58] S. Kunaporn, An Experimental and Numerical Analysis of Waterjet Peening of 7075-T6 Aluminum Alloy. , University of Washington, 2002.

[59] S. Kunaporn, M. Ramulu, M. Hashish, Mathematical Modeling of Ultra-High-Pressure Waterjet Peening, Journal of Engineering Materials and Technology, 127 (2005) 186-191. 10.1115/1.1857934

[60] N. Rajesh, S. Veeraraghavan, N. Ramesh Babu, A novel approach for modelling of water jet peening, International Journal of Machine Tools and Manufacture, 44 (2004) 855-863. http://dx.doi.org/10.1016/j.ijmachtools.2004.01.010

[61] N. Rajesh, N. Ramesh Babu, Multidroplet Impact Model for Prediction of Residual Stresses in Water Jet Peening of Materials, Materials and Manufacturing Processes, 21 (2006) 399-409. 10.1080/10426910500411736

[62] S.R. Daniewicz, S.D. Cummings, Characterization of a Water Peening Process, Journal of Engineering Materials and Technology, 121 (1999) 336-340. 10.1115/1.2812383

[63] L. Huang, J. Folkes, P. Kinnell, P.H. Shipway, Mechanisms of damage initiation in a titanium alloy subjected to water droplet impact during ultra-high pressure plain waterjet erosion, Journal of Materials Processing Technology, 212 (2012) 1906-1915. 10.1016/j.jmatprotec.2012.04.013

[64] A.S. Grinspan, R. Gnanamoorthy, Effect of oil jet peening duration on surface modification and fatigue behavior of medium carbon steel, AISI 1040, Materials Science and Engineering: A, 456 (2007) 210-217. DOI: 10.1016/j.msea.2006.11.107

[65] A.S. Grinspan, R. Gnanamoorthy, A novel surface modification technique for the introduction of compressive residual stress and preliminary studies on Al alloy AA6063, Surface and Coatings Technology, 201 (2006) 1768-1775. DOI: 10.1016/j.surfcoat.2006.03.002

[66] M. Talks, G. Moreton, Cavitation Erosion of Fire-Resistant Hydraulic Fluids, Cavitation Erosion in Fluid Systems[Proc. Conf.], Boulder, Colo., U. S. A., June 1981, 1981, pp. 139-152.

[67] I. Altenberger, Deep rolling–the past, the present and the future, Proceedings of 9th International Conference on Shot Peening, Sept, 2005, pp. 6-9.

[68] P.S. Prevey, N. Jayaraman, R.A. Ravindranath, M. Shepard, Mitigation of fretting fatigue damage in blade and disk pressure faces with low plasticity burnishing, Journal of Engineering for Gas Turbines and Power, 132 (2010). 10.1115/1.2943154

[69] P.S. Prevey, N. Jayaraman, R. Ravindranath, Fatigue life extension of steam turbine alloys using Low Plasticity Burnishing (LPB), ASME Turbo Expo 2010: Power for Land, Sea, and Air, GT 2010, June 14, 2010 - June 18, 2010, American Society of Mechanical Engineers, Glasgow, United kingdom, 2010, pp. 2277-2287.

[70] P.S. Prevéy, J.T. Cammett, The influence of surface enhancement by low plasticity burnishing on the corrosion fatigue performance of AA7075-T6, International Journal of Fatigue, 26 (2004) 975-982. http://dx.doi.org/10.1016/j.ijfatigue.2004.01.010

[71] U. Jung, B. Kaiser, K.H. Kloos, C. Berger, Festwalz-Eigenspannungen per computer-Simulation bestimmen, Materialwissenschaft und Werkstofftechnik, 27 (1996) 159-164. 10.1002/mawe.19960270408

[72] M. Sayahi, S. Sghaier, H. Belhadjsalah, Finite element analysis of ball burnishing process: comparisons between numerical results and experiments, The International Journal of Advanced Manufacturing Technology, 67 (2013) 1665-1673. 10.1007/s00170-012-4599-9

[73] W. Bouzid Saï, K. Saï, Finite element modeling of burnishing of AISI 1042 steel, The International Journal of Advanced Manufacturing Technology, 25 (2005) 460-465. 10.1007/s00170-003-1993-3

[74] P. Sartkulvanich, T. Altan, F. Jasso, C. Rodriguez, Finite Element Modeling of Hard Roller Burnishing: An Analysis on the Effects of Process Parameters Upon Surface Finish and Residual Stresses, Journal of Manufacturing Science and Engineering, 129 (2007) 705-716. 10.1115/1.2738121

[75] R.K. Nalla, I. Altenberger, U. Noster, G.Y. Liu, B. Scholtes, R.O. Ritchie, On the influence of mechanical surface treatments—deep rolling and laser shock peening—on the fatigue behavior of Ti–6Al–4V at ambient and elevated temperatures, Materials Science and Engineering: A, 355 (2003) 216-230. http://dx.doi.org/10.1016/S0921-5093(03)00069-8

[76] C.A. Rodopoulos, A.T. Kermanidis, E. Statnikov, V. Vityazev, O. Korolkov, The Effect of Surface Engineering Treatments on the Fatigue Behavior of 2024-T351 Aluminum Alloy, Journal of Materials Engineering and Performance, 16 (2007) 30-34. 10.1007/s11665-006-9004-0

[77] H. Luong, M.R. Hill, The effects of laser peening and shot peening on high cycle fatigue in 7050-T7451 aluminum alloy, Materials Science and Engineering: A, 527 (2010) 699-707. http://dx.doi.org/10.1016/j.msea.2009.08.045

[78] H. Blickwedel, H. Haferkamp, H. Louis, P. Tai, Modification of material structure by cavitation and liquid impact and their influence on mechanical properties, Erosion by Liquid and Solid Impact, Seventh International Conference, 1987, pp. 31.

[79] D. Odhiambo, H. Soyama, Cavitation shotless peening for improvement of fatigue strength of carbonized steel, International Journal of Fatigue, 25 (2003) 1217-1222. Doi 10.1016/S0142-1123(03)00121-X

[80] H. Soyama, K. Saito, M. Saka, Improvement of fatigue strength of aluminum alloy by cavitation shotless peening, Journal of Engineering Materials and Technology-Transactions of the Asme, 124 (2002) 135-139. Doi 10.1115/1.1447926

[81] H. Soyama, K. Sasaki, D. Odhiambo, M. Saka, Cavitation shotless peening for surface modification of alloy tool steel, Jsme International Journal Series a-Solid Mechanics and Material Engineering, 46 (2003) 398-402.

179

[82] B. Han, H. Zhang, D.Y. Ju, Investigation of Water Cavitation Peening-Induced Microstructures and Residual Stress in the Near-Surface Spring Steel SAE 1070, Advanced Materials Research, 299 (2011) 1036-1039.

[83] H. Soyama, D. Macodiyo, S. Mall, Compressive Residual Stress into Titanium Alloy Using Cavitation Shotless Peening Method, Tribology Letters, 17 (2004) 501-504. http://dx.doi.org/10.1023/B:TRIL.0000044497.45014.f2

[84] D.Y. Ju, B. Han, Investigation of water cavitation peening-induced microstructures in the near-surface layer of pure titanium, Journal of Materials Processing Technology, 209 (2009) 4789-4794. DOI: 10.1016/j.jmatprotec.2008.12.006

[85] H. Soyama, Effect of nozzle geometry on a standard cavitation erosion test using a cavitating jet, Wear, 297 (2013) 895-902. http://dx.doi.org/10.1016/j.wear.2012.11.008

[86] H. Soyama, Enhancing the Aggressive Intensity of a Cavitating Jet by Means of the Nozzle Outlet Geometry, Journal of Fluids Engineering, 133 (2011) 101301-101311. http://dx.doi.org/10.1115/1.4004905

[87] M. Qin, D.Y. Ju, R. Oba, Improvement on the process capability of water cavitation peening by aeration, Surface and Coatings Technology, 200 (2006) 5364-5369. DOI: 10.1016/j.surfcoat.2005.06.024

[88] B. Han, D.Y. Ju, W.P. Jia, Influence of water cavitation peening with aeration on fatigue behaviour of SAE1045 steel, Applied Surface Science, 253 (2007) 9342-9346. DOI: 10.1016/j.apsusc.2007.05.076

[89] A.S. Grinspan, R. Gnanamoorthy, Development of a Novel Oil Cavitation Jet Peening System and Cavitation Jet Erosion in Aluminum Alloy, AA 6063-T6, Journal of Fluids Engineering, 131 (2009) 061301-061308. 10.1115/1.3129134

[90] A.S. Grinspan, R. Gnanamoorthy, Effect of Nozzle-Traveling Velocity on Oil Cavitation Jet Peening of Aluminum Alloy, AA 6063-T6, Journal of Engineering Materials and Technology, 129 (2007) 609-613. 10.1115/1.2772339

[91] D.O. Macodiyo, H. Soyama, Optimization of cavitation peening parameters for fatigue performance of carburized steel using Taguchi methods, Journal of Materials Processing Technology, 178 (2006) 234-240. 10.1016/j.jmatprotec.2006.03.172

[92] M. Qin, D.Y. Ju, R. Oba, Investigation of the influence of incidence angle on the process capability of water cavitation peening, Surface and Coatings Technology, 201 (2006) 1409-1413. DOI: 10.1016/j.surfcoat.2006.02.006

[93] B. Han, D.Y. Ju, X.G. Yu, Combined finite element method and dislocation density method solution to residual stress induced by water cavitation peening, Materials & Design, 31 (2010) 3317-3323. DOI: 10.1016/j.matdes.2010.02.004

[94] B. Han, D.Y. Ju, Compressive residual stress induced by water cavitation peening: A finite element analysis, Materials & Design, 30 (2009) 3325-3332. DOI: 10.1016/j.matdes.2008.11.029

[95] O. Takakuwa, M. Nishikawa, H. Soyama, Estimation of the depth of surface modification layer induced by cavitation peening, Journal of Materials Processing Technology, 212 (2012) 1716-1722. http://dx.doi.org/10.1016/j.jmatprotec.2012.03.010

[96] V.M.M. Lai M.K.Y, Zou C., Computational fluid dynamic analysis of submerged cavitating water jets 6th American Water Jet Conference, Houston, TX, 1991.

[97] H. Soyama, T. Kikuchi, M. Nishikawa, O. Takakuwa, Introduction of compressive residual stress into stainless steel by employing a cavitating jet in air, Surface and Coatings Technology, 205 (2011) 3167-3174. http://dx.doi.org/10.1016/j.surfcoat.2010.11.031

[98] H. Soyama, Improvement of fatigue strength by using cavitating jets in air and water, Journal of Materials Science, 42 (2007) 6638-6641. http://dx.doi.org/10.1007/s10853-007-1535-8

[99] R. Marsh, Experimental analysis of oil based cavitation peening in air, Georgia Institute of Technology, 2011, pp. 131.

[100] O. Takakuwa, H. Soyama, The effect of scanning pitch of nozzle for a cavitating jet during overlapping peening treatment, Surface and Coatings Technology, (2012). http://dx.doi.org/10.1016/j.surfcoat.2012.03.034

[101] H. Soyama, High-Speed Observation of a Cavitating Jet in Air, Journal of Fluids Engineering, 127 (2005) 1095-1101. http://dx.doi.org/10.1115/1.2060737

[102] S. Young, J. Johnston, Effect of temperature and pressure on cavitation damage in sodium, Characterization and Determination of Erosion Resistance, ASTM International, 1970.

[103] S. Hattori, F. Inoue, K. Watashi, T. Hashimoto, Effect of liquid properties on cavitation erosion in liquid metals, Wear, 265 (2008) 1649-1654. http://dx.doi.org/10.1016/j.wear.2008.04.007

[104] R. Garcia, F.G. Hammitt, Cavitation Damage and Correlations With Material and Fluid Properties, Journal of Basic Engineering, 89 (1967) 753-763. http://dx.doi.org/10.1115/1.3609699

[105] S. Hattori, Y. Goto, T. Fukuyama, Influence of temperature on erosion by a cavitating liquid jet, Wear, 260 (2006) 1217-1223. http://dx.doi.org/10.1016/j.wear.2005.08.001

[106] M.S. Plesset, Temperature Effects in Cavitation Damage, Journal of Basic Engineering, 94 (1972) 559-563. http://dx.doi.org/10.1115/1.3425484

181

[107] J.V.E. Johnson, G.L. Chahine, W.T. Lindenmuth, A.F. Conn, G.S. Frederick, J.G.J. Giacchino, Cavitating and Structured Jets for Mechanical Bits to Increase Drilling Rate—Part I: Theory and Concepts, Journal of Energy Resources Technology, 106 (1984) 282-288. http://dx.doi.org/10.1115/1.3231053

[108] J.V.E. Johnson, G.L. Chahine, W.T. Lindenmuth, A.F. Conn, G.S. Frederick, J.G.J. Giacchino, Cavitating and Structured Jets for Mechanical Bits to Increase Drilling Rate—Part II: Experimental Results, Journal of Energy Resources Technology, 106 (1984) 289-294. http://dx.doi.org/10.1115/1.3231054

[109] G.L. Chahine, A.F. Conn, V.E. Johnson Jr, Cleaning and cutting with self-resonating pulsed water jets, 2nd US Water Jet Conference, Citeseer, 1983.

[110] Z.C. Vijay M.M., Tavoularis S., A Study of the Characteristics of Cavitating Waterjets by Photography and Erosion, in: E.S.P. Ltd (Ed.) Jet Cutting Technology, Amsterdam, 1991.

[111] Y. Yamauchi, H. Soyama, Y. Adachi, K. Sato, T. Shindo, R. Oba, R. Oshima, M. Yamabe, Suitable Region of High-Speed Submerged Water Jets for Cutting and Peening, JSME International Journal Series B, 38 (1995) 31-38. http://dx.doi.org/10.1299/jsmeb.38.31

[112] H. Soyama, Enhancing the aggressive intensity of a cavitating jet by introducing a cavitator and a guide pipe, Journal of Fluid Science and Technology, 9 (2014) JFST0001-JFST0001. http://doi.org/10.1299/jfst.2014jfst0001

[113] D. Li, Y. Kang, X. Wang, X. Ding, Z. Fang, Effects of nozzle inner surface roughness on the cavitation erosion characteristics of high speed submerged jets, Experimental Thermal and Fluid Science, 74 (2016) 444-452. http://dx.doi.org/10.1016/j.expthermflusci.2016.01.009

[114] A. Marcon, S.N. Melkote, J. Castle, D.G. Sanders, M. Yoda, Effect of jet velocity in co-flow water cavitation jet peening, Wear, 360–361 (2016) 38-50. http://dx.doi.org/10.1016/j.wear.2016.03.027

[115] E.A. Hutli, M.S. Nedeljkovic, I. Vojislav, An Experimental Investigation of Cavitating Jet Dynamic Power and Cavitation Intensity, ASME 2010 International Mechanical Engineering Congress and Exposition, American Society of Mechanical Engineers, 2010, pp. 343-351.

[116] J.-K. Choi, A. Jayaprakash, G.L. Chahine, Scaling of cavitation erosion progression with cavitation intensity and cavitation source, Wear, 278–279 (2012) 53-61. http://dx.doi.org/10.1016/j.wear.2012.01.008

[117] H. Rouse, Cavitation in the mixing zone of a submerged jet, La Houille Blanche, (1953) 9-19.

[118] K.K. Ooi, Scale effects on cavitation inception in submerged water jets: a new look, Journal of Fluid Mechanics, 151 (1985) 367-390. doi:10.1017/S0022112085001008

[119] W.A. Straka, R.S. Meyer, A.A. Fontaine, J.P. Welz, Cavitation inception in quiescent and co-flow nozzle jets, Journal of Hydrodynamics, Ser. B, 22 (2010) 813-819. Doi: 10.1016/s1001-6058(10)60035-2

[120] H. Soyama, Y. Yanauchi, K. Sato, T. Ikohagi, R. Oba, R. Oshima, High-speed observation of ultrahigh-speed submerged water jets, Experimental Thermal and Fluid Science, 12 (1996) 411-416. http://dx.doi.org/10.1016/0894-1777(95)00124-7

[121] H. Soyama, Y. Yamauchi, Y. Adachi, K. Sato, T. Shindo, R. Oba, High-Speed Observations of the Cavitation Cloud around a High-Speed Submerged Water-Jet, Jsme International Journal Series B-Fluids and Thermal Engineering, 38 (1995) 245-251. http://doi.org/10.1299/jsmeb.38.245

[122] S. Hattori, M. Takinami, Comparison of cavitation erosion rate with liquid impingement erosion rate, Wear, 269 (2010) 310-316. http://dx.doi.org/10.1016/j.wear.2010.04.020

[123] M.S. Plesset, R.B. Chapman, Collapse of an initially spherical vapour cavity in the neighbourhood of a solid boundary, Journal of Fluid Mechanics, 47 (1971) 283-290.

[124] Y. Tomita, A. Shima, Mechanisms of impulsive pressure generation and damage pit formation by bubble collapse, Journal of Fluid Mechanics, 169 (1986) 535-564.

[125] B. Ward, D. Emmony, Direct observation of the pressure developed in a liquid during cavitation-bubble collapse, Applied physics letters, 59 (1991) 2228-2230.

[126] C. Haosheng, L. Shihan, Inelastic damages by stress wave on steel surface at the incubation stage of vibration cavitation erosion, Wear, 266 (2009) 69-75. 10.1016/j.wear.2008.05.011

[127] J.-K. Choi, A. Jayaprakash, A. Kapahi, C.-T. Hsiao, G. Chahine, Relationship between space and time characteristics of cavitation impact pressures and resulting pits in materials, Journal of Materials Science, 49 (2014) 3034-3051. http://dx.doi.org/10.1007/s10853-013-8002-5

[128] A. Jayaprakash, J.-K. Choi, G.L. Chahine, F. Martin, M. Donnelly, J.-P. Franc, A. Karimi, Scaling study of cavitation pitting from cavitating jets and ultrasonic horns, Wear, 296 (2012) 619-629. http://dx.doi.org/10.1016/j.wear.2012.07.025

[129] J.-P. Franc, M. Riondet, A. Karimi, G.L. Chahine, Material and velocity effects on cavitation erosion pitting, Wear, 274–275 (2012) 248-259. http://dx.doi.org/10.1016/j.wear.2011.09.006

[130] J.-P. Franc, Incubation Time and Cavitation Erosion Rate of Work-Hardening Materials, Journal of Fluids Engineering, 131 (2009) 021303-021314.

183

[131] C.G.L. Kim K-H, Franc J-P, Karimi A., Advanced Experimental and Numerical Techniques for Cavitation Erosion Prediction, Springer, 2014.

[132] S. Hattori, T. Hirose, K. Sugiyama, Prediction method for cavitation erosion based on measurement of bubble collapse impact loads, Wear, 269 (2010) 507-514. http://dx.doi.org/10.1016/j.wear.2010.05.015

[133] H. Soyama, A. Lichtarowicz, T. Momma, E.J. Williams, A new calibration method for dynamically loaded transducers and its application to cavitation impact measurement, Journal of Fluids Engineering-Transactions of the Asme, 120 (1998) 712-718.

[134] H. Soyama, Y. Sekine, K. Saito, Evaluation of the enhanced cavitation impact energy using a PVDF transducer with an acrylic resin backing, Measurement, 44 (2011) 1279-1283. http://dx.doi.org/10.1016/j.measurement.2011.03.027

[135] Y.-C. Wang, Y.-W. Chen, Application of piezoelectric PVDF film to the measurement of impulsive forces generated by cavitation bubble collapse near a solid boundary, Experimental Thermal and Fluid Science, 32 (2007) 403-414. DOI: 10.1016/j.expthermflusci.2007.05.003

[136] T. Momma, A. Lichtarowicz, A study of pressures and erosion produced by collapsing cavitation, Wear, 186–187, Part 2 (1995) 425-436. 10.1016/0043-1648(95)07144-x

[137] J.-P. Franc, M. Riondet, A. Karimi, G.L. Chahine, Impact Load Measurements in an Erosive Cavitating Flow, Journal of Fluids Engineering, 133 (2011) 121301-121308.

[138] R.T. Knapp, J.W. Daily, F.G. Hammitt, Cavitation, (1979).

[139] D. Carnelli, A. Karimi, J.-P. Franc, Evaluation of the hydrodynamic pressure of cavitation impacts from stress–strain analysis and geometry of individual pits, Wear, 289 (2012) 104-111. http://dx.doi.org/10.1016/j.wear.2012.04.009

[140] D. Carnelli, A. Karimi, J.-P. Franc, Application of spherical nanoindentation to determine the pressure of cavitation impacts from pitting tests, Journal of Materials Research, 27 (2012) 91-99. doi:10.1557/jmr.2011.259

[141] H. Soyama, Surface mechanics design by cavitation peening, The Journal of Engineering, Institution of Engineering and Technology, 2015.

[142] D.A. Summers, Waterjetting Technology, E & FN SPON, 1995.

[143] J.P. Franc, J.M. Michel, Fundamentals of Cavitation, Kluwer Academic Publishers, 2004.

[144] H. Soyama, A. Lichtarowicz, T. Maomma, Vortex cavitation in a submerged jet, ASME-PUBLICATIONS-FED, 236 (1996) 415-422.

[145] U. Zupanc, J. Grum, Effect of pitting corrosion on fatigue performance of shot-peened aluminium alloy 7075-T651, Journal of Materials Processing Technology, 210 (2010) 1197-1202. http://dx.doi.org/10.1016/j.jmatprotec.2010.03.004

[146] P. Withers, Residual stress and its role in failure, Reports on progress in physics, 70 (2007) 2211.

[147] S. Liang, J.-C. Su, Residual stress modeling in orthogonal machining, CIRP Annals-Manufacturing Technology, 56 (2007) 65-68.

[148] K. Jacobus, R. DeVor, S. Kapoor, Machining-induced residual stress: experimentation and modeling, Journal of Manufacturing Science and Engineering, 122 (2000) 20-31.

[149] M. Sutton, A. Reynolds, D.-Q. Wang, C. Hubbard, A study of residual stresses and microstructure in 2024-T3 aluminum friction stir butt welds, Journal of Engineering Materials and Technology, 124 (2002) 215-221.

[150] J. Romero, M. Attallah, M. Preuss, M. Karadge, S. Bray, Effect of the forging pressure on the microstructure and residual stress development in Ti–6Al–4V linear friction welds, Acta Materialia, 57 (2009) 5582-5592.

[151] I.C. Noyan, J.B. Cohen, Residual Stresses, Measurement by Diffraction and Interpretation, 1 ed., Springer-Verlag New York, 1987.

[152] C.E. Brennen, Cavitation and bubble dynamics, Cambridge University Press, 2013.

[153] C.-T. Hsiao, A. Jayaprakash, A. Kapahi, J.-K. Choi, G.L. Chahine, Modelling of material pitting from cavitation bubble collapse, Journal of Fluid Mechanics, 755 (2014) 142-175. http://dx.doi.org/10.1017/jfm.2014.394

[154] A. Jayaprakash, C.-T. Hsiao, G. Chahine, Numerical and experimental study of the interaction of a spark-generated bubble and a vertical wall, Journal of Fluids Engineering, 134 (2012) 031301.

[155] J.-K. Choi, G.L. Chahine, Relationship between material pitting and cavitation field impulsive pressures, Wear, 352–353 (2016) 42-53. http://dx.doi.org/10.1016/j.wear.2016.01.019

[156] G.L. Chahine, C.-T. Hsiao, Modelling cavitation erosion using fluid–material interaction simulations, Interface Focus, 5 (2015). http://dx.doi.org/10.1098/rsfs.2015.0016

[157] D. Tabor, The hardness of metals, Oxford university press, 2000.

[158] H. Francis, Phenomenological analysis of plastic spherical indentation, Journal of Engineering Materials and technology, 98 (1976) 272-281.

[159] S.C. Roy, J.-P. Franc, N. Ranc, M. Fivel, Determination of cavitation load spectra—Part 2: Dynamic finite element approach, Wear, 344–345 (2015) 120-129. http://dx.doi.org/10.1016/j.wear.2015.09.005

[160] G.R. Johnson, W.H. Cook, A constitutive model and data for metals subjected to large strains, high strain rates and high temperatures, Proceedings of the 7th International Symposium on Ballistics, The Netherlands, 1983, pp. 541-547.

[161] N.S. Brar, V.S. Joshi, B.W. Harris, CONSTITUTIVE MODEL CONSTANTS FOR Al7075-T651 and Al7075-T6, AIP Conference Proceedings, 1195 (2009) 945-948. 10.1063/1.3295300